MAYNOOTH UNIVERSITY

MASTERS THESIS

Quasi-optical and Electromagnetic Modelling at Gigahertz and Terahertz Frequencies

---

Author:	*Supervisor:*
Jack GRAHAM	Dr Créidhe O'SULLIVAN

A thesis submitted in fulfillment of the requirements
for the degree of Master of Science

in the

Terahertz Space Optics Group
Department of Experimental Physics

August 15, 2022

Declaration of Authorship

I, Jack GRAHAM, declare that this thesis titled, “ Quasi-optical and Electromagnetic Modelling at Gigahertz and Terahertz Frequencies” and the work presented in it are my own. I confirm that:

- This work was done wholly or mainly while in candidature for a research degree at this University.
- Where any part of this thesis has previously been submitted for a degree or any other qualification at this University or any other institution, this has been clearly stated.
- Where I have consulted the published work of others, this is always clearly attributed.
- Where I have quoted from the work of others, the source is always given. With the exception of such quotations, this thesis is entirely my own work.
- I have acknowledged all main sources of help.
- Where the thesis is based on work done by myself jointly with others, I have made clear exactly what was done by others and what I have contributed myself.

Signed:

Date:

"We are all in the gutter, but some of us are looking at the stars."

Oscar Wilde

MAYNOOTH UNIVERSITY

Abstract

Faculty of Science and Engineering
Department of Experimental Physics

Master of Science

Quasi-optical and Electromagnetic Modelling at Gigahertz and Terahertz Frequencies

by Jack GRAHAM

This thesis describes electromagnetic and optical modelling for three telescopes operating at GHz and THz frequencies: the Pickmere telescope, QUBIC and ALMA. Optical modelling was carried out using TICRA's GRASP physical optics software and also using a Gaussian beam mode model developed in Python. The electromagnetic modelling of corrugated horn antennas was carried out using Maynooth University's existing mode-matching software 'PyScatter' and new code developed for this thesis called 'NumCross'.

The Pickmere radio telescope was simulated using Gaussian beam modes and also using GRASP physical optics. The two methods agreed to a high level of accuracy. This verified the accuracy of Gaussian beam mode analysis as a rapid, simplistic model of sequential mirrors in telescopes.

A series of horns were developed for a potential ALMA combined band 4 and 5, and in particular the effects of different manufacturing constraints on horn performance were shown. A comparison was made between the inhouse PyScatter routine and the industry standard HFSS software used by collaborators in Manchester University. The programs largely agreed, with one difference caused by differing sensitivity to back-propagation of radiation.

The QUBIC telescope makes use of an array of corrugated horn antennas manufactured using a platelet technique. The plates can incur lateral offsets due to alignment tolerances during manufacturing. These offsets cannot be modelled in PyScatter as it assumes cylindrical symmetry at platelet junctions. The NumCross routine was created, building on PyScatter, to allow the modelling of corrugated horns with laterally offset corrugations. The QUBIC horns were modelled as an example.

Acknowledgements

I would like to thank my supervisor Créidhe, and co-supervisor Anthony, for their many hours dedicated to guiding and correcting my work. Throughout this difficult time for teaching you have both gone above and beyond to ensure that I could continue my research unimpeded, whether in person or remotely.

A word also to Ian, Frank, Peter and the student demonstrators, for making my teaching role here at the University a rewarding and enjoyable experience. Indeed, the department as a whole has fostered a great atmosphere of camaraderie and cooperation during my almost seven years of study here, something I am immensely lucky to have experienced.

I acknowledge funding from the UK's STFC seedcorn budget as part of the Manchester-Maynooth project "Development of millimetre optics components for ALMA", under PI Prof. Keith Grainge of Manchester University. I would like to thank members of Manchester's Advanced Instrumentation Group for their guidance at our fortnightly telecons, in particular Dr Mark McCulloch with whom I worked closely on horn designs, Prof. Keith Grainge (PI), Prof. Gary Fuller (Co-I), Prof. Danielle George (Co-I), Prof Brian Ellison (RAL), Prof Claudio Jarufe, Will McGenn, Amy Suddards and Long Jiang.

Finally, I wish to thank my mother Janet and brother Adam, for their unending support, financial, practical and emotional, which allowed me to complete my studies despite the adversity of the last couple of years.

Contents

List of Figures

List of Tables

List of Abbreviations

AIG	**A**dvanced **I**nstrumentation **G**roup
ADS	**A**ctive **D**efense **S**ystem
ALMA	**A**tacama **L**arge **M**illimeter **A**rray
CMB	**C**osmic **M**icrowave **B**ackground
DEW	**D**irected **E**nergy **W**eapon
EMR	**E**lectro**M**agnetic **R**adiation
ESO	**E**uropean **S**outhern **O**bservatory
EHT	**E**vent **H**orizon **T**elescope
HFSS	**H**igh **F**requency **S**tructure **S**imulator
HWP	**H**alf **W**ave **P**late
LLAMA	**L**arge **L**atin **A**merican **M**illimetre **A**rray
LNA	**L**ow **N**oise **A**mplifier
MERLIN	**M**ulti **E**lement **R**adio **L**inked **IN**terferometer
OMT	**O**rtho **M**ode **T**ransducer
PAF	**P**hased **A**rray **F**eed
PO	**P**hysical **O**ptics
POLARBEAR	**POLAR**isation of the **B**ackground **R**adiation
QUBIC	**Q** (and) **U** **B**olometer **I**nterferometer (for) **C**osmology
SQUID	**S**uperconducting **Q**uantum **I**nterference **D**evice
SSB	**S**ingle **S**ide **B**and
SVD	**S**ingular **V**alue **D**ecomposition
TES	**T**ransition **E**dge **S**ensor
2SB	**D**ual **S**ide **B**and

Physical Constants

Astronomical Unit	$\mathrm{AU} = 1.495\,978\,70 \times 10^{8}\,\mathrm{m}$
Hubble Parameter	$H_0 = 2.1(8) \times 10^{-18}\,\mathrm{s}$
Impedance of free space	$Z_0 = 3.767\,303\,14 \times 10^{2}\,\Omega$
Parsec	$\mathrm{pc} = 3.085\,677\,58 \times 10^{16}\,\mathrm{m}$
Plank Constant	$h = 6.626\,070\,15 \times 10^{-34}\,\mathrm{J\,s}$
Speed of Light	$c_0 = 2.997\,924\,58 \times 10^{-8}\,\mathrm{m\,s^{-1}}$
Vacuum Permeability	$\mu_0 = 1.256\,637\,06 \times 10^{-6}\,\mathrm{H\,m^{-1}}$
Vacuum Permittivity	$\epsilon_0 = 8.854\,187\,81 \times 10^{-12}\,\mathrm{F\,m^{-1}}$
Wiens Displacement Constant	$b = 2.897\,771\,95 \times 10^{-3}\,\mathrm{m\,K}$

To my mother, without whom I would never have reached this milestone…

Chapter 1

Introduction

1.1 Introduction to the GHz/THz spectrum

The domain of GHz and THz radiation covers a vast swathe of the electromagnetic spectrum, from UHF radio with a frequency on the order of 1 GHz, to visible light with a frequency on the order of hundreds of THz. These six decades of frequency support the vast majority of human communications, from optical fiber pulses, to computer clock frequencies, to high frequency radio transmission.

The work presented herein pertains both to the THz region and occasionally to lower GHz frequencies, especially with GRASP software modelling, as described in Chapter 2. By convention, the THz region is considered to be between 100 GHz and 10 THz (Gallerano 2004). This band of electromagnetic radiation (EMR) has traditionally been neglected by scientific inquiry, despite its ubiquity on Earth; we are constantly swathed in THz radiation, as the peak frequency of thermal emission from most terrestrial sources, as described by Wiens Law, ($\lambda_{max} = \frac{b}{T}$, where b is Wiens constant, and T is temperature) falls in the upper range of this band. Correspondingly, peak thermal emission from a body at 0°C lies at 16 THz. This lack of research is primarily due to the difficulty in creating suitable sources and detectors to function at these frequencies (Wilmink and Grundt 2011). In recent years, with the advent of better sources and feeds, much research has been undertaken at these frequencies, across multiple fields of science. Some of the fields and applications are explained below.

1.2 THz medical applications

THz radiation holds great promise in the field of noninvasive diagnostic medicine, due to its innate properties of non-ionising interaction, preferential interaction with water over other compounds, and ample penetration of clothing, medical dressings and skin. Several specific fields where such imaging may be used are discussed below.

1.2.1 Oncological uses

Beams in the THz region may be used, either pulsed or continuous wave, to detect subtle changes in the water content of cells in a refined target region. This registers as a change in the absorptive character of the tissue, and thus the intensity of radiation received at the detector after exposure. These cellular changes may be indicative of malignancy in the target cells, as shown in Fig. 1.1 from Kun, Tu-nan et al. (2014). This could allow for efficient diagnosis in sensitive regions of the body, where biopsy could be harmful or even impracticable. Additional diagnostic information may be derived from the refractive index of the affected tissue, as the refractive power of abnormally oedematous tissue will differ from that of healthy tissue. This is demonstrated for different grades of tumour progression in Fig. 1.2

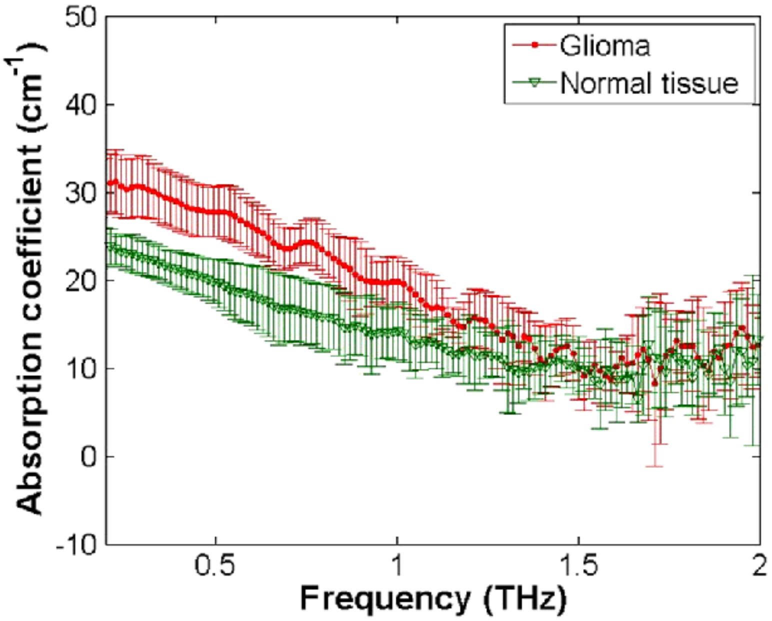

FIGURE 1.1: Comparison of THz radiation absorption levels of both malignant and normal glial tissue in the brain (Kun, Tu-nan et al. 2014).

In addition to the benefits of diagnosing cancer non-invasively, THz beams also show promise in other in-vivo oncological procedures. As described by

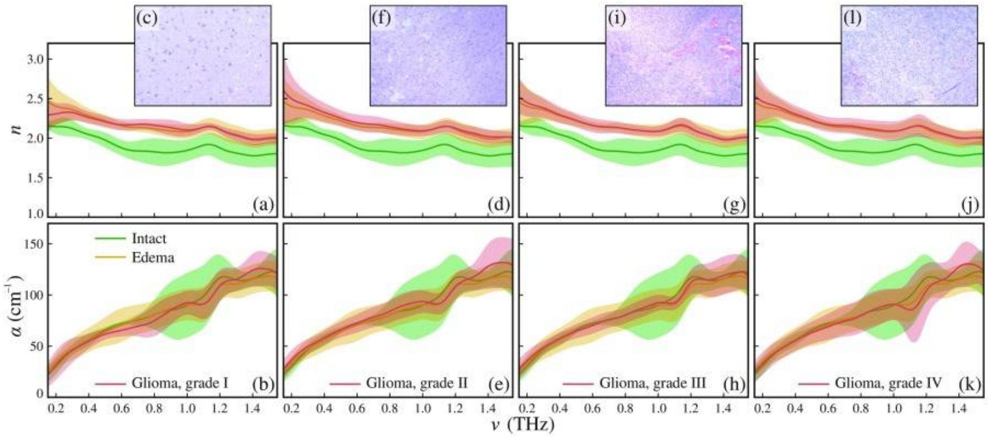

FIGURE 1.2: Comparison of THz radiation refractive index and absorption levels for different grades of glioma progression in human brain tissue (Gavdush et al. 2019).

Yngvesson and Bardin, (2021), compacted nanotechnological THz sources may be used intraoperatively to distinguish malignant tissue on a cellular level in real time, allowing the precise excision of tumours. This would render obsolete the traditional removal of a buffer margin of healthy tissue, which causes further damage and slows recovery, particularly for large masses.

1.2.2 Dental THz scanning

Research is underway into the future use of 3D spatial THz scanning to determine the enamel thickness and quality of teeth, without drilling or similar detrimental procedures. This would allow reinforcement of enamel before dentine or nerve exposure, as opposed to locating fully fledged cavities by direct visual inspection. Crawley and Longbottom (2003) explain an early implementation of this technology, using femtosecond laser pulse pumping. A later demonstration of a functioning THz dental analyser is shown in Fig. 1.3. The variable being measured is the intensity of the radiation returning to the detector, thus a lower dB value (blue) indicates greater absorption, whereas a higher dB value (red) indicates substantial penetration. The absorption is observably different in the healthy region H, compared to the carious (eroded) region C, particularly for the higher frequency images which show greater absorption in the damaged region.

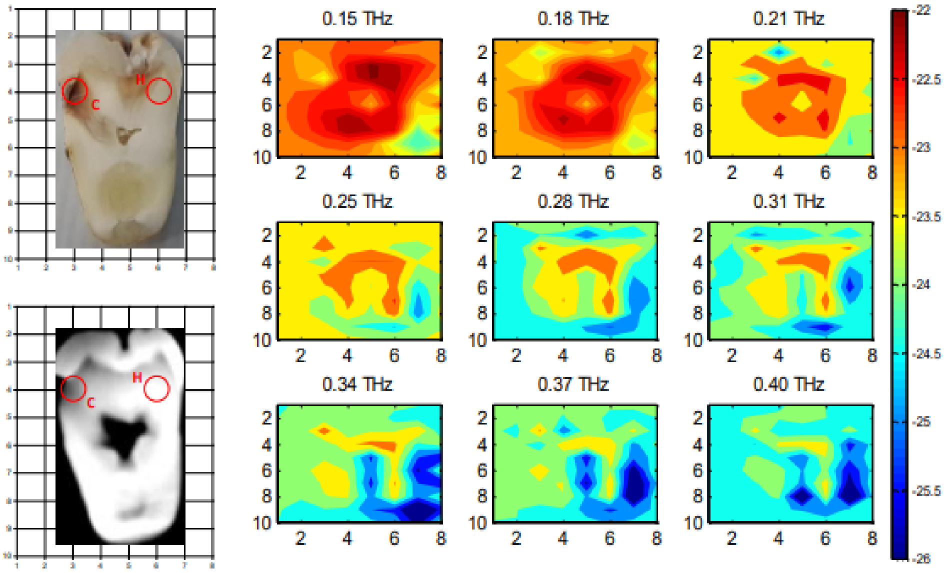

FIGURE 1.3: Comparison of healthy and damaged sections of a tooth slice, imaging using visible light (top left), X-Ray, (bottom left) and various frequencies of THz radiation (centre to right). (Karagoz, Kamburoglu and Altan, 2017.)

1.2.3 Pharmaceutical quality control

Submillimetre waves are critical to modern methods of controlling the quality of the delay coating on various orally administered pharmaceutical products. Delay coatings on tablets serve one of two purposes. Firstly, they may resist the acid of the stomach, instead breaking down in the more moderate pH environment of the intestines. Coatings may be employed either to protect the stomach from the active ingredient, or vice versa. Secondly, delayed release of medications with short biological half lives may allow fewer daily doses of the medication, reducing the burden on patients and increasing efficacy. These coatings must have a uniform and tightly toleranced thickness to perform their designated role in the body. This is difficult to measure conventionally, however the reflection of THz radiation from the outer and inner boundary surfaces of the coating gives an accurate thickness reading without damaging the product.

May and Evans (2010) showed the results of a sub-millimetre wave procedure for evaluating coating thickness in the 0.04 mm - 1 mm range. This technique employs a femtosecond THz pulse, partially reflected at the boundaries of coatings with different refractive indices. Differing angles and path lengths may then be converted to thicknesses by RADAR style timing of sections of the returning pulse. A complete scan of a tablet is shown in Fig. 1.4

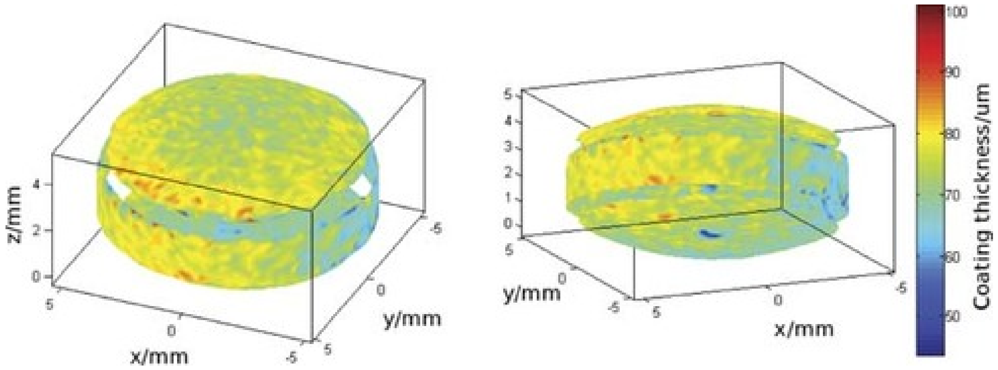

FIGURE 1.4: 3D rendered scan of coating thickness of a pharmaceutical product. (May, R. Evans, M. 2010)

1.3 THz security applications

1.3.1 Passenger and visitor scanning

Due to the ability of millimetre and submillimetre waves to pass through clothing with ease, and their harmless nature at low intensities, they are ideal for detecting people smuggling items through security checkpoints. The scanners can be visible or covert, and detect both metallic and non-metallic objects, unlike many previous detectors. This is a valuable advantage in the era of PLA printed and minimum metal firearms and munitions. Additionally, THz sources could yield characteristic signatures pointing toward certain specific substances being present, such as plastic explosives or chemical weapons (Kemp and Taday, 2003). One downside is that, in contrast to X-rays, the size and diffraction quality of the waves can make images quite poorly resolved when taken from several metres, showing an "area of interest" as opposed to an identifiable object. This, however, also has benefits from a privacy perspective, as these poorly defined images do not suffer from ethical restrictions due to clothing penetration.

1.3.2 Package interception

THz and high GHz screening are commonly employed in mail delivery centres to detect hazardous or illicit substances being sent by mail. Due to their shorter wavelength, the beams can make out more detail than microwave beams; unlike X-ray and γ scanners they are harmless to all parcel content, such as sensitive electronics. Passive detection can mostly negate the requirement for costly and sometimes dangerous manual inspection and the damage to packaging that this entails. Furthermore, such scanners can operate at amazing speeds, with some achieving 5 mm resolution on scanned goods at conveyor speeds of up to 15 m/s. This requires a scanning rate of 5000 passes per second for the diode beam (Shchepetilnikov et al. 2020). An example of scanned items revealing hidden contraband is shown in Fig. 1.5

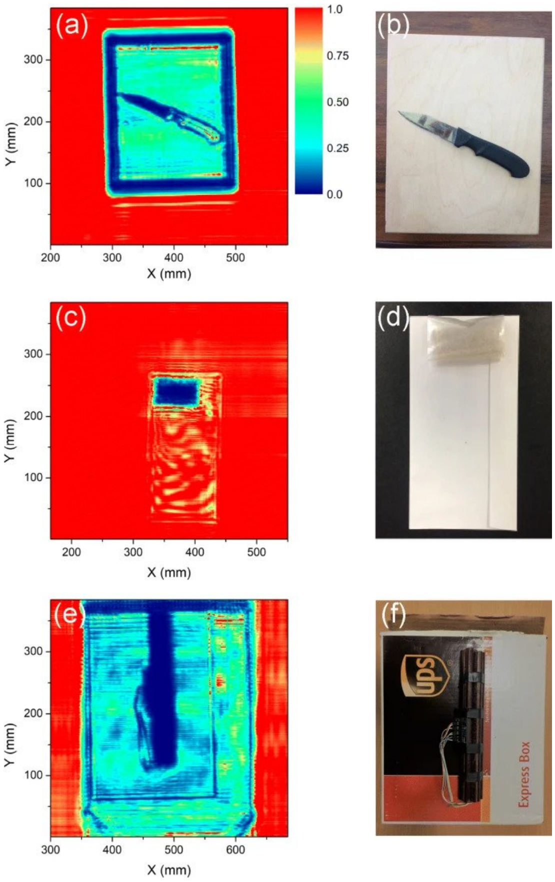

FIGURE 1.5: A variety of suspicious parcel contents imaged using a high speed automated THz mail scanner, with THz images on the left, and visible images for reference on the right (Shchepetilnikov, A. Gusikhin, P. et al. 2020).

1.4 THz communications applications

Communications development in the THz gap is extremely favourable for some applications, and all but impracticable for others. The primary limitation on the speed of wireless communications is the bandwidth and frequency of the transfer medium, the EMR signalling. Thus, each successive generation of wireless communication technology adapts to a higher frequency band of the EM spectrum and/or a larger bandwidth than the one before. Furthermore, larger bandwidths make massive communications in densely populated areas more easily managed, without overloading the spectrum. The relative data speeds and frequencies may be seen in Fig. 1.6 (table extract from Benisha, Thandaiah and Bai, 2019).

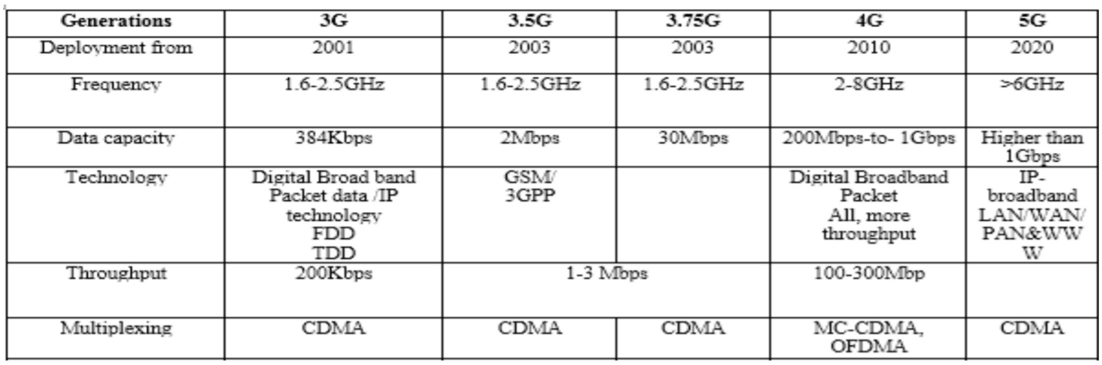

Generations	3G	3.5G	3.75G	4G	5G
Deployment from	2001	2003	2003	2010	2020
Frequency	1.6-2.5GHz	1.6-2.5GHz	1.6-2.5GHz	2-8GHz	>6GHz
Data capacity	384Kbps	2Mbps	30Mbps	200Mbps-to- 1Gbps	Higher than 1Gbps
Technology	Digital Broad band Packet data /IP technology FDD TDD	GSM/ 3GPP		Digital Broadband Packet All, more throughput	IP-broadband LAN/WAN/ PAN&WWW
Throughput	200Kbps	1-3 Mbps		100-300Mbp	
Multiplexing	CDMA	CDMA	CDMA	MC-CDMA, OFDMA	CDMA

FIGURE 1.6: Comparison of data transmission speeds and operating frequencies for successive generations of mobile networks.

5G technology broke into the millimetre wave region of the spectrum (3-30 GHz), one order of magnitude below the THz gap in frequency. This afforded substantial improvements in latency, carrying capacity and data transfer speed. However, it also incurred a heavy penalty in transmission distance, as shorter waves are much more easily attenuated in air in addition to their substantial vulnerability to absorption by rain, fog, leaves and other small obstacles. This resulted in many tiny, localized 5G boosters in urban centres, where 3G networks had used a few large towers. To create a subsequent large scale rollout of THz-based technology (6/7/8G?) would be to amplify both the advantages and drawbacks of 5G. Therefore, until our consumption of data as a society eclipses even that which 5G can support, research into large scale THz communications will be limited and theoretical. THz radiation is immensely sensitive to water vapour, fog and rain, propagating only a few metres in wet air. Thus, boosting coverage of such a short range signal source would be costly and technologically intensive. However, with the inexorable advance in data transfer and storage predicted by Moore’s law, we may in the future have to contend with these difficulties to achieve the information transfer speeds required for smart buildings, or even entire cities.

1.5 THz military applications

Similarly to the security applications mentioned earlier, THz sensing could be employed to identify a vast array of threats and contraband in a military setting. The ability to virtually penetrate skin, fabric and other dielectrics covertly could give early warning of weapons transport, suicide bombing or chemical attacks. Additionally, THz and millimetre wave imaging provides a safer alternative for minefield clearance, especially when minimum metal mines have been used. These charges are designed to avoid traditional metal detectors, making removal painstaking and dangerous. Their dielectric plastic composition and close proximity to the surface makes them vulnerable to identification at these frequencies, as described by (Du Bosq, T. Lopez-Alonso, J. and Boreman, G. 2014).

Due to the lower traffic requirements and the prioritization of other factors over cost, THz communication could be more rapidly feasible for military use than for general rollout. The highly directional beaming could improve security, while the large, high frequency bandwidth optimizes data transfer. THz beams also interact differently to centimetre RADAR upon reflection from obstacles, thus potentially unmasking stealth aircraft, if sufficient range can be achieved. THz range in space is practically infinite due to negligible attenuation and lack of water, so its future in space based RADAR and communications could also be promising.

THz technology is increasingly deployed in electromagnetothermal active defence systems (ADS), minimal harm directed energy weapons (DEWs) which use strong radiative fields at 95-100 GHz to heat the outer layer of the skin of anyone in their vicinity to around 60 degrees Celsius. This produces a highly discomforting yet relatively harmless burning sensation. These systems are much less damaging than conventional kinetic/chemical less lethal munitions, and can be mounted on vehicles to manage crowds, disperse riots, or clear paths for speeding emergency service convoys. Additionally, static units can be used at checkpoints and compound entrances, providing protection from bombers and storming. Given that ADS does not blind, maim or kill, it does not contravene Geneva Convention restrictions on DEWs, as such it is legal to deploy in combat. A discussion of this and similar technologies from both physical and ethical viewpoints is provided by (Altmann, 2008).

1.6 THz radiation in Astrophysics

1.6.1 Sources and observation

The THz part of the spectrum in astronomy is primarily relevant to "cold" observations. Matter emitting at these frequencies is typically sparse, molecular and non-ionised, far from any stellar winds or accretion zones. Interstellar gas and dust at 1-170 K will have a blackbody peak in the THz region according to Wien's law, as discussed previously. Cold, dense gas in nebulae will also have strong molecular transition lines in the THz region. The low temperatures and densities make observation difficult at higher energies, as emission of energetic photons is minimal. Studying these sources at THz wavebands can give insights into the potential conditions of the protosolar nebula prior to the initiation of gravitational collapse 5 Gy ago (Walker, 2020).

THz observations are broadly split into space-based, balloon-based and ground-based. As shown in Fig 1.7, atmospheric water vapour vastly diminishes the power of extraterrestrial THz emission at terrestrial altitudes. The main window for ground-based observation is near the millimetre wave-THz boundary, which is a region of particular importance due to the presence of the thermal peak of cosmic microwave background (CMB) emission within this range. With its 2.7 K temperature, the relic radiation easily passes through the upper layers of the atmosphere. This allows for ground- and space-based observing missions to compete for discoveries. Due to the low luminal flux of THz sources and their position on the EM spectrum, observations are easily affected by thermal sources, typically blackbody emission, within the apparatus itself. Minimizing thermal noise usually involves employing cryogenic techniques to reduce the ambient temperature of the environment containing the equipment. Moderate cryogenic temperatures can reduce the total flux of photons substantially. Additionally, high performance cooling ($T < 1$ K) can shift the thermal emission peak below the THz spectrum, further decreasing noise.

1.6.2 Interferometry with THz radiation

THz radiation is situated at the boundary between the traditional optical and radio bands. As such, the higher spatial resolution of visible light meets the suitability for interferometry of radio at this interface. Radio observations have

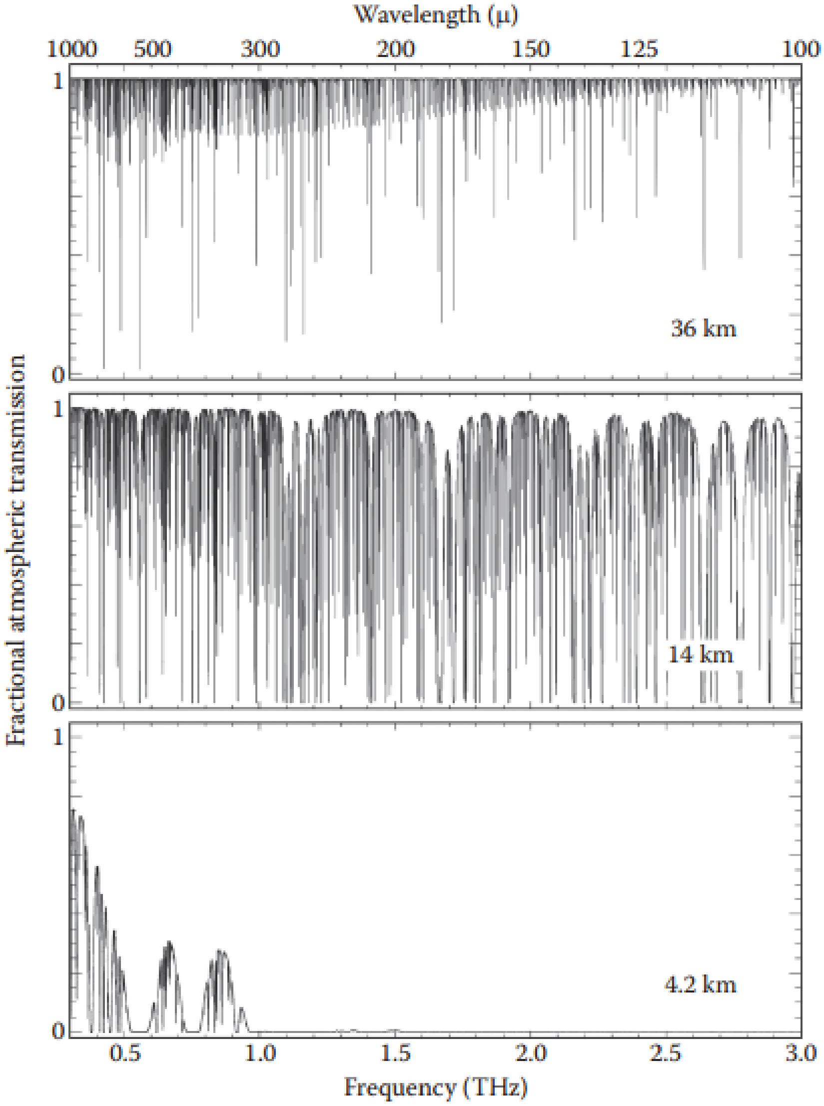

FIGURE 1.7: The transmission coefficient of radiation across the THz spectrum for three sample altitudes (Walker, 2020).

long used Very Long Baseline Interferometry (VLBI) as a means of improving resolution; a single large ∼10 m reflector has an aperture of just 30 λ at 1 GHz. The VLBI technique involves the interference of signals from telescopes at long distances from one another, to achieve an angular resolution equivalent to that of an aperture of diameter equal to the distance separating them. At radio frequencies, VLBI is used to achieve resolutions comparable to those possible with single aperture systems in the visible. However, in the THz region, VLBI can reach effective angular resolutions much greater than those permitted by basic optical observation.

A spectacular example of the power of THz VLBI was unveiled to the world

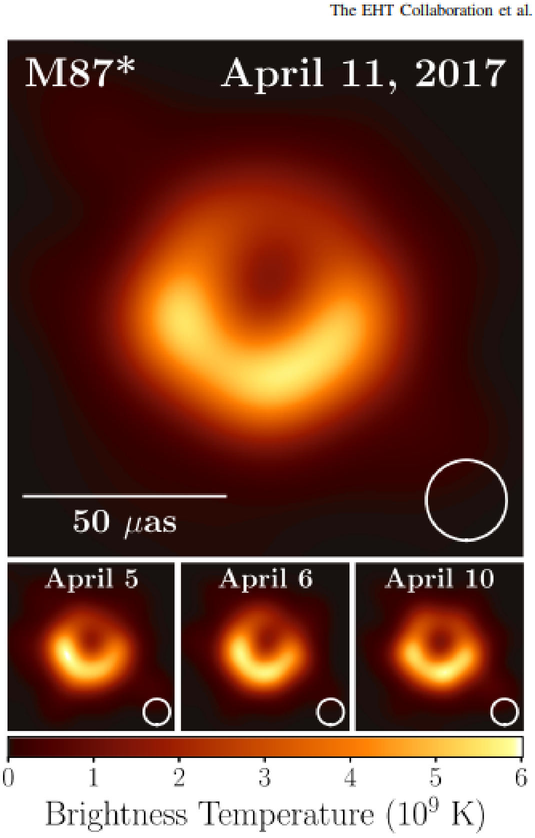

FIGURE 1.8: THz interferometric image of Pōwehi, the central SMBH of Messier 87, with surrounding jets and shadow (Akiyama et al. 2017).

in 2019, when a global team of scientists published a series of papers concerning the direct imaging of the core of the Messier 87 giant elliptical galaxy. This central mass is a black hole 6.5 billion times the mass of our Sun, with an event horizon diameter of approximately 240 AU (Smith 2021). The Event Horizon Telescope (EHT) collaboration used eight telescopes around the Earth to create an effective aperture of over 10,000 km, and a corresponding resolution (at the observing frequency of 230 GHz) of 25 microarcseconds. This is equivalent to resolving individual pebbles on the lunar surface from Earth, over a thousand times the angular resolving power of the Hubble Space Telescope. This marvel of imaging capability was used to probe the region around the supermassive black hole (SMBH) event horizon at the centre of Messier 87. The event horizon itself, despite its massive size, subtends just 15 microarcseconds at the Earth, however its shadow, and the brilliantly glowing gas surrounding it, are within the resolving limit of the EHT. A prolonged data reduction effort was required to deconvolve the interferometric data, with many terabytes coming from each of the telescopes. The result was the first ever true photograph of a black hole, shown in Fig. 1.8. The asymmetric disc shows a Doppler shift from spin, while the diameter of the dark ring yields information regarding the evolution of jets around accreting black holes.

1.7 Summary

This thesis is concerned with the optical and electromagnetic modelling of astronomical instrumentation operating at GHz and THz frequencies. The techniques and software developed could also be applied in other fields of science and technology. In this chapter I have discussed some of these applications in detail, namely, those pertaining to medicine, security and communications. Astrophysical applications were also briefy mentioned, and will be discussed in further detail in subsequent chapters.

1.8 Layout of the thesis

This chapter has given a brief introduction to research in the GHz and THz region of the electromagnetic spectrum, as background and to give context to what follows. In Chapter 2 I describe optical analysis techniques at these frequencies, in particular with the commercial software GRASP. These techniques are used to propagate beam patterns from feeds through astronomical optical systems and on to the sky. I use as an example modelling work I carried out on the Pickmere telescope. For the remainder of the thesis I concentrate on the feeds themselves by describing work carried out on corrugated horn designs for the QUBIC and ALMA telescopes. In Chapter 3 I give a description of these two telescopes. In Chapter 4 I describe the technique of electromagnetic mode matching and use our in-house software PyScatter to mode the corrugated horns in QUBIC. I investigate whether their operating frequency band could be increased. Chapter 5 discusses work done on the design of corrugated horn antennas for a possible future combined ALMA observing band. In Chapter 6 I describe an extension to PyScatter that I developed to allow it to model offsets in corrugated horns, something that is useful for the platelet horn array design of QUBIC. Finally, an overall summary and suggestions for future work are given in Chapter 7.

Chapter 2

Optical Analysis

2.1 Introduction to Physical Optics

2.1.1 Introduction

In this chapter I will briefly describe Physical optics (PO) and Gaussian beam modes, two methods commonly employed at GHz and THz frequencies to propagate beams virtually through models of astronomical telescopes. I will use the Pickmere telescope as an example as our colleagues in Manchester University are developing feed arrays for a possible upgrade to this instrument.

2.1.2 Description of physical optics and the physical theory of diffraction

PO is a method of modelling the propagation of electromagnetic radiation through optical systems. It contrasts with ray optics in that it considers the wave nature of light, as opposed to treating the light as a stream of particles or rays travelling through space. The beginnings of PO lay with the demonstration of the wave nature of light by Thomas Young, with the famous double slit experiment. Previously, light had been assumed to have a solely corpuscular character. Another great step forward was made almost simultaneously by William Herschel, when he used a prism to measure the temperature of different colours of the visible spectrum. Contrary to expectation, a considerable temperature rise was observed beyond the red of the visible spectrum. This constituted the first experimental detection of sub-optical frequencies, whereupon the wave nature of light becomes more apparent.

Augustin Jean Fresnel began the study of light as a wave in earnest. He characterised the circular elliptical and linear polarizations of light, as well as investigating the physics of light diffracting around thin wires and similar obstacles. This was published in his 1818 work "Memoir on the Diffraction of Light" (Crew et al. 1900). Additionally, Fresnel correctly predicted the existence of the Poisson spot, a bright central peak in the shadow cast by an opaque object illuminated by parallel light rays. This is caused by diffraction around the edges of the obstacle and subsequent constructive interference, as described in (Gaal, 2016).

The initial theory of physical optics was pioneered by the German physicist Gustav Kirchhoff in the late 19th century. He produced an integral relation to describe diffraction mathematically (Kirchhoff, Hentschel and Zhu, 2017). For a far field monochromatic source of electromagnetic radiation, the integral is shown below, Eqn 2.1 (Buchwald, J.Z, Yeang, C.P, 2016):

$$U_p = \frac{1}{4\pi} \oint_S \left[U \frac{\delta}{\delta \hat{n}} \left(\frac{e^{iks}}{s} \right) - \frac{e^{iks}}{s} \frac{\delta U}{\delta \hat{n}} \right] dS \tag{2.1}$$

This equation calculates U_P, the complex amplitude of an electromagnetic wave at P, a point displaced from a surface S by a distance s, while $\hat{n}$ represents a unit vector normal to S. U represents the spatial part of the relevant solution to the scalar wave equation, while k is the wavevector, and i the imaginary unit.

Ray optical approaches are sufficient when the size of the optical components are very large with respect to the wavelength of the incoming light. This is usually the case with visible spectrum lenses and mirrors. For a typical visible setup, the optical elements have physical size $D_\mathrm{e} \approx 10^{-1}$ m, compared to $\lambda \approx 10^{-6}$ m. Thus, $D_e \approx 10^5\ \lambda$, a ratio so high as to render diffractive and polarising effects negligible for most purposes. All interactions in such systems consider solely the particle nature of light and deal primarily with classical reflection and refraction, as defined by Euclid and Snell, respectively.

In the case of microwave and radio optics, it is sometimes the case that $D_e \approx 10^{-1}\ \lambda$ or $10^{-2}\lambda$. In these cases, PO is required to correctly calculate the interaction of incident light with the element, including the polarization and diffraction effects which cannot be computed by ray optics. In essence, PO analysis acts as an intermediary, between the simplistic views associated with ray optics and the complex mathematical rigour of an analytical electromagnetic solution. Two modified equations were developed to approximate the exact approach used by Kirchhoff, as is required in systems with any level of geometric complexity. These are the Fraunhofer and Fresnel integrals. Fraunhofer diffraction is used to model systems having an aperture size much smaller than the optical length of the system. Fresnel diffraction is used when this assumption does not hold true. In the case of Gaussian beam optics, expanded on later in this chapter, Fresnel diffraction would assume a finite radius of curvature of the Gaussian beam upon reaching a diffracting surface, while Fraunhofer would assume the radius of curvature to be infinite – a flat phase beam.

Some PO software evaluates the Fresnel and Fraunhofer integrals to determine the shape of beams propagated through optical systems. The accuracy of the estimate depends on the complexity allowed for in the integration; as is common when modelling physical systems numerically, a better estimate of reality incurs a sharp increase in computational power requirements. By contrast, other platforms use approximated solutions of Maxwell's equations to gain more accurate simulations, with further computational cost. An example is GRASP, which is described in more detail later in this chapter. This technique may also be described as physical optics; hereafter the term shall refer to the technique used by GRASP to evaluate surface currents.

The theory of PO is designed to model sources illuminating smooth geometric surfaces without discontinuity or superposing rays. The analysis breaks down at the edges and focii of real reflectors. For finite reflectors with physical boundaries and focal properties, another approach is required to supplement this method, the physical theory of diffraction (PTD). This theory is a method for approximating the scattering of electromagnetic radiation from the edges and corners of real surfaces. It is also frequently required in the vicinity of caustics, regions where light rays cross, such as at a real focal point. (Ufimtsev. P, 2014).

PTD was first developed by Pyotr Y. Ufimtsev in the 1960s; it was subsequently instrumental in the development of RADAR evading stealth aircraft (Ufimtsev. P, 1980). This theory extended the nineteenth and twentieth century work done in the field of mathematical diffraction. Few perfect solutions existed for diffraction at a boundary, all required very simple geometry as well as being computationally demanding to perform when the object was large compared to the wavelength of the incident light. As in the case of PO, PTD bridged the gap between oversimplified approaches and precise mathematical solution (Weinmann, 2006). The most basic unit element of PTD is the perfectly conducting infinite half plane (Jones. D.S, 1896). By considering the profile of the edge of this plane, approximations can be drawn for more complex structures numerically. PO and PTD are combined in GRASP to render a full representation of the behaviour of EM radiation as it interacts with reflector surfaces, by evaluating surface currents and edge contributions. The light striking a conducting reflector induces as a surface current. This is due to the negligible skin depth of conducting materials, preventing penetration of the light into the surface.

2.1.3 TICRA GRASP software description

GRASP [1] is an industry standard software suite (Sudhakar, Rao et al. 2013) aimed at the sub-infrared research and development market. It is one of the signature products of the Danish computational optics firm TICRA, along with other microwave analysis platforms such as CHAMP and POS. The function of GRASP is to determine the currents generated by light passing through an arbitrarily complex optical system composed of individually instantiated components, using PO and PTD.

GRASP analysis centres on a few broad classes of geometrical and electrical objects, which can be combined sequentially in command routines. Geometrical objects include rims, struts, surfaces and backstops, amongst other elements. These are the items which will interact with microwave radiation in the simulated environment. Each one possesses several degrees of freedom, which may be chosen at will to specify the shape and properties of the object. Surfaces are infinite geometric continua, usually planar, parabolic, hyperbolic, quadratic or spherical, which can be simulated using a variety of materials. Each surface shape has a set of specific constants which are set to define it uniquely. For example, in the case of a hyperbolic surface, the focal and vertex distances are required. Rims are two-dimensional boundaries imposed on surfaces when creating reflectors. Rims may be placed symmetrically onto the surface, creating an on-axis reflector, or asymmetrically, creating an off-axis reflector. Struts are included as a separate category, they may be constructed polygonally or canonically; the latter is more computationally demanding, required principally when the strut diameter approaches the shortest wavelength input into the system.

Electrical objects are objects which are not instantiated into the simulation, they do not interact with incident EM radiation. This category includes

---

[1] ticra.com/software/all-software/

sources, PO analyses and outputs. Sources are emitters of EM radiation. The most prominent types are Gaussian beams and plane waves. The physical size of the source can be specified, as can the wavelength, initial amplitude and polarization of the signal. Additionally, provision is made for the inclusion of radiation at a series of different frequencies, which are propagated simultaneously. PO analyses are the PO/PTD routines associated with reflectors and other geometric entities. They represent the diffractive and reflective effects that the associated entity will have on incoming radiation. When building a sequential series of commands, the PO analysis of each reflector is called into the routine each time light passes it. By altering the amount of detail included in the analysis, the balance of accuracy and computational effort may be adjusted. In GRASP, this is modulated somewhat indirectly by the number of PO points and number of 'passes' commands.

Outputs are the user interface with simulation results. They consist of two categories, cuts and grids. Cuts are one-dimensional slices across the field amplitude in a region. Grids are two dimensional gridded shapes which show a heatmap or contour plot of the electric field across the region being mapped. The sampling rate of both cuts and grids can be chosen at will. Cuts can produce very high resolution while requiring little computational effort, with precise intensities along a line across a field. Additionally, multiple cuts can be taken at varying angles around a central point. This is useful for isolating effects due to polarization, which often possess angular dependence. Grids are critical to providing a visual representation of the propagation of light through a region. They may be represented as coloured intensity maps, known as heatmaps. These show results quickly and efficiently, and can be plotted linearly or logarithmically. However, due to the two-dimensional nature of the grid structure, the plotting time is considerably greater than for a cut or small series of cuts at a given resolution.

2.2 PO modelling using GRASP

2.2.1 Introduction

The work described in this section was carried out as part of a collaboration with Manchester University. As part of this collaboration, focal plane patterns from corrugated horns and phased arrays are propagated through telescope optics and out onto the sky. Chapter 5 describes the design of corrugated

FIGURE 2.1: The Pickmere telescope (© Benjamin Shaw (cc-by-sa/2.0))

horns. Here the Pickmere telescope is analysed as an example of how telescopes are modelled. In the future, phased arrays will be designed in Manchester to be used with this telescope.

2.2.2 The Pickmere telescope

Pickmere is a 25-m diameter Cassegrain radio telescope, located near Knutsford in Cheshire. It forms part of the seven element array, stretching for 200 km across England. Pickmere was built in 1980, and is curated by the Jodrell Bank astronomy collective. The telescope is designed to detect a wide range of frequencies, from 150 MHz to 24 GHz. The lower bands require interferometry with other telescopes to produce meaningful data, as the telescope diameter is only about 12λ at the lowest frequency (CRAF, 2022). A photo of the telescope is shown as Fig. 2.1

The model of Pickmere telescope components was based on schematic diagrams of the reflector and support structure. As can be seen in Appendix A, these diagrams showed the relative sizes and positions of the primary and secondary reflectors and associated instrumentation and armature. As the source document was compiled in 1970's Britain, all units were imperial and had to be converted for calculations. The following dimensions for the telescope components were obtained by direct inspection of the schematics given in Appendix A, or where the measurement was not explicitly given, by trigonometry using the available information.

Primary reflector

Profile: Parabolic

Diameter: 28.04 m

Bowl depth: 4.34 m

Focal length: 8.99 m

Secondary reflector

Profile: Hyperbolic

Diameter: 2.512 m

Depth: 0.5842 m

Focal length -0.6353 m

Armature

Four struts supporting secondary

Strut profile: cylindrical

Strut length: 10.9 m

Strut thickness (diameter) 0.356 m

Cylindrical structure above secondary, aligned and centred on optical axis

Cylinder dimensions, radius 2.512 m, depth 0.914 m

General information

Height of the prime focus above the bowl: 1.476 m

Radial distance between strut bases and prime axis: 7.86 m

Separation of secondary mirror from cylinder: 0.63 m

A few pieces of information that are not easily obtained from the graphics are the profile of the conical strut heads and the focal and vertex distances of the secondary mirror. The strut heads, where the strut connects to the armature of the secondary mirror, are a very small component of the whole and are assumed to be insignificant in this initial analysis. The focal and vertex distances are calculated as described below.

The system set-up and optical simulation were performed with the GRASP radio astronomy package. To set up the system, the secondary vertex and focal distances were first calculated by fitting a hyperbolic surface to the physical parameters given in the schematic as follows: two planes were placed where the upper and lower edges of the secondary mirror are positioned in the schematics shown in Appendix A. These were just ghost markers, not included in the GRASP commands. The focal and vertex distances of the mirror could then be adjusted such that the mirror fits correctly inside the cylindrical volume specified by the given mirror radius and the two planes. There were two variables, the focal length and the vertex distance. These could be derived from the position of the marker planes, together with the radius and depth of the mirror. The vertex distance was found to be 6.35 metres, and the focal distance 7.385 metres. The antenna profile in GRASP is shown as Fig 2.2.

2.2.3 Modelling technique

When the model had been constructed in GRASP, an on-axis plane wave source was input at the aperture of the telescope. A grid at the focal point recorded the shape of the focused beam of radiation. For quicker testing of mirror properties, a copy of the model was made, excluding the struts and cuboid. Additionally, another copy had its commands reversed, to check the collimation of the beam output by the main reflector from a source at the focus. In effect, they test the system in both transmitting and receiving mode, which can be assumed equivalent by the reciprocity theorem applied to antennae, as described in (Balanis, 2016). It was found that the focussed beam had an Airy type pattern, as shown by Fig. 2.3. The cut across this beam, shown as Fig. 2.4, more clearly shows the profile of the beam. A 20 dB reduction from boresight intensity was observed at just under 40 cm from the main lobe peak. Inclusion of struts in the full simulation proved too computationally intensive to be undertaken in reasonable time, however the effect of the struts, armature

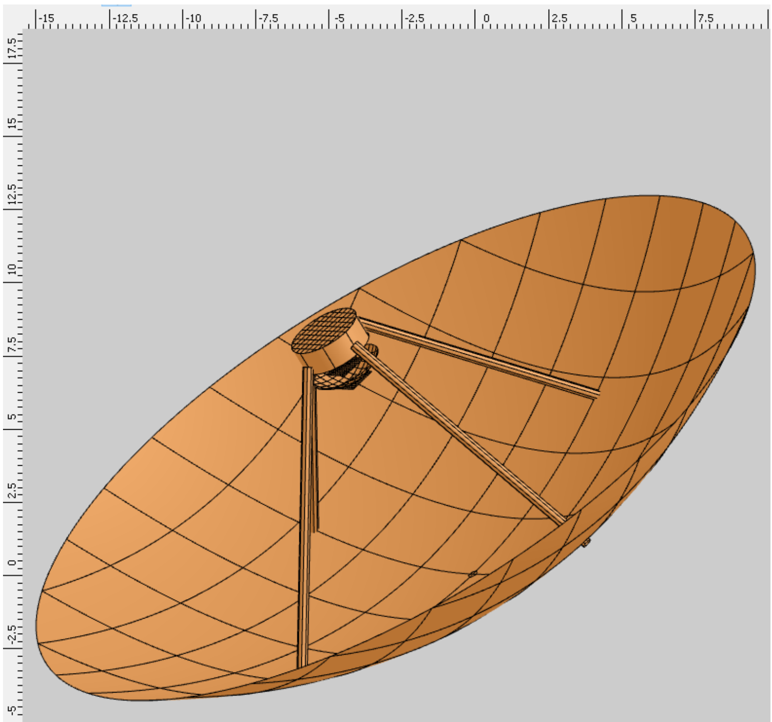

FIGURE 2.2: Pickmere optics as viewed in the GRASP antenna pane.

and secondary mirror on a free Gaussian beam is shown as Fig. 2.5. The effect of the four struts and the secondary mirror shadow are clearly defined. The outer fringes of the pattern are highly comminuted, potentially explaining the substantial simulation time. The strut calculation was done by propagating a Gaussian beam from a distant point, past the struts, armature and secondary mirror, and onto a grid where the primary mirror lies. It is essentially a map of the incident power pattern on the primary from the distant Gaussian source.

For the reverse simulation, a Gaussian beam of a size similar to the focussed beam found above, was propagated from the focus through the telescope and out on to the sky. The Gaussian beam was defined in GRASP using taper and taper angle by assigning a -10 dB power reduction at an angle 10° from boresight. To verify that the beam had been defined correctly, a 20 m × 20 m grid was placed 100 m from the focus, centred on axis. The mirrors were not included, so as to test solely the dispersion of the freely propagating beam. A cut was also placed across the horizontal axis of the grid. The angle subtended by the edge of the grid at the source (100 m away) was $\tan^{-1}\frac{1}{5} = 11.3^\circ$. Thus, from the beam taper specified, an intensity reduction of approximately 11 dB would be expected across the test cut, which was verified by the simulation.

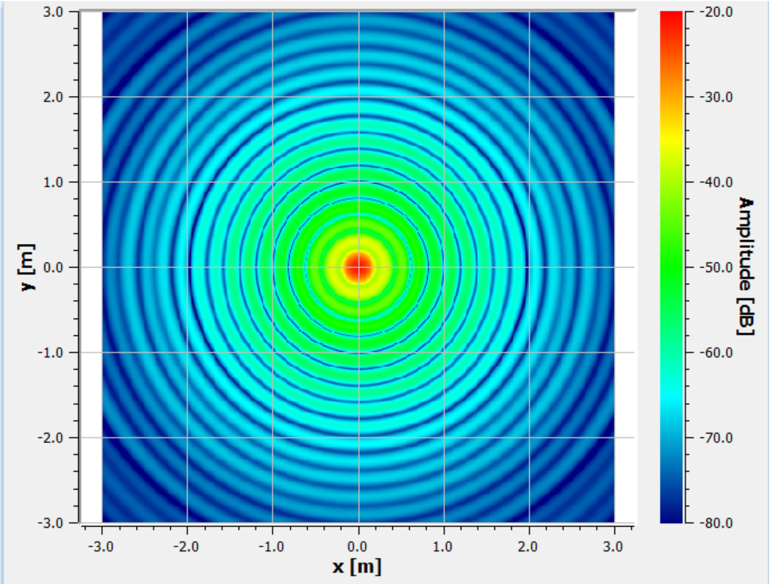

FIGURE 2.3: Beam pattern on the Pickmere focal plane from a plane wave source. The two mirrors were included in the simulation.

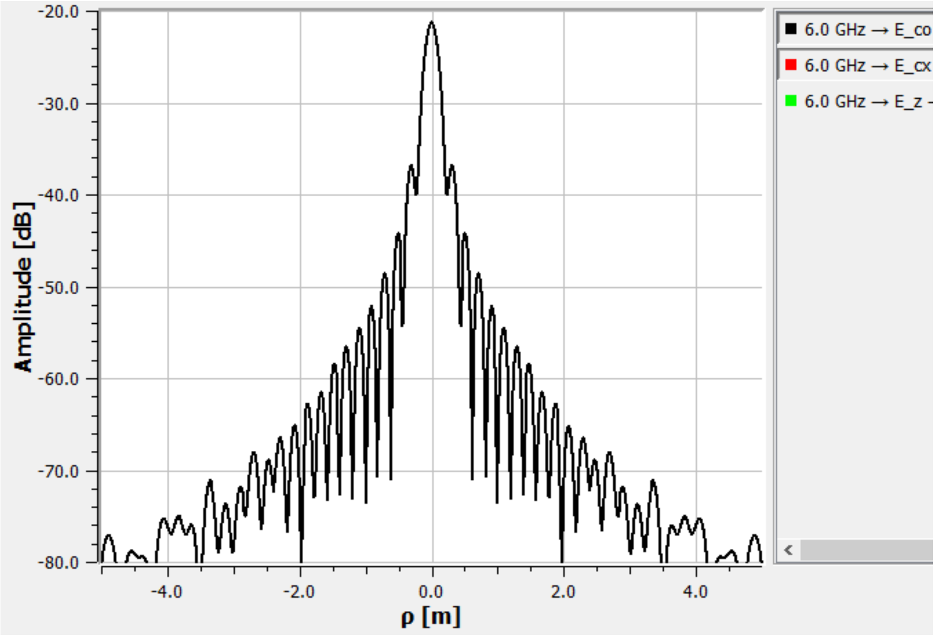

FIGURE 2.4: A cut of the focal plane beam pattern in Fig. 2.3

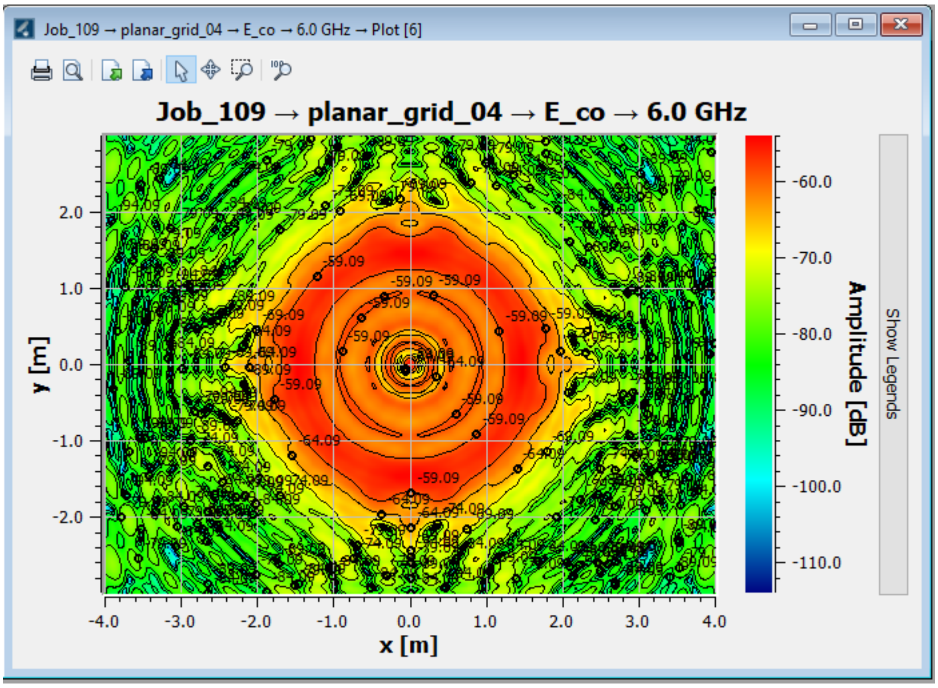

FIGURE 2.5: Effect of the struts, armature and secondary mirror shadow on a beam from a distant Gaussian source.

The cut and grid outputs are supplied as Fig. 2.6 and Fig. 2.7, respectively. The peak of the focussed beam from Fig. 2.3 is 30 dB higher than the peak of the unfocussed beam, implying a gain of 10^3 on the propagation axis from using the mirrors.

Upon verification that the beam had been defined correctly the hyperbolic mirror was reintroduced into the GRASP simulation. This produced an elliptical beam, although the input beam and mirror were both radially symmetric about their principal axis of propagation. The only physical explanation for this was polarization effects, so four separate polarisations of the input beam were run through the same simulation. This allowed observation of the effect of polarization on the transverse beam profile. When linear polarization was used, elliptical co- and cross-polarised beams were found, the orientation of which changed with the axis of polarization. When circular polarization was used, the co-polarised beam was elliptical and oriented along the y-axis and the cross-polarised was elliptical and oriented along the x-axis. These then swapped when the direction of circular polarization was reversed. This effect was corrected when the primary was introduced, yielding a circular beam once more at the telescope aperture. The beam was then propagated 50 m from

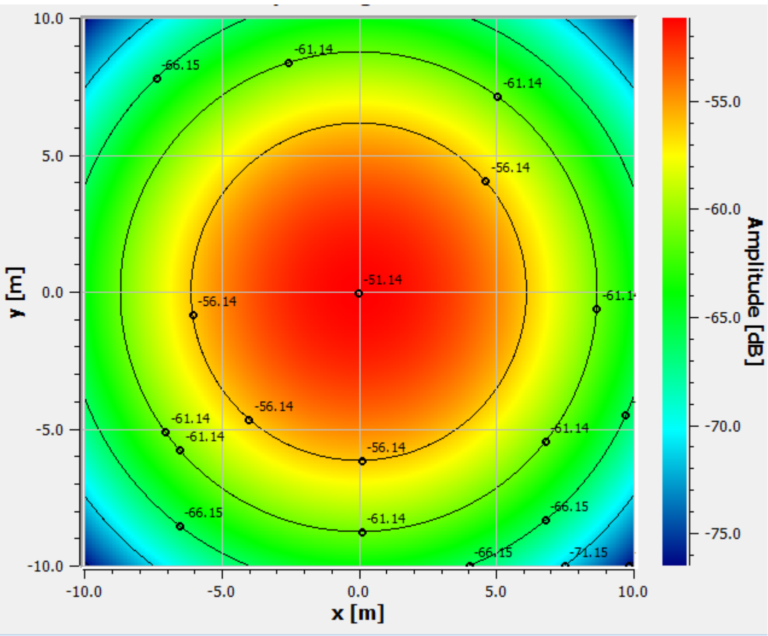

FIGURE 2.6: Grid showing profile of the input beam pattern, without mirrors

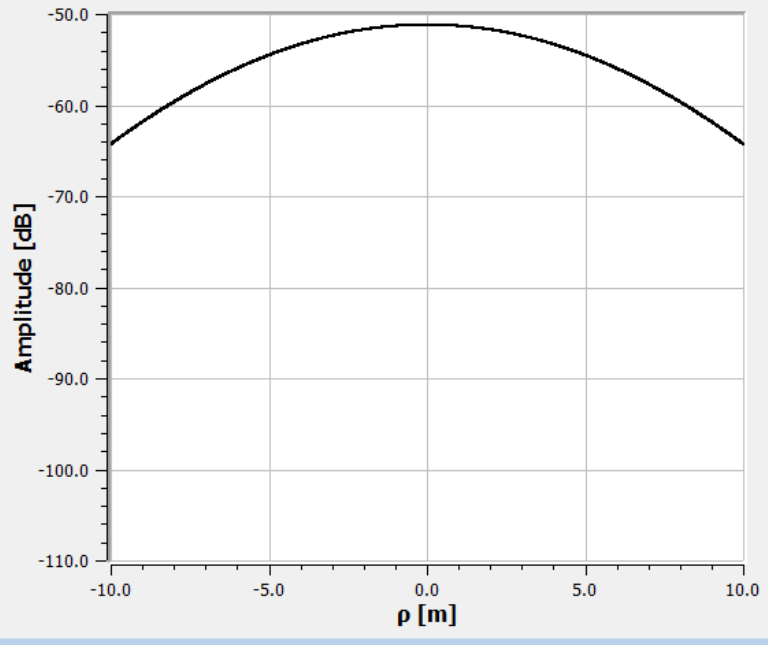

FIGURE 2.7: Cut across input beam pattern, without mirrors.

the telescope to yield a beam of radius 7.8 m and flat phase. The beam radius changed little beyond this, even after propagation of several km.

2.3 Gaussian beam mode analysis

2.3.1 Initial Gaussian beam

It was decided to carry out a Gaussian beam mode analysis of a simplified model of the Pickmere telescope to use as a comparison for the full PO/PTD model. This analysis models the telescope beam as a Gaussian beam which is a solution to the paraxial wave equation. Off-axis mirrors are approximated by their on-axis lens equivalent. This analysis does not have the rigour of PO, but nevertheless provides a good approximation for simple systems, and is much quicker to perform. A program was required that would firstly produce a Gaussian beam, and then propagate the beam through a series of optical components via an ABCD ray matrix analysis. Additionally, it was useful to plot the profile of the beam as it passed each component.

To start, a routine was constructed to display a cut of a Gaussian beam, propagating in free space, along the transverse and longitudinal axes. The program was based on Eqn. 2.2, the Gaussian intensity profile equation:

$$I(z,r) = I_0 \left(\frac{w_0}{w(z)}\right)^2 \exp\left(\frac{-2r^2}{w(z)^2}\right). \tag{2.2}$$

I_0 is the initial boresight intensity of the Gaussian beam, while $I(z,r)$ is the intensity in the transverse plane after propagating a distance z from the origin. $r^2 = x^2 + y^2$. Likewise, w_0 denotes the initial width of the beam, and $w(z)$ the width at a propagation distance z. $w(z)$ can be calculated using 2.3, from Goldsmith (1998)

$$w(z) = w_0\sqrt{1 + (\frac{\lambda z}{\pi w_0}^2)}. \tag{2.3}$$

By evaluating $I(z,r)$ at every point on an xy grid, for a particular value of $w(z)$, the entire transverse profile of a beam of initial width w_0 could be evaluated at any specific z. To obtain a cut along the longitudinal plot, a set of points were chosen on the xz plane with $y = 0$. Fig. 2.8 shows such a transverse and longitudinal plot of a propagating Gaussian beam.

The curvature of the Gaussian beam wavefront is described by a phase term

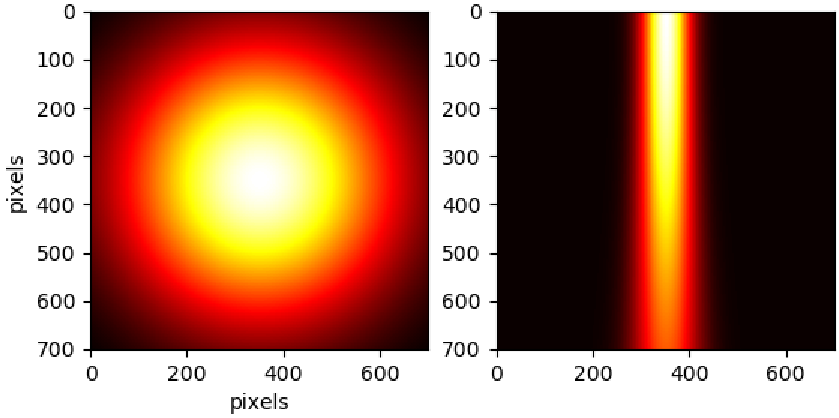

FIGURE 2.8: Transverse (left) and longditudinal (right) beam intensities for free space propagation using the Matplotlib heatmap function. The direction of longditudinal propagation is vertically downward.

$$\exp\left(i\frac{kr^2}{2R(z)}\right), \tag{2.4}$$

where k is $2\pi/\lambda$. In addition to the width or waist radius $w(z)$, it is useful to keep track of the phase radius of curvature $R(z)$ of the beam. This can be done using (Goldsmith, 1998)

$$R(z) = z + z\left(\frac{\pi w_0^2}{\lambda z}\right)^2. \tag{2.5}$$

2.3.2 ABCD matrices for Gaussian beams

The next program aimed to pass the Gaussian beam through two lenses designed to mimic the action of the Pickmere mirrors, and through the associated free spaces.

ABCD ray matrices are a tool for describing optical elements using a matrix, and combining the effects of multiple elements using matrix multiplication (Mansell et al. 2007). In ray optics the ABCD matrix describes the effect of an optical element on an input ray's position and slope. In the case of Gaussian beams, the same matrices can be used to describe the effect of the element on its Gaussian beam parameter $q(z)$. This complex number combines $R(z)$ and $w(z)$ into a single descriptor of the beam properties

$$\frac{1}{q(z)} = \frac{1}{R(z)} - i\frac{\lambda}{\pi w^2(z)}. \tag{2.6}$$

The real component of q pertains to the radius of curvature R, and the imaginary to the beam width w.

A single matrix is typically used for each optical component in a system, including free spaces. For any complex optical system, the overall ABCD matrix can be constructed from the individual element matrices by matrix multiplication in reverse order i.e. the matrix for the last optical element first. The ABCD matrix is then used to transform the complex q value of the beam across the optical element, according to Eqn. 2.7

$$q_{out} = \frac{Aq_{in} + B}{Cq_{in} + D}. \tag{2.7}$$

Once q_{out} is known, $w(z)$ and $R(z)$ are easily obtained from Eqn. 2.6. Lens matrices leave w unchanged but modify R, while free space matrices modify both R and w. The form of free space and lens matrices are shown below as Eqns. 2.8 and 2.9, respectively, where D represents the distance propagated through free space, and f the focal length of the lens. The set of ray matrices used to propagate radiation through the Pickmere system is shown in Eqn. 2.10. The matrices represent the system elements as follows, beginning from the rightmost matrix, due to the reverse order of the matrix multiplication. The first propagation matrix takes the ray from 100 m away (arbitrary long distance to yield a reasonably flat beam) to the surface of the primary. The first lens matrix represents the primary mirror, with 0.111 being the inverse of its focal length in meters. The third matrix is the propagation from the surface of the primary to the surface of the secondary. This is smaller than the focal length of the primary, thus, the beam still has substantial width upon striking the secondary. The second lens matrix represents the second mirror, with -1.574 as its inverse focal length. Finally the last propagation takes the ray from the surface of the secondary to the system focus, at a distance of approximately 1.5 m above the centre of the primary, on axis.

$$\begin{pmatrix} 1 & D \\ 0 & 1 \end{pmatrix} \tag{2.8}$$

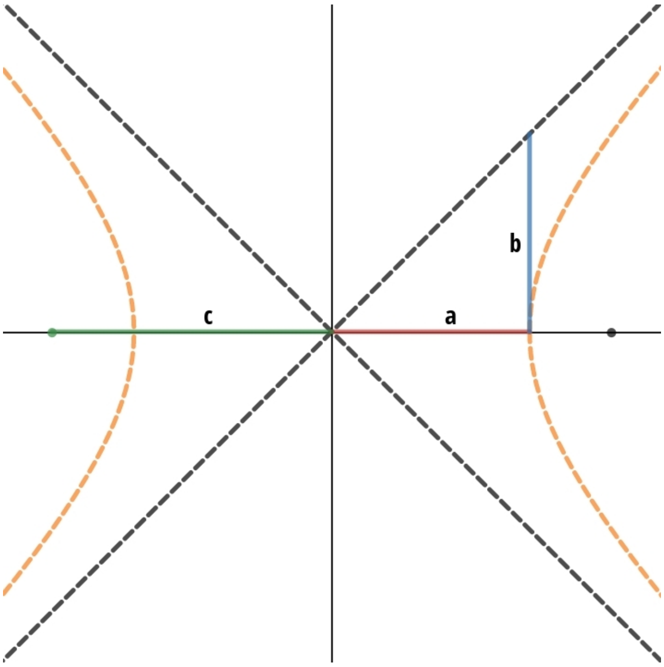

FIGURE 2.9: Hyperbola, showing vertex distance a, asymptote distance b and focal distance c.

$$\begin{pmatrix} 1 & 0 \\ \frac{-1}{f} & 1 \end{pmatrix} \tag{2.9}$$

$$\begin{pmatrix} 1 & 6.94 \\ 0 & 1 \end{pmatrix} \begin{pmatrix} 1 & 0 \\ -1.574 & 1 \end{pmatrix} \begin{pmatrix} 1 & 8.4 \\ 0 & 1 \end{pmatrix} \begin{pmatrix} 1 & 0 \\ -0.111 & 1 \end{pmatrix} \begin{pmatrix} 1 & 100 \\ 0 & 1 \end{pmatrix} \tag{2.10}$$

In the case of the Pickmere parabolic mirror, the focal length could be obtained easily from the original diagram. For the hyperbolic mirror, however, the conversion was less obvious. The geometric parameters of the hyperbolic mirror were required to determine the effective focal length of the equivalent lens, these are displayed on a diagram in Fig 2.9. The radius of curvature of the effective mirror is $R = \frac{b^2}{a}$, and the focal distance as f=$\frac{R}{2}$. The interfocal and intervertex distances were known from the schematic diagram. These gave a, c and $b^2 = c^2 - a^2$. A value of -0.6353 m was obtained for the effective focal distance. The negative sign is due to the focus being virtual, as the hyperbolic secondary is divergent in nature.

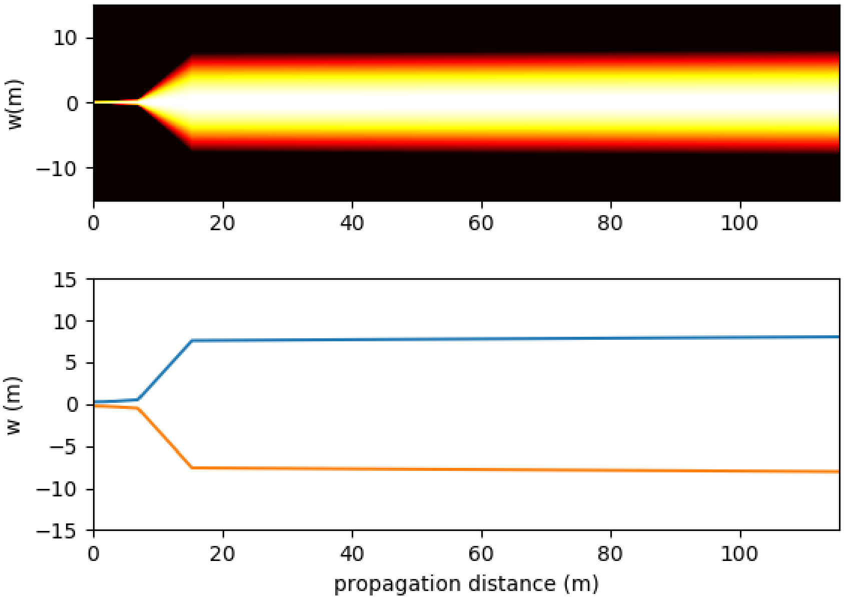

FIGURE 2.10: Gaussian propagation through two lenses representing the optics of the Pickmere telescope.

The R and w for the beam were found for various propagation distances through the telescope, and $w(z)$ is plotted for those points in Fig. 2.10. This plot uses a logarithmic scaling to better show the edges of the beam on the heatmap. The secondary and primary mirrors lie at $z = 15.34$ m and $z = 6.94$ m, respectively.

Fig 2.10 shows a flat phase Gaussian beam emanating from the telescope. This is ideal, as a telescope tends to look at objects which are at effectively infinite optical distance. Therefore, it must focus light with a flat phase front, which by the reciprocity theorem is equivalent to conversion of a source at the focus to a flat phase output beam. The lower plot in Fig. 2.10 shows the Gaussian beam width, w, the diameter outside which the intensity falls to I_0/e^2, where I_0 represents the boresight intensity. I_0/e^2 is a width parameter which can be substituted for FWHM when greater beam inclusion is desired.

2.3.3 Comparing PO with Gaussian beam modes

The most basic case of a beam propagating in free space, with no other optical components, is defined in Gaussian beam mode analysis using the starting waist radius w_0. In GRASP far field optics, it is defined in terms of beam taper (power relative to that on-axis) at a given angle, the taper angle. The equation to relate the waist radius to the far-field angle subtended by $w(z)$ (where the taper corresponding to $1/e^2$ is -8.7 dB) is given below as Eqn. 2.11, in degrees and in radians, as shown by Al Azzawi (2007).

$$\theta_{rad} = \frac{\lambda}{w_0 \pi} \qquad \theta_{deg} = \frac{180\lambda}{w_0 \pi^2} \tag{2.11}$$

To predict what linear beam radius should be observed at a given distance of propagation, basic trigonometry suffices on a beam which is assumed to be in the farfield; thus $r = z\sin(\theta)$. This calculation was performed for several values of z and w_0. The GRASP Gaussian beam was then set to model a near field source instead of a far field source. Near field sources are defined in GRASP in terms of their initial waist and radius of curvature, as opposed to the far field taper and taper angle. Radius of curvature 0 is included as a special case to yield infinite curvature radius, or a flat phase beam. When the near and far field sources were compared, the results of both analyses matched to within <0.1%, as shown below.

w_0=1 m, z=20 m.

Near field beam width=1.04951 m

Far field beam width= 1.0488 m

Difference =0.06%

The GRASP results for free-space propagation were then compared with the ideal paraxial Gaussian beams as modelled using Python. This was done by propagating Gaussian beams with waist radii of different sizes out to a fixed plane in space, 100 m from the waist location. Narrower waists suffer more diffraction and a wider beam at 100 m, while wider waists give a narrower beam. The GRASP results agreed very well with the Python Gaussian beam mode simulation - to an accuracy of $< 0.2\%$ for all tested values of w_0. These tiny deviations are easily accounted for by the different resolutions employed by the two routines; Gaussian beam modes in Python and PO/PTD analysis in the GRASP environment.

A comparison of the beam radius predicted by PO and the Gaussian beam mode model of the two-mirror Pickmere telescope was also made, starting

TABLE 2.1: A comparison of beam radius calculated using Gaussian beam modes (GBM) and GRASP PO.

waist radius	GRASP radius (m) at 100 m	GBM radius (m) at 100 m	percentage difference
25 cm	6.3603	6.3712	0.17
50 cm	3.2192	3.2222	0.093
75 cm	2.2504	2.2507	0.013
100 cm	1.87926	1.87963	0.02

with the same Gaussian beam at the telescope focus and propagating 50 m from the primary mirror. Gaussian beam modes gave a width of 7.729 m, while GRASP gave 7.800 m. Thus, the discrepancy between the routines was below 1%.

2.4 Mirror blockage

Once the two programs were found to agree, the GRASP model was investigated in more detail. The models are sequential, so that the beam first intercepts the secondary mirror, then it propagates back to the primary mirror, and after reflecting a second time, it propagates out to free space, past the secondary. No dark region was observed behind the secondary, which is unphysical, as one would expect a shadow zone directly behind the mirror where the light from the primary could not reach. This zone would have a roughly conical shape and depend on the ratio of the secondary diameter and the wavelength of the light. To model this, a copy of the secondary mirror was instantiated in the same spatial position as the original so the beam propagated from the focus to the secondary and from the secondary to the primary and then to the secondary again as it exited the telescope. When this change was implemented, it was observed that considerable radiation was back-propagating from the secondary, before passing directly through the primary, creating a bright region behind it. This is logical, as if the secondary is instantiated for a second pass, to model diffraction effects on the beam, it will reflect light back along the optical axis. This light then propagates unobstructed into space behind the primary, as this reflector has not been instantiated for a second pass.

As more simulations were run, it became evident that there would always be a final surface which was not instantiated for the final pass of the light.

Thus, to approximate the true system to considerable accuracy, one would have to pass the beam many times between the two reflectors. This would result in an asymptotically increasing accuracy, as more light hit the grid with each reflection. Computing time, however, increases rapidly with the number of passes, as the wave patterns become more distorted and thus more difficult for the PO/PTD to calculate. For this reason, taking too many passes was impractical.

To investigate this, two separate GRASP images were taken, one with a single reflection off the secondary and primary, and the other with a final additional reflection off the secondary. In Fig. 2.11, the shadow of the secondary is clearly defined. Additionally, the lobes of the power pattern of radiation propagating back from the secondary can be seen. In Fig. 2.12, the reverse is observed; the primary is perfectly defined, and the secondary shadow is not present. Instead, there is a higher intensity region propagating out to infinity along the optical axis.

The GRASP technical description (TICRA, 2013) discusses the modelling of subreflector blockage in dual reflector systems such as this. In their example they deliberately exaggerate the telescope design (small main reflector and relatively high edge taper from the feed at the subreflector) to make the effects of subreflector blockage and feed spillover easy to perceive. It suggests two ways of modelling the blockage. In the first, the part of the primary that is blocked by the secondary (subreflector) is removed i.e. replaced by a hole, so the currents produced in this area do not contribute to the field. The second method suggested is more rigorous and calculates the currents on the secondary that are generated from the illumination by the primary mirror. The field from these currents are then added to the output field and can make a significant contribution to the sidelobe level.

As discussed above, the currents induced on the secondary will illuminate the primary mirror once more and generate a second set of induced currents which, like the first set, will radiate in the far-field and be blocked by the subreflector. This process will continue in an ever-decaying fashion until the remaining contribution due to further scattering become negligible. For the example in the GRASP manual, five iterations were required before a stable result was obtained. If an accurate sidelobe pattern for Pickmere were required, then a similar process should be carried out.

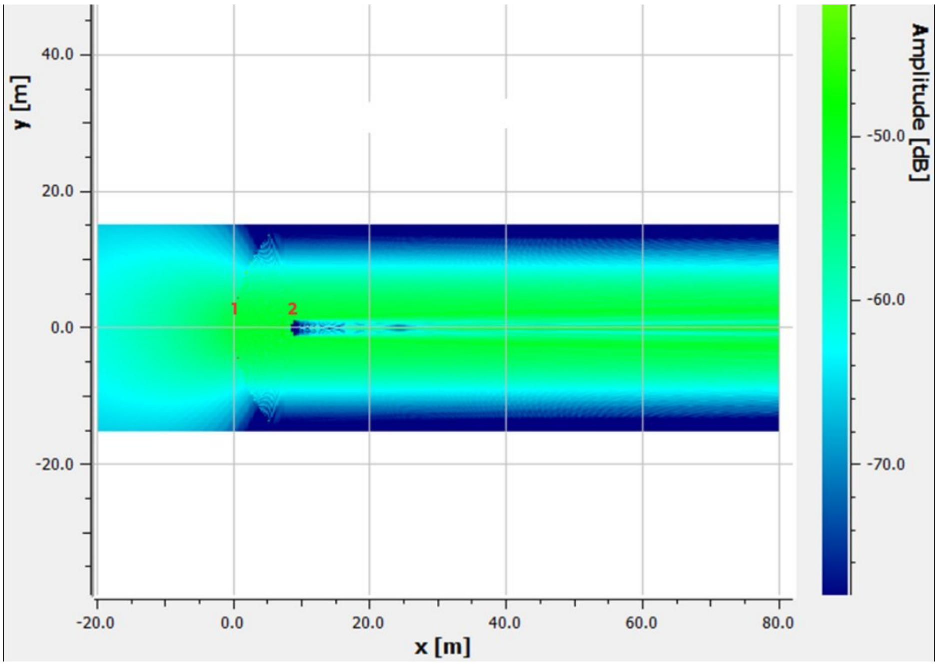

FIGURE 2.11: Beam propagation with surface of last scattering as secondary. The primary and secondary are marked 1 and 2, respectively. The x axis of the cut corresponds to the propagation axis

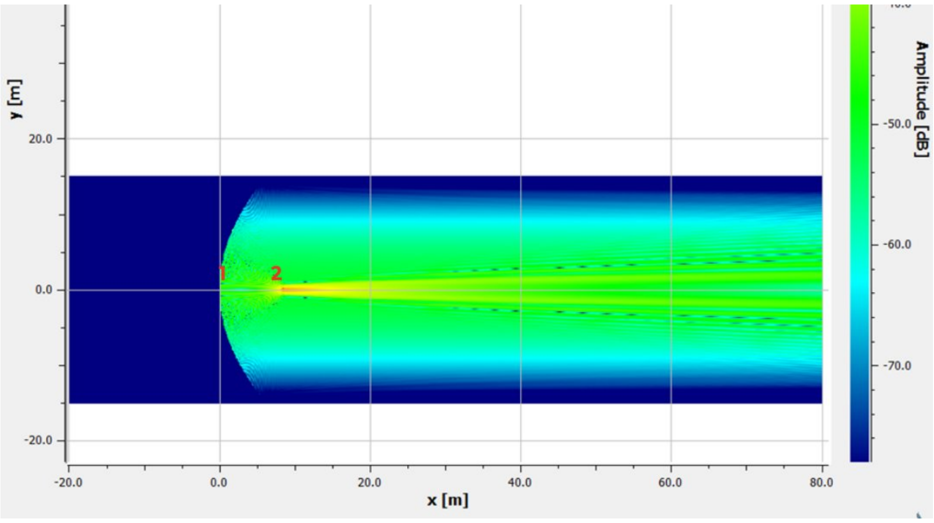

FIGURE 2.12: Beam propagation with surface of last scattering as primary. The primary and secondary are marked 1 and 2, respectively. The x axis of the cut corresponds to the propagation axis

2.5 Summary

The purpose of the work outlined in this chapter was to model the optical properties of the Pickmere telescope, a Cassegrain radio telescope operating in the low GHz band. The analysis was carried out using the TICRA GRASP integrated PO package. The component parts of Pickmere were introduced into the simulation using data from the design schematics of the telescope. A number of data collection elements were placed into the simulation to return intensity plots as both cuts and grids. The radiation was viewed on the axis of the telescope, showing the focussing effect of the primary and secondary surfaces. This gives confidence that the telescope parameters were calculated correctly from old documents.

The representation of the system yielded by GRASP was somewhat incomplete, as to account for all of the scattered radiation, the program would have to make a very large number of passes between the surfaces. To simulate this would require excessive computational effort, as the system complexity increases rapidly with the number of reflections of the radiation. The difference caused by modelling one more internal reflection was investigated.

As a comparison, a more approximate model of the telescope was developed using Gaussian beam mode optics with ABCD matrices. This was shown to be quick to execute, and provided congruent estimates of beam radii when compared to GRASP. Both models gave a flat phase beam on the sky when radiation was input at the focus and propagated through the system.

The optical model of the Pickmere telescope will prove useful to our collaborators in Manchester University, as they develop focal plane phased arrays. The remainder of this thesis will look at work on feeds used in two other telescopes, QUBIC and ALMA, which are described in the next chapter. Fields from these can be propagated through their respective instruments in a manner similar to that described here for Pickmere.

Chapter 3

QUBIC and ALMA

3.1 Introduction

In this chapter, I will describe two telescopes, QUBIC and ALMA. Both operate primarily at mid GHz frequencies, and make use of corrugated horn antennas. The analysis of horns developed for these projects represents the majority of the work presented in this thesis, and will be explained in detail throughout the subsequent three chapters. This chapter, however, will focus on the background to the telescopes. A description will be provided of the general optical design of the telescopes and the sources that they can be used to investigate. Finally, the observing goals for the telescopes, each at the forefront of modern microwave astrophysics, will be briefly outlined.

3.2 QUBIC

3.2.1 Origins of the cosmic microwave background

The cosmic microwave background (CMB) is one of the most interesting and consequential astrophysical sources on the millimetre wave-THz boundary. It is an ever present sea of near uniform radiation at first seemingly without directionality or structure. The radiation originates from the surface of last scattering, the point at which the Universe cooled sufficiently to allow light to travel. Before this, the early Universe contained protons and free electrons in a sea of photons. Light cannot travel substantial distances in a medium containing many unbound electrons, as it is constantly absorbed and scattered, making the medium opaque. A proton and an electron can combine to make a hydrogen atom, a process known as recombination. However, the atom is likely to be reionised by absorbing a photon, if the energy of this photon exceeds the binding energy of their mutual electrical potential, denoted ionisation energy. This is 13.598 eV in the case of monoprotic hydrogen. Once the temperature drops sufficiently that such photon collisions are rare, light can propagate almost infinitely in the rarefied neutral gas.

By Wien's law, as discussed in the previous chapter, the temperature at which photons of energy 13.598 eV are the most prevalent is approximately 5.6×10^4 K. However, this simplistic calculation must be adjusted for the dominance of photons over baryons in the early universe. If many more photons than baryons are present, each baryonic particle is very likely to remain ionised well into the tail of the thermal distribution of the photon gas surrounding it. This corresponds to a lower temperature at recombination for a Universe with an elevated photon to baryon ratio. The actual ratio is approximately $1 : 2 \times 10^9$ as quoted by Liddle and Loveday (2008). When this is taken into account, the temperature at which recombination occurs proper (defined as $N(H^0) = N(H^+) = 0.5N_{total}$) is approximately 3000 K. From cosmological modelling, this is estimated to have occurred about 380,000 years after the Big Bang. The photon flux from a 3000 K blackbody would have peaked in the near infra-red, but as the Universe expanded, the radiation was redshifted, and the blackbody spectrum shifted to longer wavelengths. The current estimated redshift of the CMB surface of last scattering is approximately 1100, so dividing 3000 K by this figure, we arrive at the current blackbody temperature of the CMB, 2.7 K.

By looking at the tiny variations in this radiative field, we can piece together a picture of the Universe in its infancy, long before matter condensed to form the structures we see today. These variances are broadly divided into temperature and polarization anisotropies. Observation of these requires subtraction of a dipole fluctuation ($\frac{\Delta T}{T} = 10^{-3}$) due to the Earth's peculiar velocity with respect to the distant universe. At ($\frac{\Delta T}{T} = 10^{-5}$), temperature anisotropies are seen, while polarization anisotropies require sensitivity at least an order of magnitude greater to discern. Performing these immensely accurate observations over vast areas of the sky is technologically very challenging, and has been at the forefront of cosmological experimental advancement for decades.

3.2.2 Polarization Anisotropies

In astronomy, the polarization of electromagnetic radiation is typically represented by Stokes parameters which are defined by a set of parametric equations in spherical coordinates; a thorough mathematical derivation of these is provided by Collett (2005). The parameters are often assimilated as a four-element column vector, the Stokes vector $\bar{S} = \begin{bmatrix} I \\ Q \\ U \\ V \end{bmatrix}$. The I parameter represents the intensity of the radiation, while Q represents the preponderance of horizontal over vertical linear polarization and U represents the preponderance of $+45^\circ$ over -45° linear polarization. The final parameter concerns circularly polarised radiation, and can be neglected in this case, as it is not an inherent polarisation of the CMB, and will thus have a value of zero. For Q and U, values between positive and negative unity are permitted, with the magnitude of the parameters quantifying the relative strength of polarisation, and their signs determining orientation. The Stokes parameters often correspond to how polarization is measured (hence the Q and U in QUBIC) but because they are coordinate-dependent are less convenient for describing the polarization anisotropies of the CMB. For this a decomposition into E amd B modes (derived from the combinations $Q \pm iU$) is used. E modes are curl-free, possessing a finite gradient and zero curl. B modes are polarized at 45 degrees to the principal axes and have finite curl and zero gradient. This is shown in Fig. 3.1. This decomposition is also physically useful because the origins of E mode and B mode anisotropies in the CMB are different.

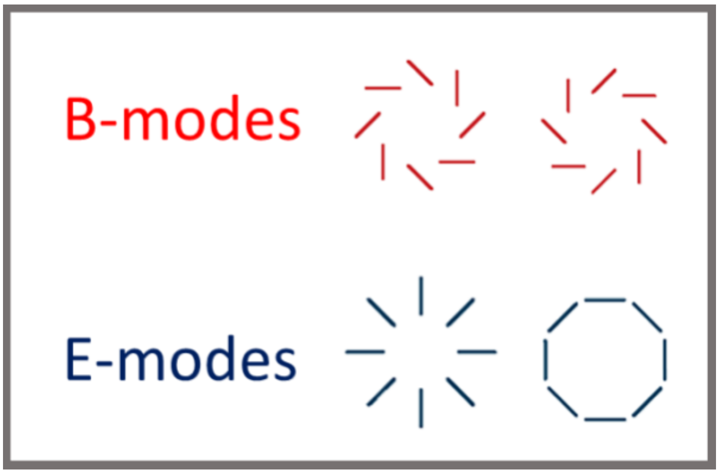

FIGURE 3.1: E and B mode polarization components (APS/Michael Schirber, taken from https://physics.aps.org/articles/v13/164).

Both types of polarization anisotropies represent a tiny fraction of the incident radiation from the CMB. Of the two, E modes are dominant and were primarily generated by scalar density perturbations in the early Universe. B modes are extremely weak, on the order of 10 μK, and can be generated as the result of conversion of E modes to B modes during their 13 billion year journey toward Earth. This conversion is initiated by the passage of the radiation through strong gravitational fields over long periods of time. This gravitational lensing effect may be caused by galaxy clusters, and also the dark matter halos which surround galactic structures, contributing substantially to their gravitational influence (Fidler, 2014). The first statistically confirmed observation of these lensed B modes was made by the POLARBEAR collaboration, detecting the modes to a significance of 4.7σ (Ade et al. 2014).

It has been predicted that B modes are also generated by gravitational interactions in the early universe. Primordial gravitational waves, a signature of the inflation of space, could have imprinted evidence of their existence onto the nascent CMB at the surface of last scattering, a time when these gravitational waves were of sufficient magnitude to have detectable effects. These relic perturbations are termed primordial B modes. To date, despite its popularity as a theory, the primary evidence for inflationary cosmology is solely circumstantial, in that it can explain many otherwise difficult to explain cosmological observations. As such, the detection of these gravitational wave signatures in the CMB would lend strong and much-needed experimental evidence to inflation, the smoking gun for the violent birth of the Universe. One notable claim was made to their purported discovery by (Ade et al. 2014). This work appeared to represent confirmation of primordial B-modes, but upon review, the signal could not be differentiated from that caused by galactic dust lensing. The graphic showing B-mode "twists" in the CMB signal is included as Fig. 3.2.

3.2.3 QUBIC technical overview

The Q and U Bolometer Interferometer for Cosmology, QUBIC, is a ground-based array which primarily aims to detect the primordial B modes discussed earlier. It is a cryogenic instrument, encased in a large pulse tube cooled cryostat with optics cooled to 4 K. This reduces the effects of thermal and electrical noise on the instrumentation. The observing window is a 40 cm sheet of high density plastic, which, as a good electrical insulator with few free charge carriers, is optimally transparent to radiation at the observing frequencies. After entering the cryogenic environment, incident radiation then passes through a rotating half-wave plate (HWP) and a polarizer. This beam is received by a 20×20 array of back-to-back corrugated horns. The light is then reradiated

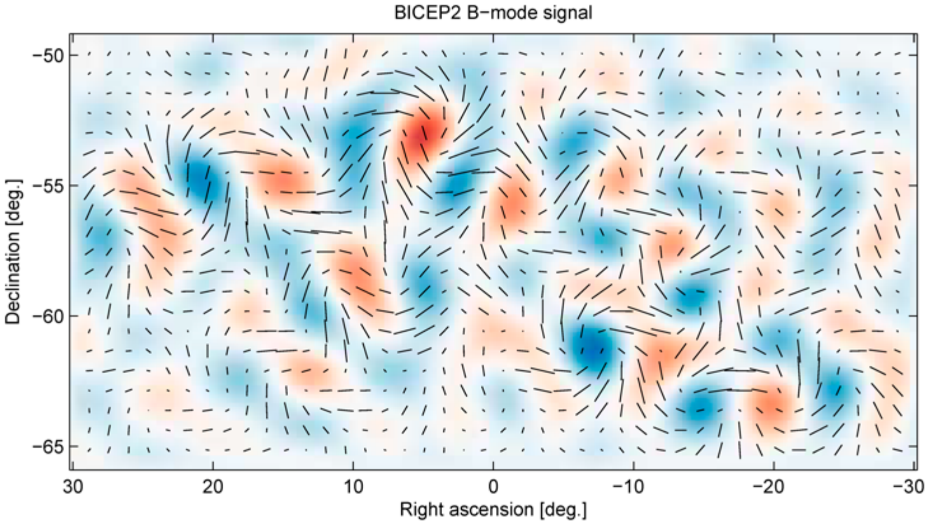

FIGURE 3.2: B mode signal, initially thought to be primordial in nature, captured by the BICEP2 instrument (Ade et al. 2014a).

into an optical beam combiner (two off axis mirrors) and the 400 beams are combined on a focal plane. The focal plane is tiled with the detectors: four sub arrays of 248 pixels apiece, cooled further to 300 mK. The QUBIC array is designed to trasmit radiation in two observing bands, centred at 150 GHz and 220 GHz. A basic schematic of the optical components is shown in Fig. 3.3

The QUBIC apparatus uses a novel combination of two established physical techniques, interferometry and bolometry. By combining the advantages of these two techniques, the instrument strives to achieve the immense sensitivity and signal purity required to separate the ultra faint B mode signal from the much stronger background and foreground noise. One of the primary advantages of interferometry is its low systematic errors, while bolometry results in superior sensitivity over other techniques.

Interferometry concerns the combination of wave based information from multiple sources. In astrophysics, it is typically used as a workaround to the restrictive limitations on angular resolution placed by the Rayleigh criterion

$$\theta = 1.22\frac{\lambda}{D} \tag{3.1}$$

on observations, particularly at longer wavelengths. An interferometric aperture system may be considered to have a baseline D equivalent to the separation of the centres of the individual interfering apertures, as discussed in the introductory section concerning VLBI. In the case of QUBIC, it allows the 400

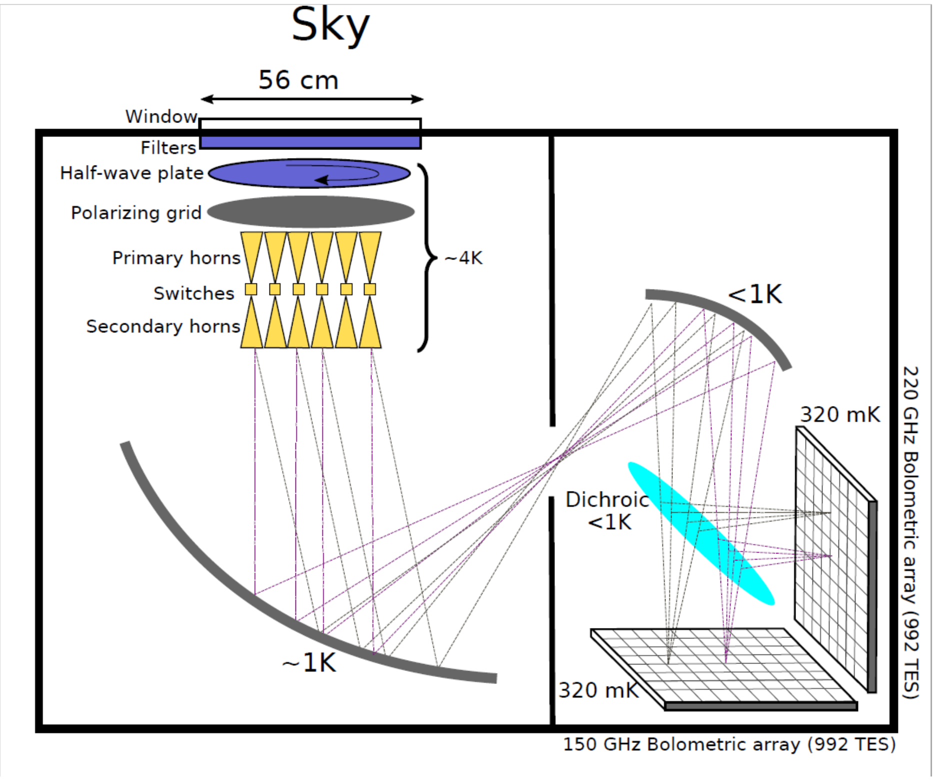

FIGURE 3.3: Cutaway schematic diagram of the QUBIC apparatus (May et al. 2014.)

horns to behave as a single large detector, with an aperture of 40 cm. This corresponds to 120 λ at 90 GHz, and therefore a physical resolving limit of 0.01 rad $\approx$ 0.5 degrees. or the apparent size of the solar/lunar disc in the night sky. In the case of QUBIC, interferometry is not used for its ability to create an equivalent large aperture, but rather to exploit its control of systemic errors in calibration. By opening and closing switches between the horns in a back-to-back pair, equivalent baselines can be selected, which should, if calibrated correctly, produce identical patterns on the focal plane. The rotating HWP and polarizer modulate the pattern on the focal plane, and this, along with a knowledge of the corrugated horn beam pattern, allows recovery of an image on the sky in terms of Q and U Stokes parameters (Burke, D. 2021).

Bolometry constitutes the irradiation of a resistor with known thermal inertia with the intention of measuring the total spectral power of the incident radiation. It differs from other detection methods in that it is sensitive to all frequencies, and exhibits a linear response across the spectrum. In the case of QUBIC, filters and the horn waveguides are used to define the frequency bands which reach the bolometer and are absorbed. Additionally, the enclosed cryogenic system minimizes input from the environment. The bolometers used are transition edge sensors (TES), ultra cold superconducting detectors. The name refers to the edge of the transition between typical and super conductivity, which occurs at a specific temperature, usually in the 0-10 K range. These sensors can thus use the high temperature dependence of their resistance at the edge of the superconducting state to very accurately detect the power absorbed from the incident photon flux (Bennett, D 2014). Fig. 3.4 shows the structure of a TES pixel. Such detectors can register the change in energy resulting from the absorption of even a single photon.

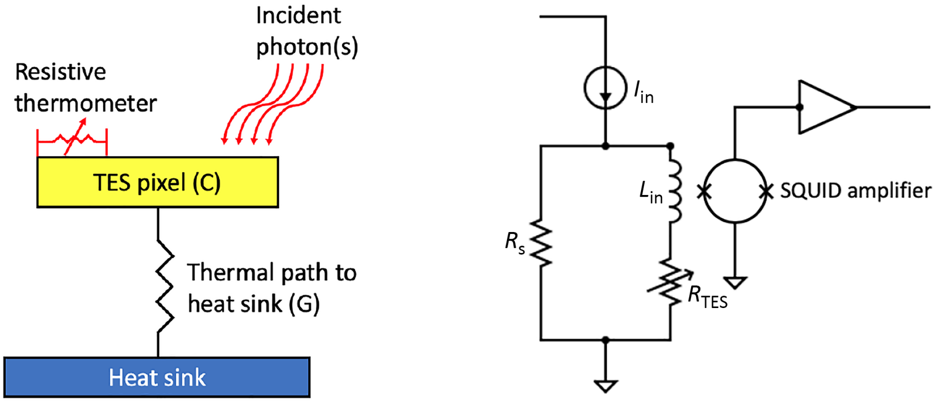

(a) (b)

FIGURE 3.4: Schematic diagrams of the functionality of an individual TES bolometric pixel, with its associated amplifier (Nagler, Sadleir and Wollack, 2021).

The signals from the TES pixels are then multiplexed and amplified by superconducting quantum interference devices (SQUIDs). These devices detect tiny changes in magnetic field strength by measuring the variation in a current around a loop of superconducting wire. Superconducting wire is chosen due to the expulsion of magnetic flux from the inside of the wire, and thus its total lack of electrical resistance. The outputs of the individual SQUIDs are combined to generate the total interference pattern output for the array, representing the signal on the sky convolved with the interferometer beam pattern. This detection system takes advantage of the cryogenic environment already required for a good signal-to-noise ratio, and boosts it further to maintain a superconductive state in the TES. A further detailed technical outline of QUBIC is given by Hamilton et al. (2021).

Knowledge of the beam patterns from the QUBIC corrugated horn array is important for the success of the project. In Chapter 6 I extend the modelling capability of Maynooth's in-house software 'PyScatter' to take account of manufacturing tolerances on the horn array. In Chapter 4 I investigate the possibility of re-designing the QUBIC horns to also operate at 90 GHz.

3.3 ALMA

3.3.1 Technical overview

The Atacama Large Millimetre Array (ALMA) resulted from a collaborative effort by European, North American and Japanese astronomical organizations, all seeking an array of linked ground based telescopes to operate in the millimetre wave spectral band. The location selected for the array lies on a large raised plain, deep in the Atacama Desert of Chile. This area was chosen for its altitude of over 5,000 metres, its stable, dry climate, and its considerable separation from substantially populated areas and the ensuing radio noise. These factors result in a highly stable and rarefied column density, combined with a lack of absorption and scattering from dust and water vapour; as such this area boasts some of the most reliably superior astronomical seeing from ground level anywhere on the globe (Bustos, 2014).

FIGURE 3.5: ALMA array in extended configuration (artist's impression, Britannica 2018).

The array consists of 66 telescopes, most of which are 12 m in diameter, with some 7 m in diameter. The array can form many unique configurations, enabling a massive variety of baseline lengths and spatial orientations. 192 telescope slabs lie in a radial pattern extending from the centre of the site.

Connecting roads allow two purpose built crawlers to move the telescopes between the slabs, changing the array shape. This allows for a resolution below one hundredth of an arcsecond when the array is in its widest configuration, while also permitting compact patterns to examine extended sources. In general, wide configurations are used for angular resolution limited observation, such as with the EHT, as mentioned earlier. Close configurations are conversely used for photometric intensity limited observations, typically faint objects subtending large angular scales, such as nebulae. Fig. 3.5 shows an artist's rendition of the final ALMA array moving to the extended configuration.

The individual ALMA component telescopes have a Cassegrain design, with the majority having a 12 m primary and a 0.75 m secondary suspended on struts. Tolerance on the surface of the dishes is 20-25 μm, similar to coarse copy paper. This is sufficient for the minimum wavelength of radiation received, approx 350 μm, being below 0.1λ. Rigidity is a more restrictive concern, with a tolerance of just 13 fs of delay over a 5-minute period, corresponding to a maximal flexion tolerance of 3.9 μm in the dish. The telescopes must thus be sufficiently rugged to withstand the harsh environment, including high winds, 40 degree diurnal temperature shifts, and frequent earthquakes, without suffering even minor deformation. Additionally, they must be robust enough to be moved between sites without loss of performance due to distortion under their own 100 ton weight (ALMA, 2021).

At the heart of ALMA is the correlator, one of the most powerful supercomputers in the world, housed in the highest altitude facility of its kind. Whereas a basic interferometer has just two elements, the correlator allows ALMA to include 64 antennas, giving up to 2000 baseline lengths between the pad installations, in addition to countless radial orientations. Accomplishing this task in real time, with more information constantly streaming in, is a mammoth computing task. To this end, the four quadrants of the correlator use over 100 million individual processors to parallelise and complete tasks at a rate of 1.7×10^{16} operations per second.

TABLE 3.1: Spectral observing bands of the ALMA array (Iguchi et al. 2009).

Band	Frequency range (GHz)	Type
1	31–45	SSB
2	67–90	SSB
3	84–116	2SB
4	125–163	2SB
5	163–211	2SB
6	211–275	2SB
7	275–373	2SB
8	385–500	2SB
9	602–720	DSB
10	787–950	DSB

3.3.2 Observational bands

The ALMA functional range covers 1.5 decades of frequency in the low GHz and THz regions of the electromagnetic spectrum. The frequency band structure is shown as Tab. 3.1, however the exact boundaries vary slightly depending on the source quoted. The individual bands each have a fractional bandwidth of 0.25-0.3, making them suitable for use with a single detector. A wide-band detector could also combine two adjacent bands, as will be discussed later. Bands 3 through 10 are fully active, with Band 1 also being implemented in late 2021. Band 2 is still under development. In Chapter 5 I investigate horn designs to facilitate possible combined band detectors in the future.

3.3.3 ALMA science

With each new band, new atomic and molecular transition lines are opened up to science, at interferometry-aided resolutions that were not possible with simple single dish designs. These allow for the detection of biomolecules in various settings, from the clouds of gas giants in the Solar System to the interior of giant molecular clouds. Many of the regions observed by ALMA are totally opaque in the visible due to vapour and dust. Of particular interest are Bands 4-5; various carbon-based molecular transitions have been detected in the Band 4 region of the spectrum. Furthermore, water vapour has a faint transition in the Band 5 range, allowing its detection in protostellar disks and molecular clouds. These capabilities hold particular interest due to the status of water and carbon as the most fundamental prerequisites for the development of recognisable life (ESO, 2021). The dust penetrating power of radiation at ALMA frequencies also allows imaging of the internal structure of nascent stellar systems. This is important as in the initial planet forming era, such systems are without substantial stellar winds, their parent star having only recently initiated core fusion. As such, the larger planetary bodies are still sheathed in their formative cloud, and thus are not detectable by visible-light instrumentation. As ALMA grows, it can begin to search for signature density structures within these systems, potentially showing the sweeping voids in protostellar disks thought to be indicative of planet formation.

3.4 Summary

The purpose of this chapter is to serve as a supplementary reference for Chapters 4, 5 and 6, explaining the QUBIC and ALMA projects, upon which those chapters are based. The design, operation and objectives of the observing projects were discussed, along with possible outcomes and future development. This provides context to the corrugated horn design and simulation which forms the bulk of this thesis.

Chapter 4

Corrugated horn design and modelling

4.1 Introduction to corrugated horns

This section concerns the use of waveguides and corrugated horns for the transmission of radiation at GHz and THz frequencies. A waveguide is a hollow channel of conducting material, filled with a dielectric, commonly air. It acts to transmit microwave energy, without significant losses, by total internal reflection between the internal walls. Analogues for other parts of the EM spectrum include fiber optics for visible light and coaxial cables for RF.

A waveguide allows the propagation of radiation in a series of distinct forms called modes. Each mode is a specific solution of the wave equation associated with the vibrational cavity formed by the waveguide. Specifically, the waveguide imposes a boundary condition, converting the wave into a mode by requiring that the field at the conductive boundary be reduced to zero. Each mode has a characteristic frequency range throughout which it will propagate. The modes of smooth-walled waveguides, known as TE and TM modes, will be described in detail in Chapter 6. The limiting frequencies beyond which a particular mode will not propagate are termed cutoffs. The mode with the lowest cutoff is the waveguide cutoff, as below this no radiation propagates. There are separate solutions for the modes propagating in the conducting "cladding" and for those propagating in the dielectric "core" (Snitzer, 1961), but the latter is of primary interest.

Waveguides come in a variety of geometries, tailored to their specific purpose. A long cylindrical waveguide can be used to transmit signals, whereas a horn, or flared waveguide, is generally used to radiate them. The fundamental requirement for a horn is that the geometry provides a smooth transition between the impedance of the transmission medium and the impedance of

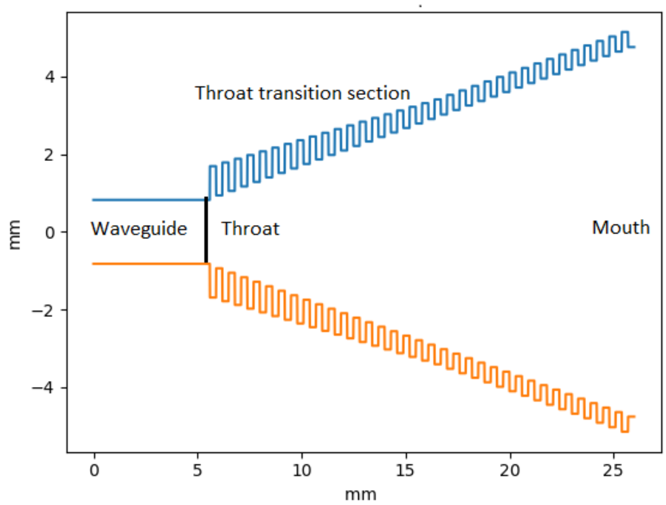

FIGURE 4.1: Horn cross section, showing the waveguide, throat and mouth sections of a horn. The transition section is also marked, where the corrugation depth reduces to 0.25 λ

free space. The mathematically ideal geometry for this is an exponential horn, as these provide the fewest possible reflections between source and aperture (Ascama et al. 2013), minimising reflective distortion and losses. In practice, simpler conical and square conical (pyramidal) horns are often used, due to ease of manufacture and modelling. Intermediary designs such as polynomial profiles may also be employed. A horn can be designed to perform multiple functions simultaneously, in addition to impedance matching. These include restricting the modes in which radiation can propagate, applying polarisation effects and increasing the directional gain of a signal. These functions are modulated by the specific geometry of the horn and highly dependent on the wavelength of incoming light. As such a particular horn is designed to operate over a relatively narrow waveband, typically in the region of ±20% centred on the quoted frequency of the horn (Del Torto, 2012). Fig. 4.1 shows a cross section of a horn design which will be discussed further in the next chapter. It is labelled to show the different regions of a typical design, the waveguide, throat and mouth.

Many horns used to propagate microwaves in astronomy and communications are corrugated, having crenellations or slots of a specific depth placed radially around the interior of the horn. This performs a number of functions. In addition to improving the directional gain, it allows for the propagation of hybrid modes within the cavity. These modes have both TE and TM components.

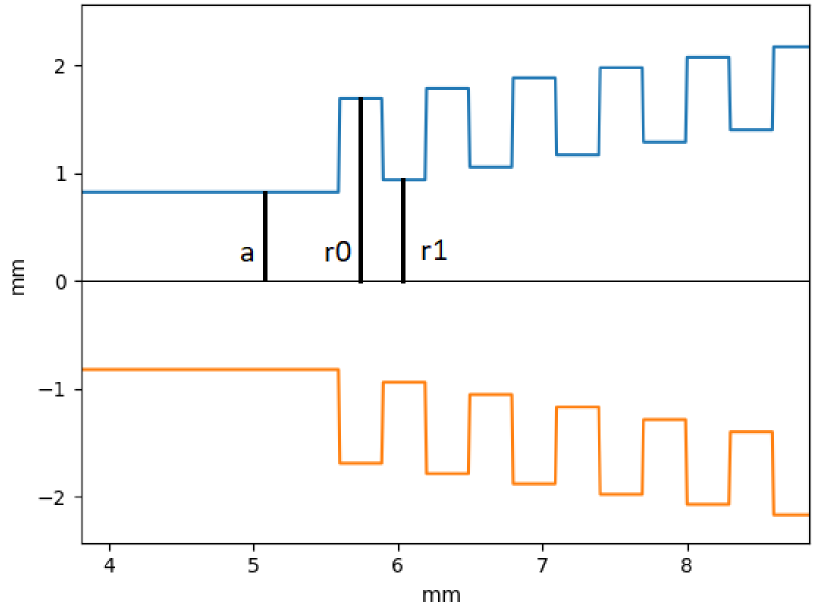

FIGURE 4.2: Closeup of the throat of a horn, showing r_0, the radial distance from the horn boresight to the bottom of a slot, and r_1, the distance to the corrugation peak. Also marked is a, the waveguide width.

The most commonly employed mode is the TEM11 mode, which typically approximates a Gaussian beam within the operational waveband (Granet and James, 2005). These hybrid modes allow corrugated horns to function with lower attenuation then their smooth-walled counterparts. Fig. 4.2 shows a close-up diagram of the throat section of a corrugated horn, defining some of the parameters used in the remainder of the thesis.

4.1.1 Glossary of further relevant terms

The performance of horn antennas will be discussed throughout the remainder of this thesis, here some common terms used to describe various aspects of performance are explained.

Aperture efficiency is the ratio of the effective area to the total area of an antenna. Effective area is the area from which EMR can radiate. Aperture efficiency may be reduced from unity by physical constraints such as armature and equipment partially blocking the optical cavity. It may also be reduced in the case of an aperture which is not designed to capture light across its entire surface, for example, a mesh gridded dish with a solid non-reflecting rim.

Insertion loss is the decrease in signal intensity caused by inserting a component into a transmission line. It may also be termed attenuation. This is typically calculated as the power leaving divided by the power entering, and expressed as a negative dB value (a positive value would signify gain or amplification). This quantity is usually minimised to optimise optical systems, particularly across passive components such as lenses, mirrors, etc.

Polarisation efficiency represents the degree to which the polarisation of the incoming radiation matches the polarisation of the antenna detecting it. In the case of a linear polariser it may be calculated as the square cosine of the angle between the polarisation direction of the antenna with respect to that of the incoming radiation. Thus, for an angle of $\pi/2$, the efficiency will be zero, perfect obstruction, and for an angle of zero, the efficiency will be unity, perfect transmission (Mandeep and Hilary, 2011).

Reflection loss is a reduction in power due to the reflection of electromagnetic energy off a sharp boundary between media of differing impedance. For example, horns are used to minimise the reflection of power back down a transmission line due to the impedance mismatch between the transmission line and free space. It may also be referred to as return loss. It is usually quoted as the ratio of the transmitted power to the returning power and is typically expressed in dB. Thus, a minimal return loss is preferable, as it implies that the component impedances are well matched.

Scattering parameters are a method of analysing the interaction between ports in an electrical system. The scattering parameters of a system of N ports may be represented as an $N \times N$ matrix, wherein each term refers to an interaction (transmission or reflection) between the associated two ports. In particular, the S11 parameter can be used to express the return/reflection loss of an antenna, as defined above.

Evanescent modes and fields are a feature integral to wavelike phenomena. Continuity is the cornerstone of wave mechanics, thus waves tend not be discontinuous at a boundary. For example, the continuity of matter waves at the boundary of a quantum potential well results in the finite probability of tunnelling through the well boundary. In the case of electromagnetic waves, this is observed as exponentially decaying fields penetrating into a cavity which is too small to support transmission of the associated mode. Such fields are also observed upon exceeding the critical angle at an optical refractive boundary.

These fields do not transmit power, their Poynting vectors averaged over a cycle sum to zero (Ramakrishna and Armour, 2003), however they can interfere with desirable modes, as such measures are often taken to ensure that they do not affect the performance of components.

4.1.2 Modelling corrugated horns with PyScatter

Whilst there are rules-of-thumb for the design of corrugated waveguides and horn antennas, a rigorous analysis requires a technique such as finite-element analysis (using for example Ansys HFSS[1]), or electromagnetic mode-matching (Clarricoats, 1984). In this thesis I have made extensive use of the in-house software PyScatter (Gradziel, 2007) (Kalinauskaite, 2018) that uses electromagnetic mode-matching. This technique regards the corrugated structure as a sequence of smooth walled cylindrical waveguide sections, each of which can support a set of propagating TE and TM modes. At each corrugation the sudden change in the radius results in a scattering of power into backward propagating reflected modes in the left-hand side guide segment and forward propagating transmitted modes in the right-hand segment. The power coupling between modes is given by the overlap integral

$$\int e_{n,l} h^*_{m,r} dA \tag{4.1}$$

where $e_{n,l}$ is the transverse electric field of mode n on the left-hand side of the junction, $h_{m,r}$ is the magnetic field of mode m on the right-hand side of the junction and dA is a surface element on the transverse plane. The modes are then propagated through the length of waveguide section to the next scattering junction where the overlap integral between the modal components is performed again.

If [A] and [C] are column vectors of the mode coefficients of the fields incident from the left and the right, and [B] and [D] are the mode coefficients of the resulting reflected fields (Fig. 4.3), then their relationship is described using a scattering matrix [S]

$$\begin{bmatrix} [\mathbf{B}] \\ [\mathbf{D}] \end{bmatrix} = [\mathbf{S}] \begin{bmatrix} [\mathbf{A}] \\ [\mathbf{C}] \end{bmatrix} = [\mathbf{S}] \begin{bmatrix} [\mathbf{S_{11}}] & [\mathbf{S_{12}}] \\ [\mathbf{S_{21}}] & [\mathbf{S_{12}}] \end{bmatrix} \begin{bmatrix} [\mathbf{A}] \\ [\mathbf{C}] \end{bmatrix} \tag{4.2}$$

---

[1] https://www.ansys.com/products/electronics/ansys-hfss

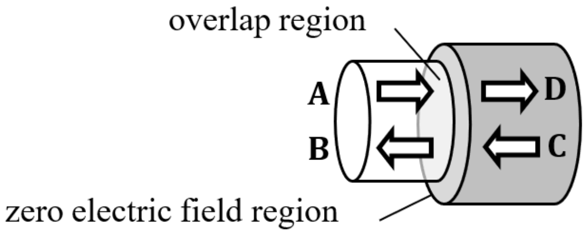

FIGURE 4.3: Scattering at a horn corrugation.

whose elements are calculated using overlap integrals as described in (Olver, 1994). These overlap integrals are the subject of Chapter 6 and will be discussed further then. The columns of the scattering matrix describe the amplitude of each output mode generated by a unit-amplitude input mode. The scattering matrix for the horn as a whole is computed by cascading the matrices for each uniform section and junction. The field at a corrugation step in a corrugated horn is determined from Eq. 4.2. The components approaching the junction, A and C are related to the components leaving the junction B and D, through multiplication by the S matrix. The transmitted and reflected power are found by multiplying the complex elements of the relevant column vector by their complex conjugate and summing them.

The PyScatter code takes as input a text file, known as the geometry file, that specifies the operating frequency and corrugation geometry of the horn. An example is shown in 4.4. The frequency and the number of corrugation sections are given in the header, followed by a list of all the section lengths, followed by the section radii (r_o and r_1).

Fig. 4.5 shows a typical plot of the beam pattern from a corrugated horn calculated using PyScatter. This particular example is for the corrugated horn used in the QUBIC telescope. It was computed by calculating the coupling between 30 TE and 30 TM modes at 173 GHz (the central design frequency of this horn was 150 GHz). The plot shows many of the advantages of corrugated horns and why they are used extensively at GHz frequencies. The beam is directional (the gain on the main lobe is greater than 20 dB and the sidelobe level is low) and highly symmetric as can be seen by comparing the 0, 45 and 90 degree cuts. The cross-polarisation is low, falling below -50 dB at boresight, and peaking at -36dB near the first nulls.

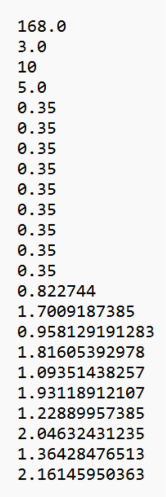

```
168.0
3.0
10
5.0
0.35
0.35
0.35
0.35
0.35
0.35
0.35
0.35
0.35
0.822744
1.7009187385
0.958129191283
1.81605392978
1.09351438257
1.93118912107
1.22889957385
2.04632431235
1.36428476513
2.16145950363
```

FIGURE 4.4: Example geometry file input to PyScatter. The first three lines are the header (the pattern is calculated at 168 GHz, line 2 is not used, and there are ten sections in the horn), the following ten lines are the section lengths and the final ten lines are the section widths.

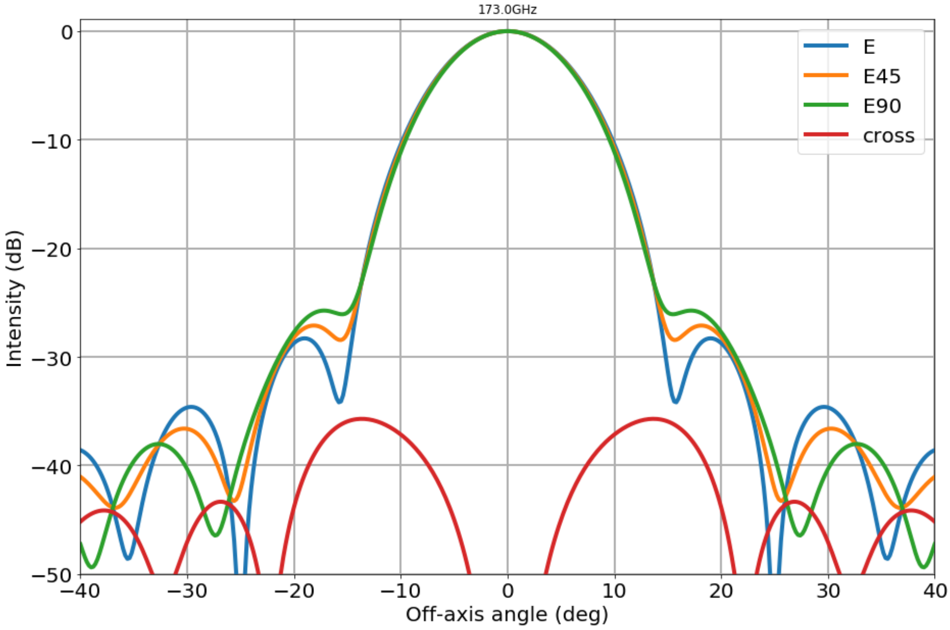

FIGURE 4.5: Sample pattern plot of transmitted power as a function of angle for a corrugated horn. This example shows the 173-GHz beam pattern of a QUBIC horn.

4.2 The QUBIC horn design

4.2.1 QUBIC at 90 GHz

The QUBIC instrument (see Chapter 3) uses an array of back-to-back corrugated horns to collect electromagnetic radiation from the sky and transmit it to an optical combiner. The horns in each back-to-back pair are corrugated as a low sidelobe level and low cross-polarisation were considered important in the original design described in (Cavaliere et al. 2020). QUBIC operates in two frequency bands, the lower one centred at 150 GHz, the higher at 220 GHz. The horns were designed to transmit radiation in both frequency bands simultaneously (approximately 130–240 GHz) and so are very wide-band. Observing the CMB in multiple frequency bands is crucial to the subtraction of contaminating foreground sources.

One possibility being considered by the QUBIC collaboration is to design a QUBIC-like instrument that could be placed at the focal plane of the LLAMA telesope, also under construction at La Salta province in Argentina (Romero, 2020). One question arose as to whether it would be possible to modify the QUBIC horns so that they could also transmit radiation in a third, lower, band at 90 GHz. Although it was suspected that 76–240 GHz would be too wide, electromagnetic mode-matching with PyScatter was used to find the full band of the current QUBIC horn design and to see whether any straightforward modifications to that design could allow operation at 90 GHz.

4.2.2 The existing QUBIC horn design

To begin with, the existing horn geometry was analysed using PyScatter. The code was modified to plot the normalised far-field beam pattern at frequencies from 90 to 220 GHz, in steps of 1 GHz. Cuts of each pattern were taken at 0, 45 and 90 degrees (an example was shown in Fig. 4.5).

As a measure of the correct operation of the horn, the first sidelobe level, relative to the on-axis gain, was calculated in dB at each frequency step in the 90 to 220 GHz range encompassing the higher band at 220 GHz, the band at 150 GHz, and the newly introduced lower band at 90 GHz. The results are shown by the orange trace in Fig. 4.6. If no beam is produced the level defaults to 20 dB. It can be seen that the horn fails to propagate radiation below 126 GHz, and has a sharp mode cutoff. The frequency at which cutoff occurs can be predicted using the propagation characteristic of the hybrid modes that propagate

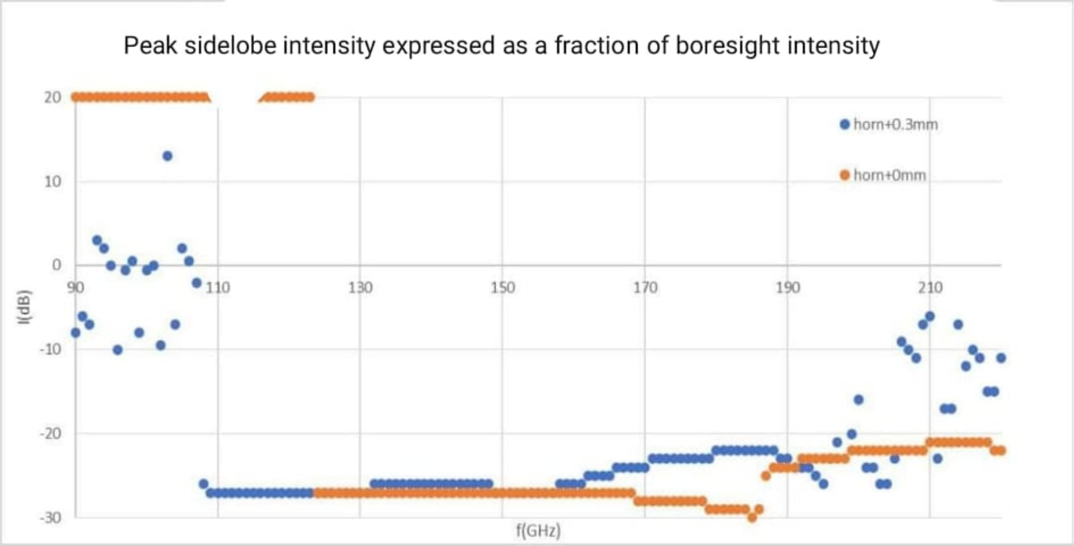

FIGURE 4.6: Comparison of original and wider horn, showing sidelobe level at 1 GHz intervals throughout the bands.

in corrugated horns. As it is the narrowest part of a back-to-back horn pair, the throat width of the horns (Fig. 4.8) is what determines the modes that can propagate. The cutoff, for a given corrugation ratio (r_1/r_o) in the guide, can be read from plots such as as Fig. 4.9. For QUBIC, the narrowest part of the throat section has $r_1 = 0.684$ cm and $r_0 = 1.394$ cm giving $r_1/r_o = 0.491$. The QUBIC horn was designed to propagate the single HE11 mode and from Fig. 4.9 the y value corresponding to HE11 at corrugation ratio 0.491 is approximately 1.8. The units are $\omega r_1/c \approx 1.86$, solving for frequency

$$f_{min} = \frac{1.8c}{2\pi r_1} = 129 \text{ GHz}. \tag{4.3}$$

For comparison, the general cutoff frequency for a smooth-walled cylindrical guide of radius a is

$$f_{min} = \frac{1.8412c}{2\pi a} = 128.5GHz. \tag{4.4}$$

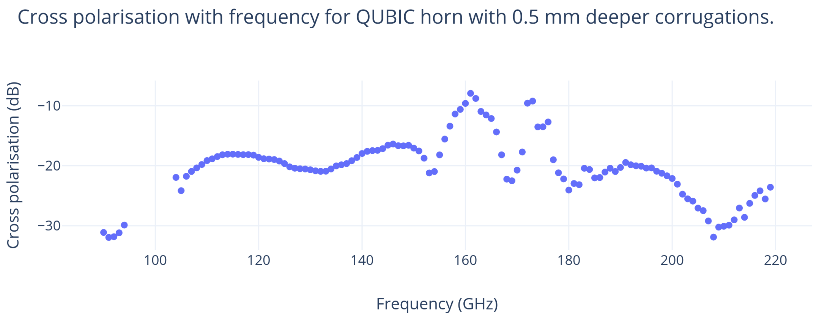

FIGURE 4.7: Cross polarisation plot for QUBIC horn with deeper corrugations. The cutoff section at low frequencies is visible, along with generally poor cross polarisation.

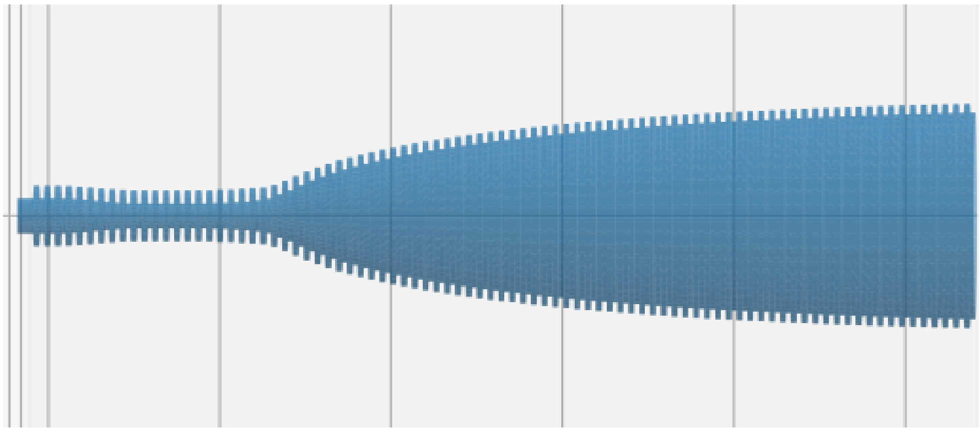

FIGURE 4.8: Plot of the QUBIC horn design. The corrugation sections are 0.3 mm in length, for scale reference. The waveguide and throat sections discussed earlier are clearly visible.

4.2.3 Modification to the QUBIC horn design

In order to increase the functional waveband of the QUBIC horn down towards the 90 GHz target, the first thing to consider is the width of the waveguide and throat of the horn, as a wider guide permits mode transmission at lower frequencies. To widen the horn, the input geometry file was altered by adding a fixed value to each of the r_0 and r_1 values along the full length of the horn. The plot in Fig. 4.6, shows an example when a test value of 0.3 mm was added. It can be seen that an increase in the overall horn width causes a decrease in the functional waveband of the horn towards the desired lower frequency band. In this case the cutoff shifted to 108 GHz but there was, however, a corresponding decrease in performance at the upper end of the band.

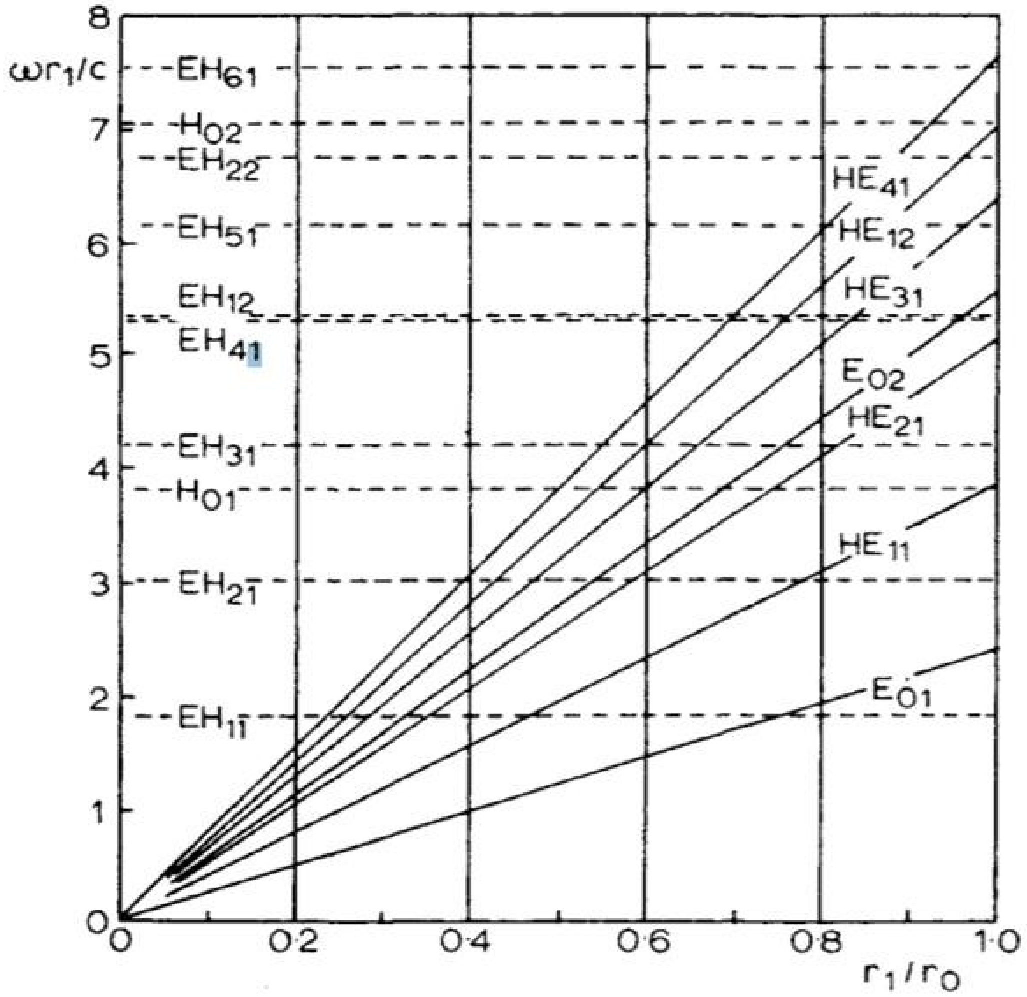

FIGURE 4.9: Lower limit mode cutoff graph for various HE and EH modes of corrugated horns (Clarricoats, P. Olver, A, 1984).

A second method was tried where r_0 was increased but not r_1 i.e. deeper slots in a wider horn. This reduces r_1/r_0 and moves the horn to the left along the HE11 cutoff line in Fig. 4.9 to lower values of $\omega r_1/c$. Since r_1 was not changed this has the effect of lowering the cutoff frequency ω. The corrugation slots were deepened by 0.5 mm along the length of the horn, and the data was again analysed in PyScatter. This simulation returned no data for most points below 106 GHz, implying full mode cutoff. A few frequencies appeared to propagate, below 106GHz, but this is unlikely to be a physically valid result. Additionally, the cross polarisation began to spike in the centre of the band, as shown in Fig. 4.7

A final geometry file was created to investigate performance across the three bands of a smooth walled horn. A Python script was used to flatten out the corrugations to a smooth, rolling mean along the length of the horn. This retained the curvature and slope of the horn, while removing the corrugations. Because there are no corrugations, there is no high-frequency mode cutoff in the system. Fig. 4.10 and Fig. 4.11 show beam patterns calculated for the horn at 155 and 220 GHz. The improvements afforded by corrugating the horn are made abundantly clear by comparison with Fig. 4.6. In the case of the smooth-walled horn the main lobe is not symmetric and the sidelobe level (-9 dB) and cross-polarisation level (-10 dB) are much higher than for the corrugated horn. Since the current design of QUBIC has a HWP and polarizer (see Chapter 3) and its calibration scheme should be able to deal with an asymmetric beam, future versions of the instrument may not have such tight requirements for beam symmetry and cross-polarization and smooth-walled designs could be considered.

4.3 Summary

The aim of the research outlined in this chapter was to investigate an existing horn design for the QUBIC instrument. QUBIC currently operates over two bands, centred at 150 and 220 GHz, and the possibility of extending that to a third 90-GHz band was considered. The horn was varied by changing individual parameters such as waveguide diameter and slot depth, with the intention of extending its lower operational limit. This was partially successful, as the lower frequency limit at which the horn remained well-behaved was brought from $\sim$ 126 GHz to $\sim$108 GHz. However, a corresponding reduction in performance at the higher band nullified this benefit. Finally, a smooth-walled

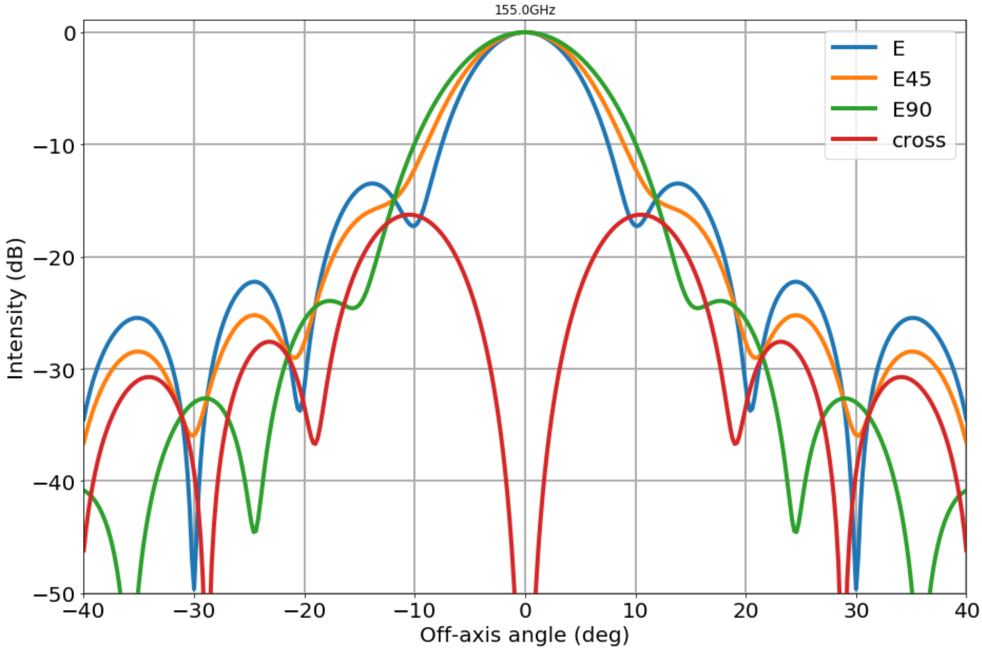

FIGURE 4.10: Sample pattern plot of transmitted angular power at 155GHz for a smooth walled horn at 0, 45 and 90 degrees to the polarisation axis. Cross polarisation is included as a red trace.

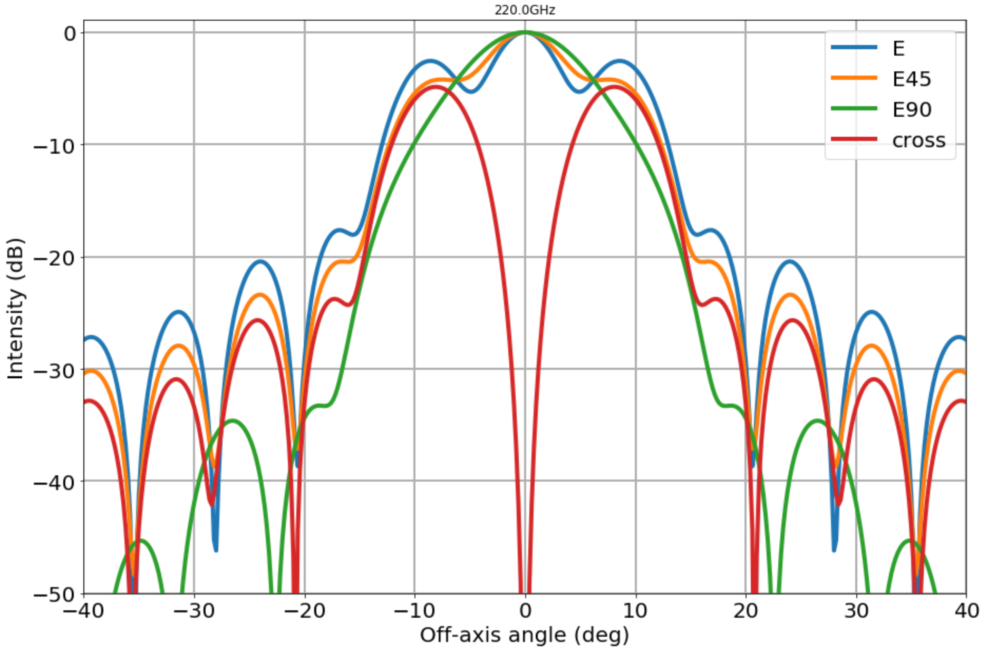

FIGURE 4.11: Sample pattern plot of transmitted angular power at 220GHz for a smooth walled horn at 0, 45 and 90 degrees to the polarisation axis. Cross polarisation is included as a red trace.

version of the QUBIC horn was designed to illustrate the advantageous effect of corrugation. The smooth-walled horn had much poorer performance, with very high cross-polarisation and sidelobes at -10 dB, compared to -25dB for the corrugated horn at the same frequency.

The work described here showed that a simple solution for extending the QUBIC observing band is unlikely to be found and a more bespoke re-design of the corrugated horns should be done.

Chapter 5

ALMA Collaboration

5.1 Introduction

5.1.1 The Maynooth-Manchester collaboration

The research outlined in this chapter was completed in collaboration with colleagues from the Advanced Instrumentation Group (AIG) of Manchester University. The AIG won funding from ESO for the design, development and production of extremely sensitive, broadband low-noise amplifiers (LNAs) in order to upgrade the capabilities of the ALMA telescope. In the future they plan to dramatically enhance the field-of-view of the ALMA telescope by deploying focal plane arrays or phased array feeds (PAFs). The increase in sensitivity promised by these LNAs can only be realised if they are well coupled to the sky and critical to achieving this is the design of the passive optical elements, primarily the feed-horn and ortho-mode transducer (OMT). The design of these components is especially challenging due to the large fractional bandwidth of operation desired. The OMTs were designed by Mark McCulloch in Manchester and the aim of the work presented in this chapter was to design suitable corrugated horns to feed them.

This work aimed to construct and then simulate corrugated horns to meet the requirements set out for receivers operating within various bands of the EM spectrum. Two particular regions were identified for consideration. The primary design would be for a wideband horn covering combined ALMA bands 4 and 5, with a secondary project to cover the Ka band, a much lower frequency, with less bandwidth. The lower frequency design is one that could be manufactured and tested in Manchester, spanning 26.5-40GHz.

Three horn designs were analysed. An initial 84 corrugation horn was simulated but was deemed too costly to manufacture due to the large number of sections. A smaller, 35 corrugation, horn was made to satisfy this requirement.

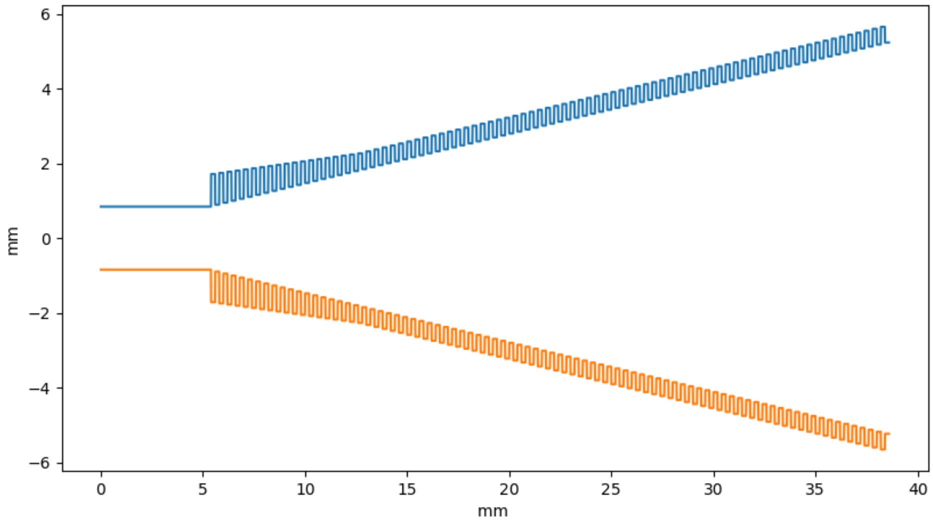

FIGURE 5.1: Longitudinal profile of prototype horn for use in ALMA bands 4 and 5.

This horn was then modified slightly to produce a third design (30 corrugations), to comply with the thickness of aluminium plate available from the supplier. The three designs will be detailed and compared below. A tolerance analysis is also provided for the second and third designs.

5.1.2 Design and modelling

Conical corrugated horns were designed following principles given in the literature, as will be described. A routine was developed in Python to construct a longitudinal cross-sectional horn profile (PyScatter geometry file) from the resulting series of input design parameters; such a profile for the final ALMA prototype horn is shown in Fig. 5.1. The horn was then modelled using the electromagnetic mode-matching technique with the in-house software PyScatter as has been described in Chapter 4.

Scatter produces the scatter matrix for the profile from which the sub-matrices $[\mathbf{S_{11}}]$ and $[\mathbf{S_{21}}]$ are extracted. The transmitted and reflected mode coefficients are calculated using Eqns. 4.2 with $[\mathbf{A}] = [1, 0, 0, ...]$, i.e. exciting the one input mode, TE_{11}, that can propagate through an input circular waveguide. Fields are calculated by summing modal fields, weighted by the relevant mode coefficients.

The number of waveguide modes included determines the accuracy of the scattering analysis. For initial testing, 40 waveguide modes were used, rising to 60 (30 TE and 30 TM) for the final analysis and plotting. Including the additional modes did not alter the farfield patterns out to the relevant angles from boresight. The TE and TM modes with power at the aperture have a coherent phase relationship and in this case correspond to the single hybrid HE11 mode (a singular value decomposition (SVD) of the [S] matrix results in one singular value). The PyScatter software is computationally less intensive than a finite element approach and can be used to investigate the performance of the horn over a range of frequencies. Once designed, the beam patterns were verified by comparison with those produced by the commercial software HFSS.

5.1.3 Analysis

The transmitted field at the horn aperture is propagated into the far field to yield the beam profile at a given frequency. The FHWM and peak cross-polarisation level are recorded. Return loss is calculated by summing the power (sum of the squared mode coefficients) in each column of the $[\mathbf{S_{11}}]$ matrix. The return loss, FWHM and cross-polarisation were computed for each frequency of interest, and plotted to show the performance of the horn across the band. For initial testing a frequency resolution of 1 GHz was used, increasing to 0.05 GHz for the final results.

5.2 ALMA band 4-5 horn designs

5.2.1 Constraints and the horn design

The specifications to be met by the horn designed in this project were based on those given by Yagoubov et al. (2018) and are listed in Tab. 5.1. This published work was developed for the lower frequency ALMA bands 2 and 3, as opposed to 4 and 5, but was of particular relevance as it spanned two bands, while most receivers are designed for a single band.

The central frequency for the ALMA bands 4-5 horn was chosen as 168.5 GHz, the midpoint between the 125 GHz lower edge of ALMA band 4, and the 216 GHz upper edge of ALMA band 5. This gives a required bandwidth about the central frequency of ± 26%. This is quite a wide range, incurring a likelihood of reduced performance at the edges of the band.

TABLE 5.1: Horn requirements

Parameter	Requirement
Centre frequency [GHz] . .	168.5
Frequency range [GHz] . .	[125-216]
FWHM at band centre [degrees]	[14-16]
Cross-polarisation [dB] . . .	[<-30 ideal]
Return loss (S_{11}) [dB]	[<-15, <-20 goal]

A circular conical corrugated horn was designed as a base to which further modifications could be made. This type of horn is widely used for its high beam symmetry and low cross-polarisation.

The width of the waveguide and throat of a horn is of paramount importance in determining which modes will be allowed through at a given frequency. Typically, it is desirable to allow only the TE_{11} fundamental mode to propagate from an input circular guide to the throat of the horn. The fundamental mode cutoff frequency for a circular waveguide of radius a is given by 4.4, as discussed earlier. The constant in this equation is the first root of the derivative of the Bessel function of the first kind. A narrow waveguide diameter, approaching cutoff at the lower end of the desired frequency band, will lower cross polarisation across the band. It also reduces the likelihood of multimodal transmission at higher frequencies; however, these benefits are tempered by the return loss requirements for the system. If the waveguide diameter is extremely close to cutoff at a given frequency, a significant amount of power at that frequency will be reflected back down the waveguide upon striking the first corrugation. A suitable balance between cross-polarisation and return loss was achieved at a diameter of 1.2 times the theoretical cutoff for the largest wavelength of the band for the initial model (1.688 mm in diameter for ALMA band 4-5). The final models refined this to 1.17.

The hybridisation section is a junction between the waveguide section and the body of the horn. Its purpose is to hybridise the TE and TM modes into one or multiple HE/EH modes (in this case the single HE_{11} mode). Typically this is achieved by varying the corrugation depth from an initial $\lambda_{\text{central}}/2$ to the $\lambda_{\text{central}}/4$ standard used for the remainder of the horn to improve modal purity, where λ_{central} is the central wavelength of the operating band. This reason for this choice of corrugation depth is outlined in detail in Clarricoats and

Olver (1984), and applied in e.g. Zaman, Matin and Gaffar (2011). The corrugation depth is varied linearly across a specified number of corrugations to be included in the section. It was found that increasing the depth of the initial transition corrugations reduced the return loss, but increased cross polarisation at higher frequencies. Thus, simulations were run varying the depth at which the linear variation began. The optimal compromise was found to be 0.48 λ in this instance. A 20 corrugation transition section was used for both models. Slot depth reduced linearly from $0.48\lambda_{\text{central}}$ to $0.25\lambda_{\text{central}}$ for the initial design, and $0.42\lambda_{\text{central}}$ to $0.25\lambda_{\text{central}}$ for the final designs, as shown in Fig 5.1.

The aperture dimension is the size of the mouth of the horn, where the final impedance matching takes place, and is largely determined by the required FWHM. A wider mouth brings the impedance of the widest corrugations closer to that of free space, thus smoothing the transition and reducing the return loss. However, increasing the aperture diameter for a given horn flare angle also increases the horn length, and this is not desirable for real instruments which often must fit into a limited volume. For small flare angles, the beamwidth depends on λ/D, as expected (Fig. 5.2). However, as flare angle is increased, the beamwidth no longer decreases indefinitely with D. For widths above 20-30 degrees, the minimum possible beamwidth increases rapidly. The flare angle of the horn may be chosen quite freely, but a very wide-angled horn will be short, with relatively few corrugations. These factors may result in poor directionality and high return loss. For the ALMA band 4-5 initial horn, a flare angle of 7.5 degrees was chosen. This was extended to 10.8 degrees for the final design, to aid in reducing the number of sections.

The aperture diameter of the initial design was 5.9 λ_{central}, 10.47 mm for ALMA 4-5. The corrugation height affects the exact final radius. From Fig. 5.2, we see that the predicted half beamwidth for $D = 5.9\lambda_{\text{central}}$ and flare angle $\theta = 7.5^\circ$ is approximately 6.5 degrees. This corresponds to a FWHM of 13 degrees, somewhat more directional than the requirement of 15 degrees. However, upon computing the FWHM across the band, the mean FWHM was closer to the target than suggested by the graph, as discussed in the analysis section. Additionally, the return loss was improved somewhat by the low angle and large size of the design. The aperture diameter of the final designs was reduced to 5.4 λ_{central}, or 9.6 mm. This is chosen to reduce the number of sections further, while minimising impact on the FWHM.

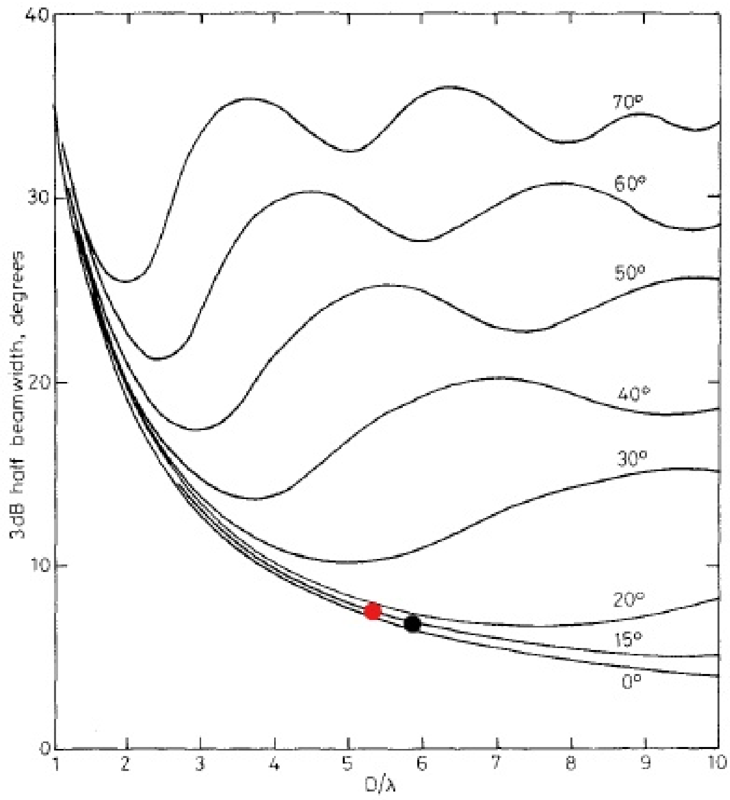

FIGURE 5.2: The dependence of FWHM on flare angle and wavelength-normalised horn diameter for circular conical corrugated horns. (Clarricoats, 1984). The position of the initial design for the ALMA band 4-5 and Ka band horns are indicated by a black dot on this plot. The final designs are indicated by a red dot. The frequencies of the ALMA bands are shown in Table 3.1.

For the initial horn, a slot to corrugation width ratio of 1:1 was chosen as a starting point, making the grooves of equal width to the corrugations. The length of the corrugation cycle was varied for optimal balance between cross polarisation and return loss, returning a value of 0.4 mm as the optimal compromise. This cycle width was chosen for the initial ALMA band 4-5 horn. Each section in the geometry file corresponds to either a corrugation or a groove and so has a width of half of this, 0.2 mm. This gives more than four corrugations per wavelength. The second design had a corrugation cycle of 0.6 mm to reduce corrugation number for economical manufacture. This was subsequently extended to 0.7 mm for the third design, as the sheets of aluminium available for machining suited this thickness. The initial ALMA band 4-5 initial design is shown in Fig. 5.1, for reference.

5.2.2 Results

The results of the PyScatter analysis of the ALMA 4-5 design are summarised in Figs. 5.3-5.5 which show the changing performance of the 84-corrugation horn with frequency. The frequency resolution of the plots is 0.05 GHz, giving 1820 datapoints across the band. The high resolution was used to more accurately probe variations in the lower part of the frequency band, which were not well defined using lower resolution frequency scans.

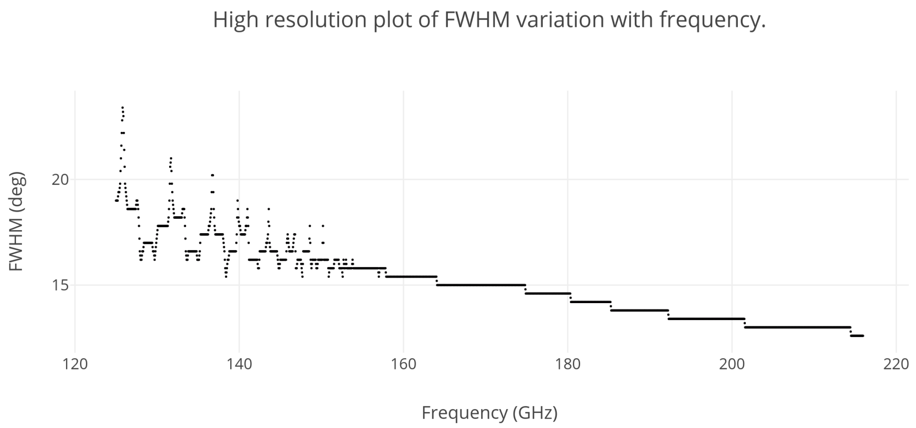

FIGURE 5.3: FHWM dependence on frequency, as computed by PyScatter. (Design 1: 84-corrugation horn.)

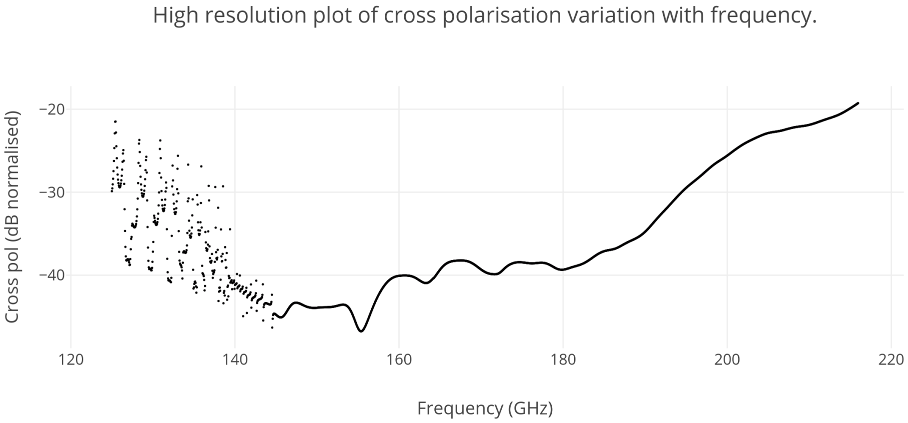

FIGURE 5.4: Cross polarisation dependence on frequency, as computed by PyScatter. (Design 1: 84-corrugation horn.)

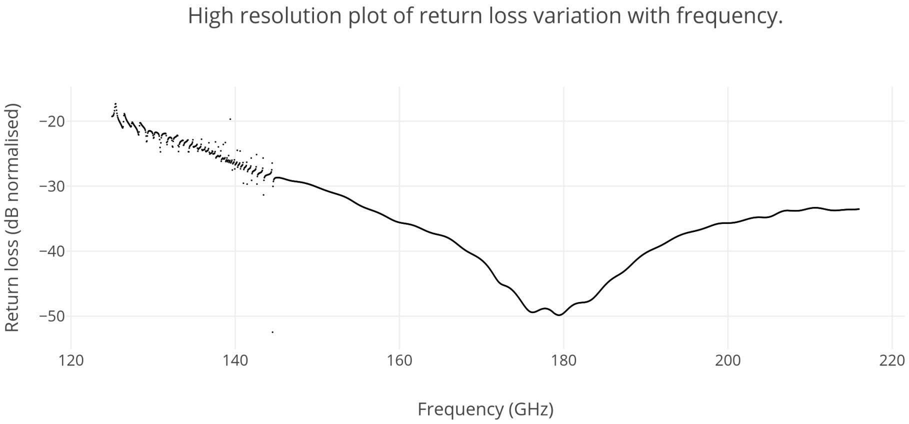

FIGURE 5.5: Return loss (S11) dependence on frequency, as computed by PyScatter. (Design 1: 84-corrugation horn.)

The FWHM plot shows a beamwidth that changes rapidly with frequency in the lower part of the band. This settles down to the expected steadily decreasing width above 150 GHz. The FWHM graph shows discrete jumps, unlike the other plots, because of the finite angular resolution of 0.2 degrees. Adding further resolution wasn't considered necessary in the case of FWHM, due to its slow and highly uniform change with frequency. The mean FWHM across the plot is 14.3 degrees, ensuring that the beam in the central region of the waveband has a width within the 14-16 degree range. The central frequency FWHM was thus modelled to be slightly wider than the 13 degrees predicted earlier by Fig. 5.2.

The cross-polarisation also changes with frequency but stays below about

-20 dB and is less than -40 dB in the centre of the band. The cross-polarisation of -19 dB at the very lower end of the band is slightly above the desired level and is one of the compromises made for obtaining very wide bandwidth.

The return loss is more stable at low frequencies than the other measured characteristics. The value oscillates in the 120-150 GHz region but remains below -30 dB above 150 GHz. In the 140-145 GHz region, this oscillation takes the form of a series of expanding asymptotic curves. The predicted structure in the frequency response at the lower end of the band could be real or potentially an artefact of the PyScatter algorithm, which involves matrix inversion. In particular, the matrix arithmetic involved in cascading the sections of the horn could introduce float division by zero errors, explaining the asymptotes. To verify the low-frequency results, the Manchester team analysed the radiation performance of the ALMA band 4-5 horn using HFSS, which uses a finite-element approach and thus would not likely possess the same artefacts. As shown by figure 5.6, the artefacts were not present in HFSS. PyScatter shows smooth asymptotic curves, approaching a bilateral asymptote at a range of single points. HFSS shows low level fluctuations ($\sim \pm 1$ dB), with no periodic nature observed. Both software packages agree, however, on the general trend of the return loss, varying from approximately -26 dB at 140 GHz, to -28 dB at 145 GHz. This suggests that the observed patterns in the PyScatter data are indeed an artefact, and will not likely be measured from a real physical horn.

The 84 corrugation horn was deemed too expensive to machine in the near future. In light of this, the results for the re-designed horn with a smaller number of corrugations are shown in the next section, together with a full tolerance analysis performed for potential machining of this horn.

5.3 Tolerance analysis

Tolerancing is required to determine the degree of precision required in machining horns, as a horn with greater tolerance for error is typically quicker and/or cheaper to produce, while also allowing for greater choice of production methods. These advantages are minor in the case of a single horn, but are compounded for a large array, making cost and time viability critical to the design. A series of examples in the literature are presented in Tab. 5.2, which lists the author and year of publication, the tolerance level achieved, the horn manufacturing method employed to achieve it, and critically, the frequency at

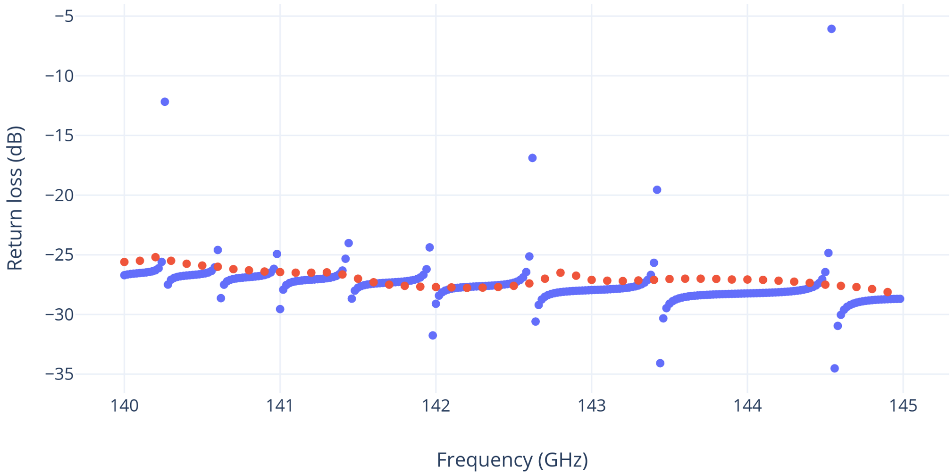

FIGURE 5.6: Return loss as a function of frequency for the ALMA band 4-5 horn (Design 1: 84 corrugations). Comparison of high frequency scans of a 5 GHz band section using HFSS (red) and PyScatter (blue), showing anomalous patterns in the PyScatter data.

which the horn operated. In general, a horn designed to operate at a lower frequency will have a greater tolerance, as the manufacturing errors incurred represent a smaller fraction of λ.

To determine the effect of machining tolerances on the horn design with a reduced number of corrugations (Design 2: 35 corrugations), a Python routine was written to vary the depths of the corrugations. This was conducted by selecting a pseudorandom number from a uniform distribution, centred on the true corrugation size, and extending to the relevant tolerance limits. Tolerances are mostly constant throughout the depth of the horn (with a small nonlinear component possible for rotating-spindle based methods, due to flexion in the spindle), however they become an increasingly larger fraction of the overall diameter as one approaches the throat. This implies that the throat section is most vulnerable to the detrimental effect of inaccuracies. Two methods were used to approximate tolerances, a general approach, using uniform random variations of the first twenty corrugations, and a more complex two step approach tailored to the machining methods to be used,

5.3.1 Single level throat tolerance

To implement this method, 20 geometry files were prepared for each tolerance level, each with a unique randomly varied throat section (taken as the first 20

TABLE 5.2: Machining tolerances in the literature.

Author	Tolerance	Method	Frequency
Villa et al., 2002	10 μm	Cu electrodeposition on Al plug with Au plating	100 GHz
Del Torto et al., 2011	30 μm	Al platelet stacking	100 GHz
Mandelli et al., 2021	30 μm	CNC milled and etched Al platelet stacking	155 GHz
Britton et al., 2010	10 μm	Si micromachining, ion etching, Cu, Au plating	150 GHz
Francechet, 2021	60 μm	Chemically etched Al platelet stacking	95 GHz

sections in the geometry file). The variation was estimated as a random value in the range $\pm\Delta$, where Δ is the stated tolerance value. The performance was examined at 5 GHz intervals across the band. An example of the data generated is shown in Fig 5.7. Plots of beam parameters as a function of frequency were then prepared, which were compared with the ideal parameter for the as-designed horn. An approximate range was shaded around the mean curves in Figs. 5.8 to 5.10, by taking the standard deviation of the dB values for all data points at a given frequency. This will not constitute a true standard deviation due to the logarithmic nature of the data, however it is included as a guide to compare the variation at different points across the waveband. Plots of beam width are not included in the results for the tolerance analyses, as the values obtained were almost identical to those for the nominal section widths. This can be explained by the fact that beam width depends primarily on the aperture diameter and flare angle. As such it is not extremely sensitive to slight changes in corrugation widths, as the other beam parameters are, ±0.2 degrees is typical.

Three tolerance levels were analysed: ±25 μm as a typical tolerance, ±50 μm as an example of crude tolerance, and finally, ±100 μm to show the effect of an unrealistically poor manufacture, and thus demonstrate the requirement for the precision levels commonly used in industry.

It is clearly shown by Fig. 5.10 that a tolerance of 100 μm would be wholly

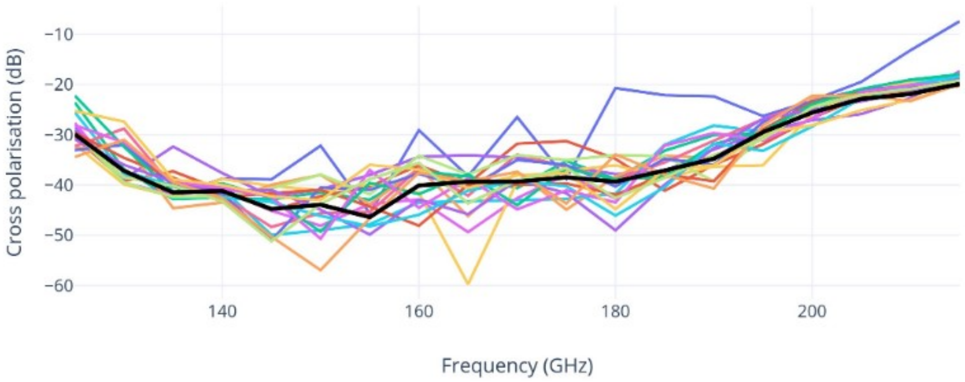

FIGURE 5.7: Cross polarisation as a function of frequency for 20 realisations of the horn with ±25 μm error. The coloured traces show the performance of individual iterations, while the thick black trace represents the nominal horn design.

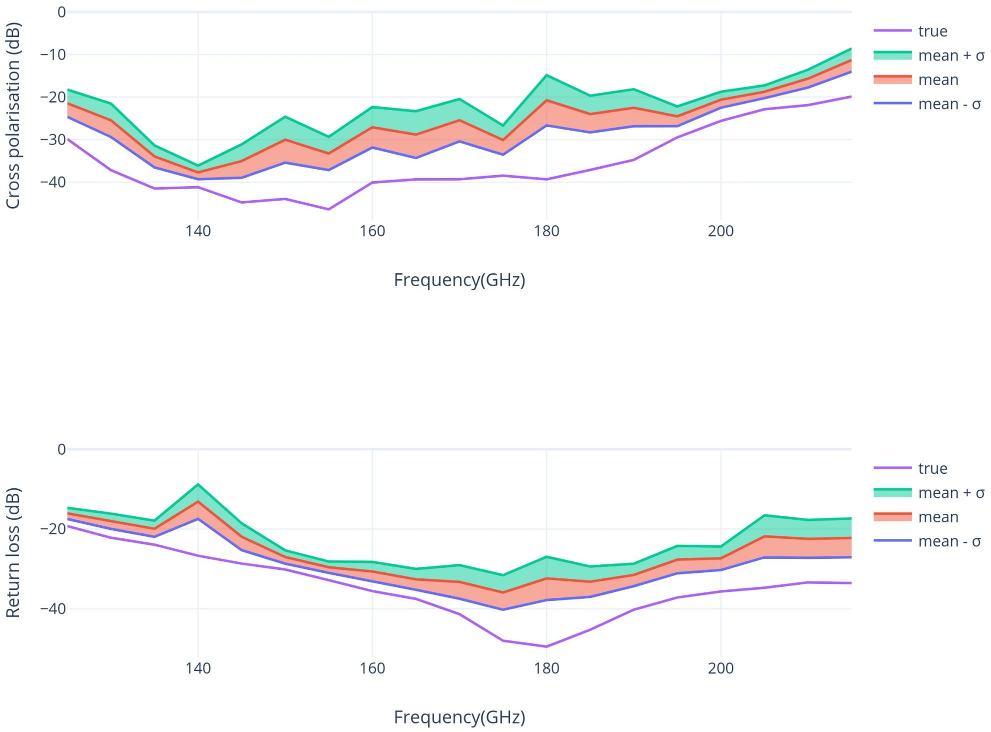

FIGURE 5.8: Cross polarisation and return loss as functions of frequency for 20 realisations of the horn with ±25 μm error (mean and standard deviation were calculated as explained in the text). The single unshaded line denotes the ideal case.

unsuitable for components at this waveband. Mean cross-polarization and return loss levels are almost 10 dB above the ideal design. Conversely, Fig. 5.9

FIGURE 5.9: Cross polarisation and return loss as functions of frequency for 20 realisations of the horn with ±50 μm error (mean and standard deviation were calculated as explained in the text). The single unshaded line denotes the ideal case.

shows a more modest 4-5 dB average increase in both cross-polarization and return loss across the band. However, the return loss at the upper end of the band is still adversely affected. This is to be expected as at higher frequencies, the errors included represent a larger fraction of λ. The 25 μm dataset, Fig. 5.8, shows very minor reduction in performance, on the order of 1-2 dB. Additionally, the deviation of the values is much smaller, indicating that it is very unlikely that any particular horn would perform poorly. The final conclusion from these data is that the analytical horn design outperforms the deviated designs in all three cases at all frequencies. The <25 μm tolerance level is thus adopted as the goal to aim for in considering the machining methods available for manufacture.

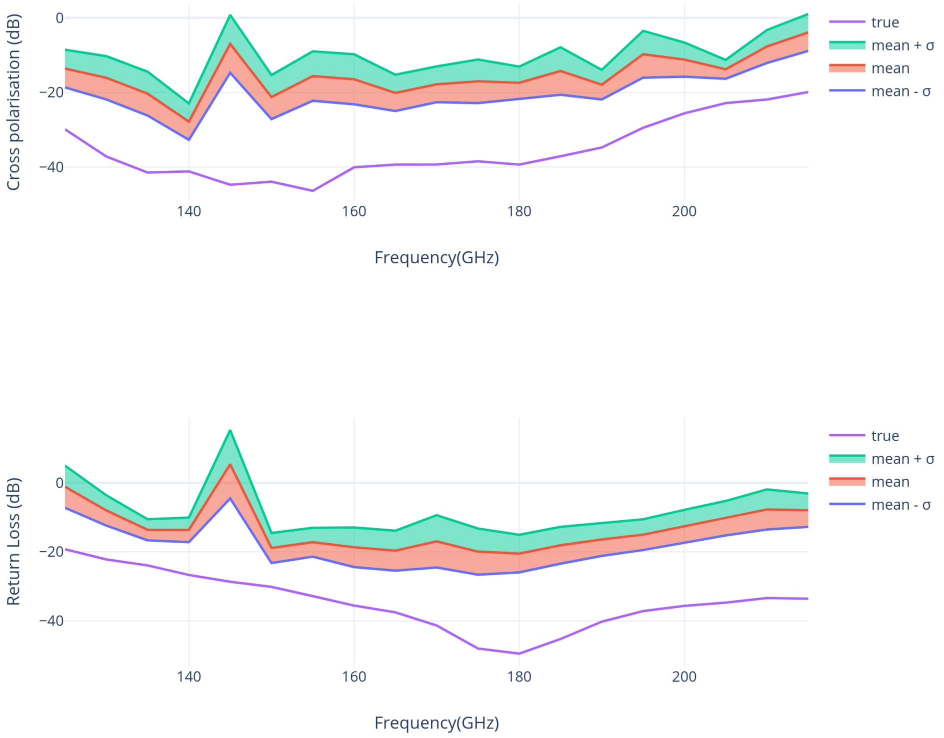

FIGURE 5.10: Cross polarisation and return loss as functions of frequency for 20 realisations of the horn with ±100 μm error (mean and standard deviation were calculated as explained in the text). The single unshaded line denotes the ideal case.

5.3.2 Two level full-length tolerance

The option arose during the project of machining each horn in two parts which would subsequently be bolted together into a small array of identical horns. The first 18-20 sections would be realised in plate aluminium, using a platelet manufacturing approach, as previously used by Francechet (2021). The circular section cuts would be performed using laser micromachining. This could give a better tolerance than more conventional machining approaches, however its substantial cost makes it unsuitable for fabricating the whole array. An electroforming process was chosen to create the remaining lengths of the horns individually. These would then be bolted to the positions on the aluminium sheet which correspond to the micromachined throats. A schematic of this procedure in various stages of completion is shown in Fig. 5.11, courtesy of Mark McCulloch and the Manchester team.

To approximate the inaccuracies in a two-step manufacturing process, each

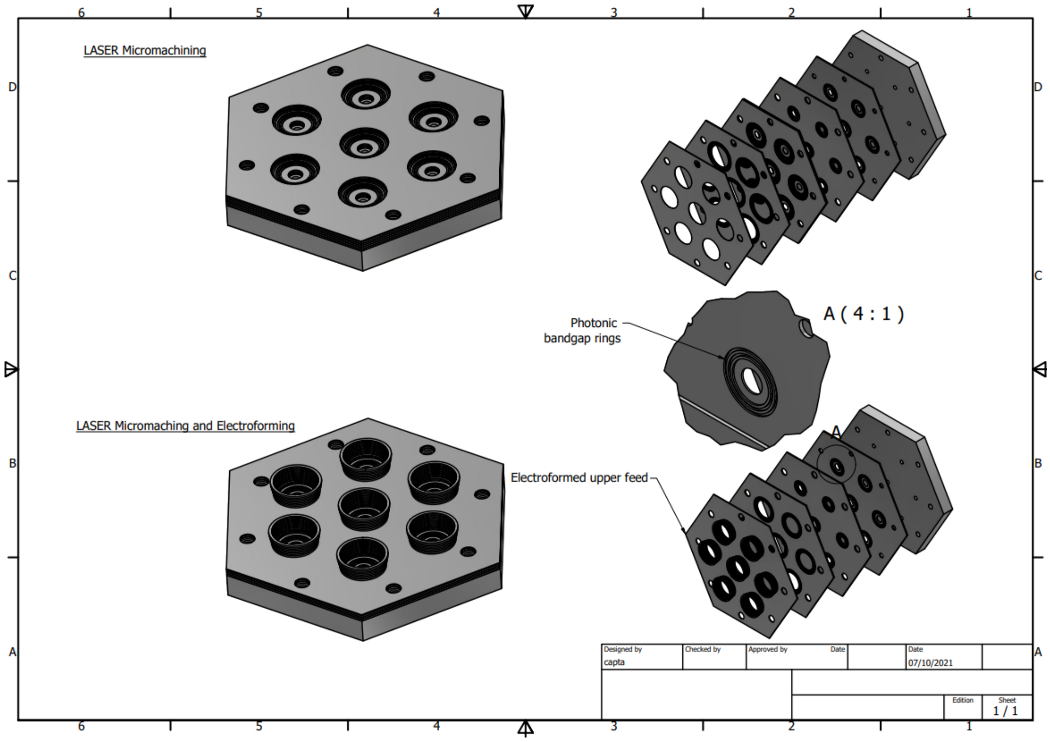

FIGURE 5.11: Schematic of laser micromachined plates, (right) individually, (top-left) stacked, and (bottom-left) with the electroformed horn bodies attached. Credit: M. McCulloch, Manchester University.

tolerance level was split in two, corresponding to the different accuracy inherent in each of the techniques used. A best case scenario was taken as 5 μm for the lasered section and 10 μm for the electroformed section. Average performance was simulated with 10 μm and 20 μm, while worst case used 20 μm and 40 μm. The tolerances were applied in the same manner as for the previous analysis. It is of note that these are in general a tighter set of values than were produced previously, as the techniques chosen do not typically reach 50 μm or 100 μm error levels. As such, performance closer to the nominal would be expected. The results for each of the three levels in cross polarisation and return loss are shown as Figs. 5.12-5.17. The cross polarisation is affected much more severely than the return loss for these tolerance analyses.

5.3.3 Material constraints

The aluminium for micromachining was difficult to source in bespoke sizes. A set of 0.7 mm plates were available to the Manchester team to supply to the laser micromachining firm, who would burn a single corrugation slot into each plate before stacking them together. The individual sections would thus

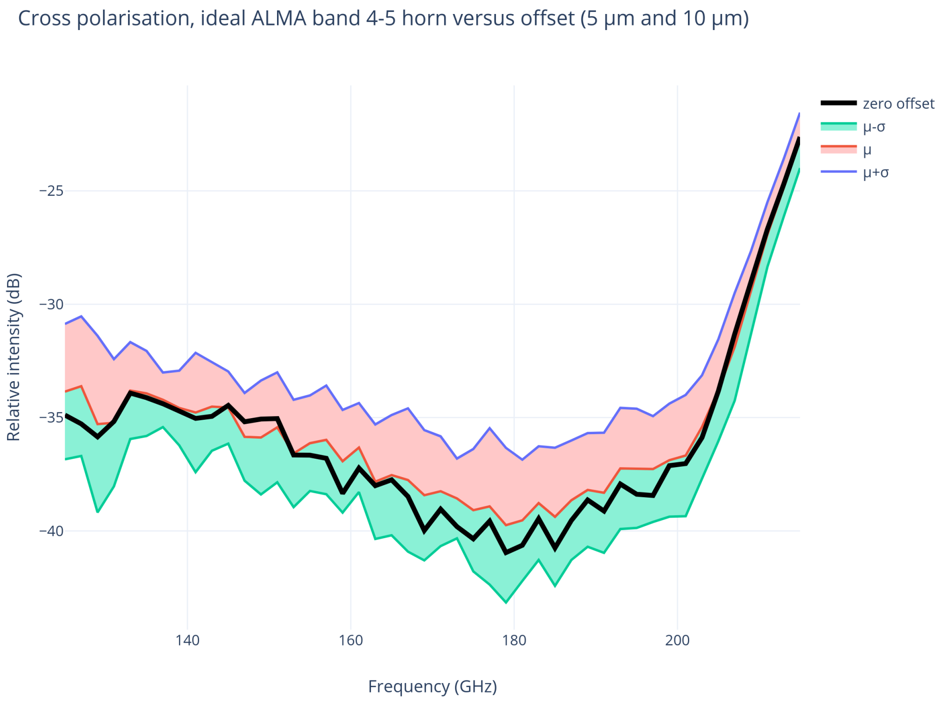
Cross polarisation, ideal ALMA band 4-5 horn versus offset (5 μm and 10 μm)

FIGURE 5.12: Cross polarisation for ±5μm toleranced throat section and ±10μm toleranced remainder.

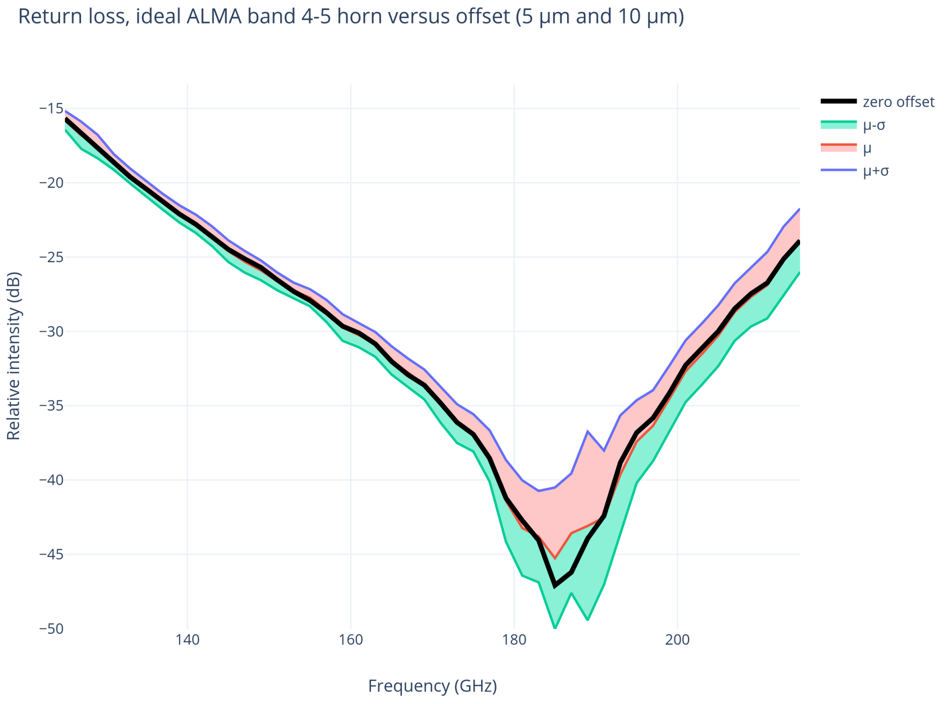
Return loss, ideal ALMA band 4-5 horn versus offset (5 μm and 10 μm)

FIGURE 5.13: Return loss for ±5μm toleranced throat section and ±10μm toleranced remainder.

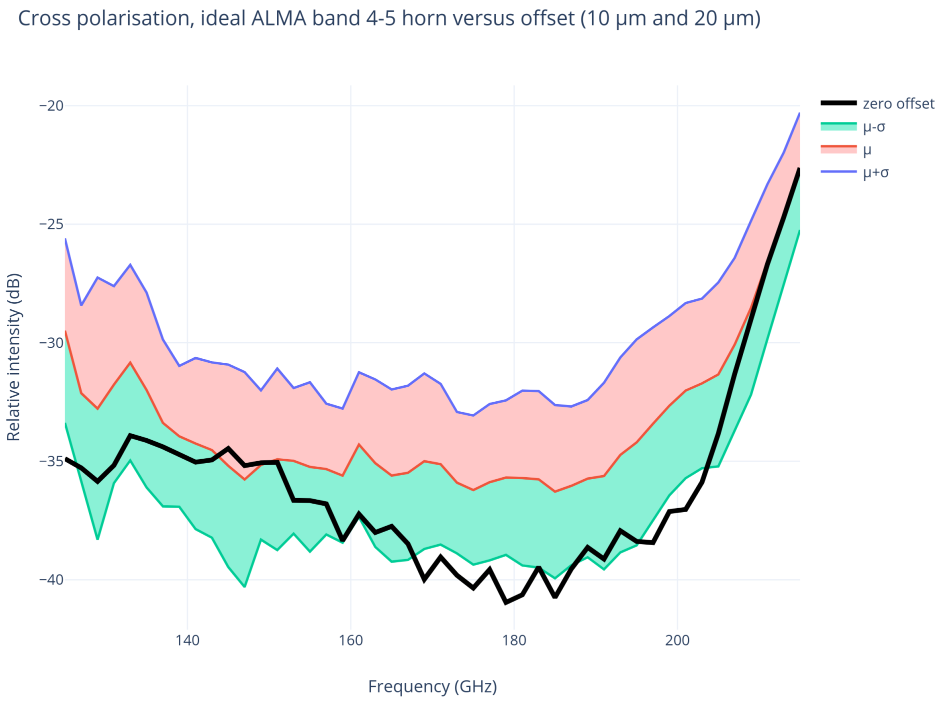

FIGURE 5.14: Cross polarisation for ±10μm toleranced throat section and ±20μm toleranced remainder.

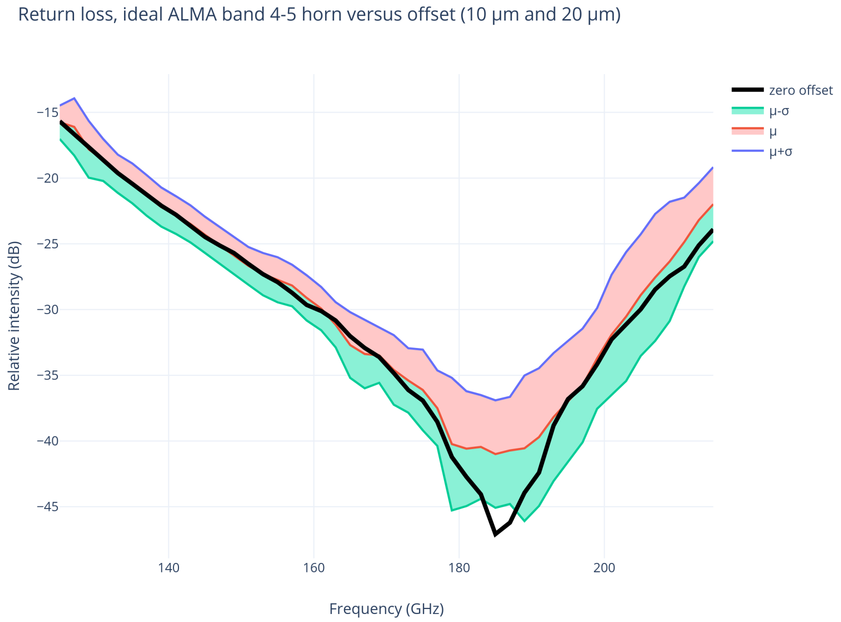

FIGURE 5.15: Return loss for ±10μm toleranced throat section and ±20μm toleranced remainder.

be 0.35 mm in thickness, rather than the 0.3 mm used in the previous analysis. To preserve the general shape of the horn, the number of corrugations would

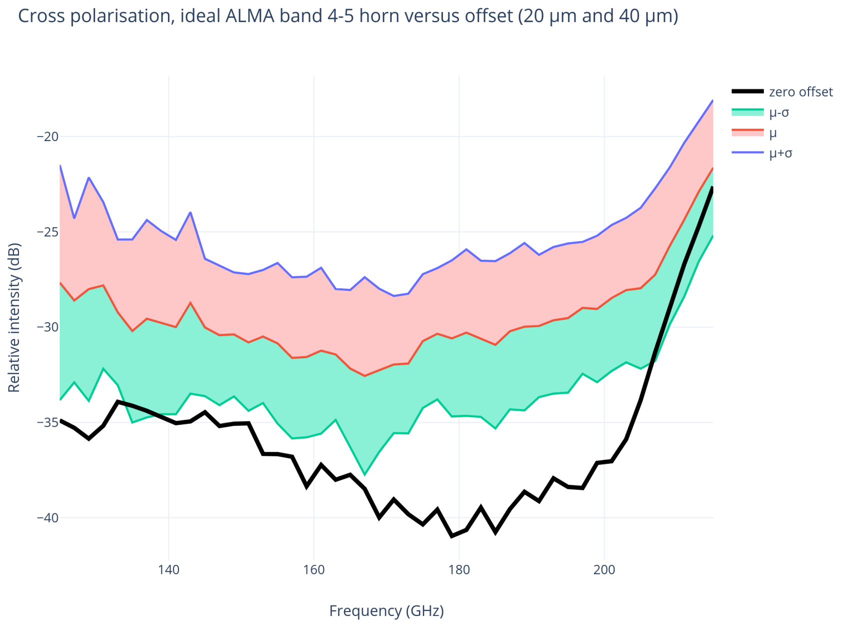

FIGURE 5.16: Cross polarisation for ±20μm toleranced throat section and ±40μm toleranced remainder.

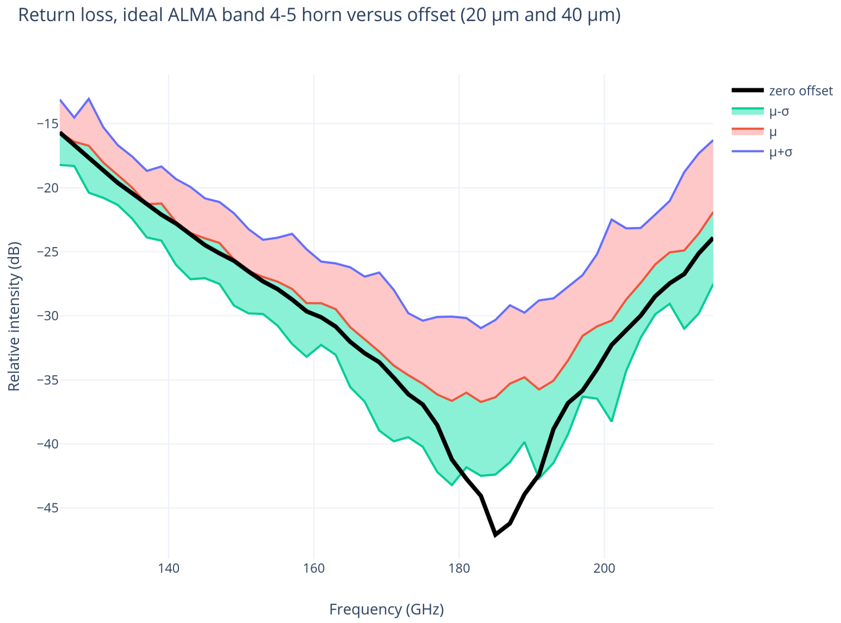

FIGURE 5.17: Return loss for ±20μm toleranced throat section and ±40μm toleranced remainder.

thus have to be reduced from 35 to 30 (Design 3). This required the generation of a second set of geometry files, with their associated beam parameters and tolerances, to compare with the nominal 0.3 mm (35 corrugation) case.

The zero offset beam parameters of all three ALMA horn models are presented in Figs. 5.18, 5.19 and 5.20. The original 84 corrugation model is plotted in blue and the 35 corrugation model developed to reduce section number is plotted in red. Finally the new 30 corrugation model to comply with material requirements is plotted in green. The cross polarisation stays reasonably low (>-20 dB) across the whole waveband for all three horns. The horns with a lower number of corrugations actually function slightly better than the original at high frequencies. Return loss however, is much lower for the original horn, staying under -20 dB for the whole band, and under -30 dB for most of it. The 35 corrugation model stays under -20 dB return loss for most of the band, rising slightly above at the upper edge. Finally, the 30 corrugation model reaches -10 dB at higher frequencies, and also performs slightly worse at low frequencies. The effect of changing the corrugation thickness by the breadth of a human hair is surprisingly stark. A FWHM plot is also included, showing the 35 and 30 corrugation horns with almost identical beamwidths, as expected given their identical mouth diameter and flare angle. The original horn has a narrower beamwidth, as it is much more gently flared, with a slightly wider mouth diameter.

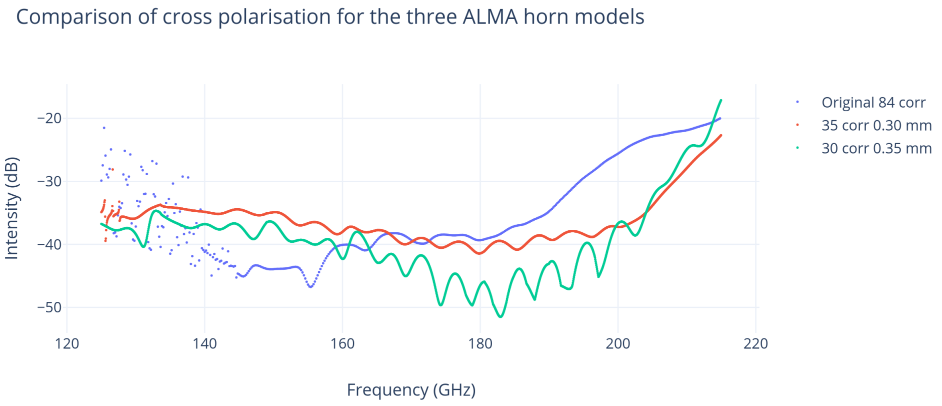

FIGURE 5.18: Cross polarisation as a function of frequency for the three ALMA horn models.

The cross polarisation is slightly better on the 0.35 mm horn in the centre of the waveband, however below the -30 dB level this is inconsequential. It then rises above -20 dB at approximately 210 GHz. As the edge of the band is 211-215 GHz, this is not ideal but not of great concern. The return loss however, is higher across the band for this horn. In particular, it is significantly higher for frequencies above 180 GHz. At the edge of the band it reaches -10 dB, while for

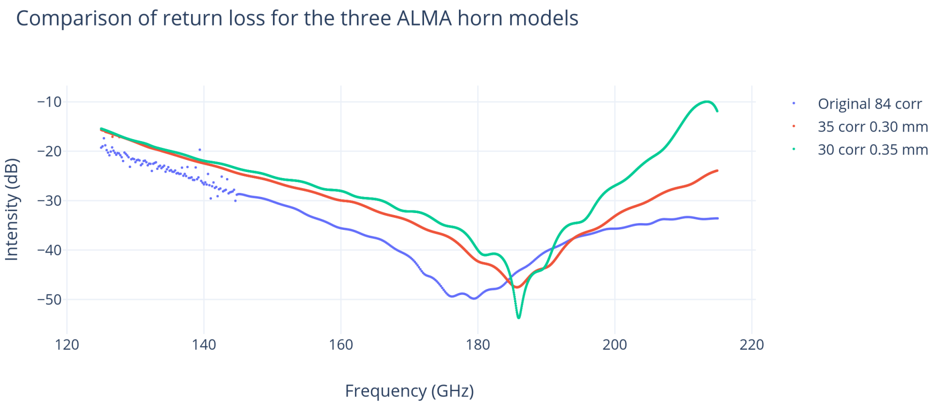

FIGURE 5.19: Return loss as a function of frequency for the three ALMA horn models.

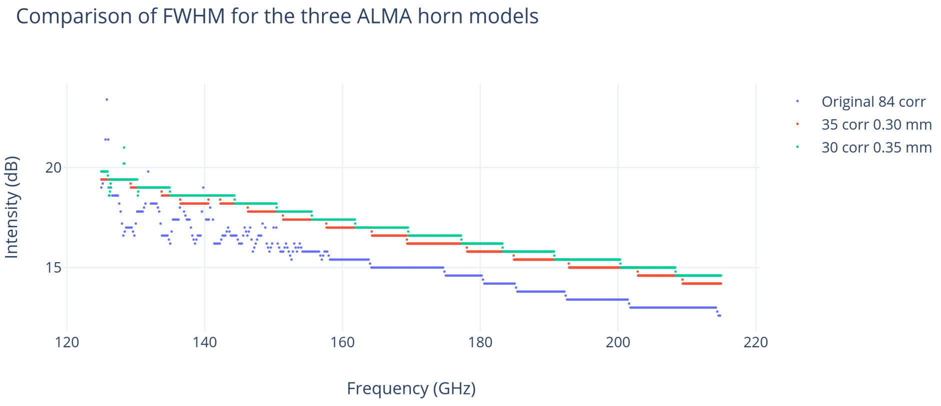

FIGURE 5.20: FWHM as a function of frequency for the three ALMA horn models.

the original it horn peaks at -24 dB. This represents a factor of 25 times more power lost to the S11 at 210-215 GHz due to the increase in platelet width.

One final consideration for laser cutting techniques is that the cutting beam is a laser, of presumably optical or near UV frequency, which is emitted as a Gaussian beam from a very small aperture (to improve accuracy and power efficiency while minimising loss of substrate). This beam is designed to reach a narrow Gaussian waist at the point of entry into the substrate to be cut, as shown in Fig. 5.21. For Gaussian beams, as discussed in Chapter 2, it follows that a smaller waist creates more divergent beams for a given wavelength (Eqn. 2.11). The divergence of the laser as it passes its waist location and moves into the aluminium sheet would thus be expected to impart a small angle to the cut edge of the metal, cutting a narrower ring at the point of entry than the point of exit by several microns. However, modelling this effect in PyScatter would be difficult given that approximating slopes requires the inclusion of a large number of incremental steps for each corrugation section, multiplying the computation times. As such, this error is neglected in simulation, but could be a small source of divergence from predictions when the real horn performance is compared with the simulated case.

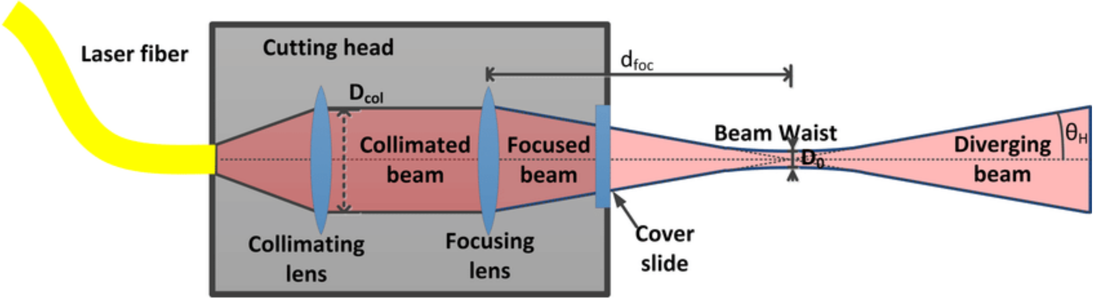

FIGURE 5.21: Cutaway schematic of the internal structure of a laser cutting head, showing real components alongside optical parameters (Willumson, 2016).

5.3.4 Final tolerance analysis

The parameters for machining specified by the laser micromachining firm are given in Tab. 5.3. The first three sources of uncertainty listed in the table were used to construct a final, highly representative set of horn models for a tolerance analysis. The conductive sheet thickness and milling depth were assumed to be uncorrelated sources of uncertainty, and therefore summed in quadrature to yield a total uncertainty of ±72 μm. As stated previously, beam spread is not a random error and is also not easily computed with PyScatter. Furthermore, its effect in this case is of the order of $350\sin(4^\circ) = 25$ μm, 4° being a reasonable upper bound for the angle incurred by the beam spread, and 350 μm being the section width. This is smaller than the 50 μm cutting radius error. These errors are larger than was initially expected for the laser technique, and are likely to be comparable to, or even exceed, the tolerance on the electroformed section. As such, the final error simulations were conducted for the entire horn, without splitting the tolerance level to account for the different techniques. The section widths were varied to correspond to corrugation length uncertainty, and the section radii varied for corrugation radius uncertainty. All section errors were selected from uniform distributions, with limits at the aforementioned tolerance levels.

TABLE 5.3: Manufacturing tolerance specifications.

Nature of uncertainty	Value	Measurement affected
Sheet thickness	$\pm 70\mu$m	Corrugation length
Milling depth	15 μm	Corrugation length
Milling radius	50 μm	Corrugation depth
Beam spread	$\approx 2-4^\circ$	Corrugation depth

The beam parameter results are shown in Figs. 5.22 and 5.23. Return loss is not too badly affected by the machining tolerance, with the mean following the nominal horn trace for most of the plot. However, the deep trough at 185 GHz is notably absent from the return loss plot. One potential explanation for this is that the randomisation of the tolerance disrupted destructive interference which had been suppressing returning radiation at these frequencies. Cross-polarisation suffers significantly by contrast, with increases of up to 10 dB, although the levels still fall mostly below -25 dB.

5.4 Ka band horn design

A horn was also designed for the Ka band region, 26.5-40 GHz, as mentioned earlier. This design was not advanced as quickly as the band 4-5 design, as the machining of the band 4-5 design was to take precedent. The horn was designed in the same way as the ALMA band 4-5 horn described previously. A flare angle of 7.5 degrees, an aperture diameter of λ_{central} (56-57 mm for the Ka band), and an input waveguide diameter of 1.2 times the theoretical cutoff for the largest wavelength of the band (7.96 mm for Ka band) were again used. Corrugation widths of 2 mm were chosen. The profile of the horn designed is shown in Fig. 5.24, and the beam at the central frequency in Fig. 5.25. The Ka band horn is approximately five times bigger in all dimensions than an ALMA band 4-5 horn. As such it would be much easier to machine than the higher frequency design, and machining errors on it would be a substantially smaller fraction of λ. For this reason, no tolerance analysis was conducted on this horn. The FWHM of the Ka horn is the same as that for the original band 4-5 design. The cross polarisation and return loss are shown in Fig. 5.26 and Fig. 5.27 respectively. In these plots the performance is compared with a later design which had 61 corrugations rather than 84. It is hoped that the Ka band horn design will be manufactured and tested in Manchester later this year.

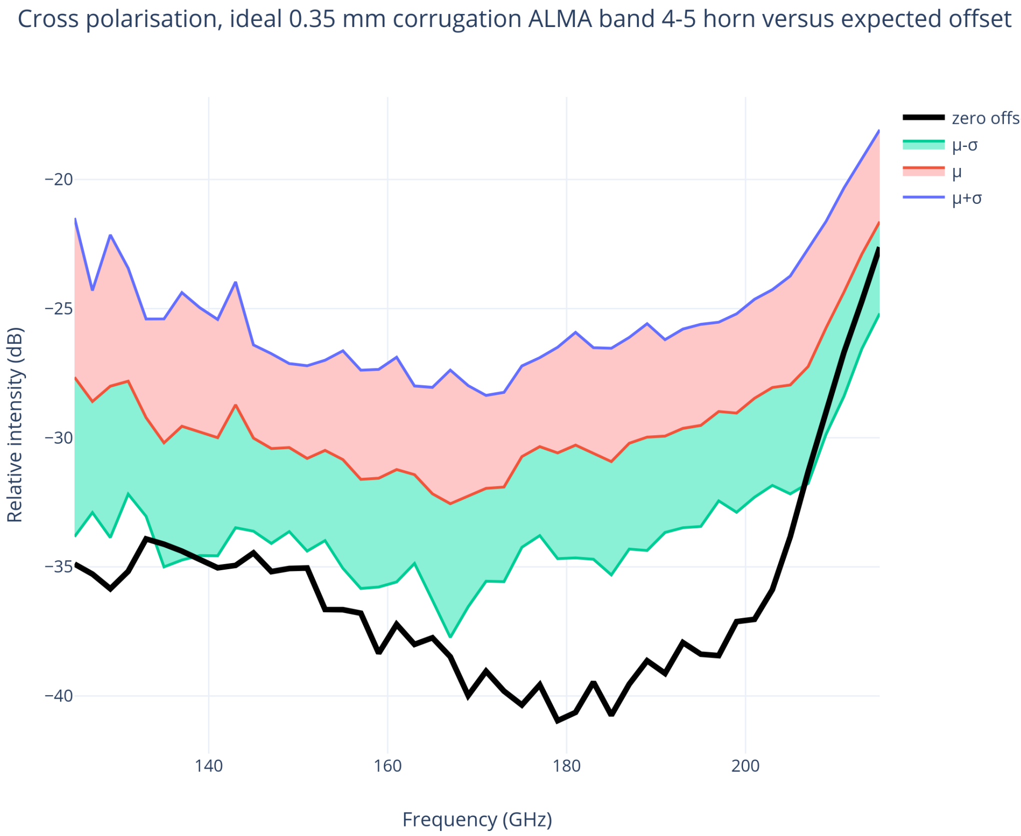

FIGURE 5.22: Mean and standard deviation of realised cross-polarisation as a function of frequency for 20 0.35-mm section horns, including errors of the final tolerancing levels. The nominal 0.35-mm section ALMA horn is included as the solid black trace.

5.5 Final summary

Corrugated horns were designed for two wavebands, ALMA band 4-5, and later the Ka band as a scaled test horn. The initial horn designs were modified several times to meet manufacturing criteria. At each step, errors were introduced into the models to simulate the inaccuracies of the machining techniques and materials used. This showed how the theoretical best design is impacted by physical considerations.

To illustrate this, the final beam parameters in Fig 5.22 and Fig 5.23 may be compared with the initial results in Fig. 5.4 and 5.5. This yields the total change in performance due to the multiple stages of manufacturing constraints. This change was shown to be very substantial, with >10 dB increases in both cross-polarisation and return loss across most of the band.

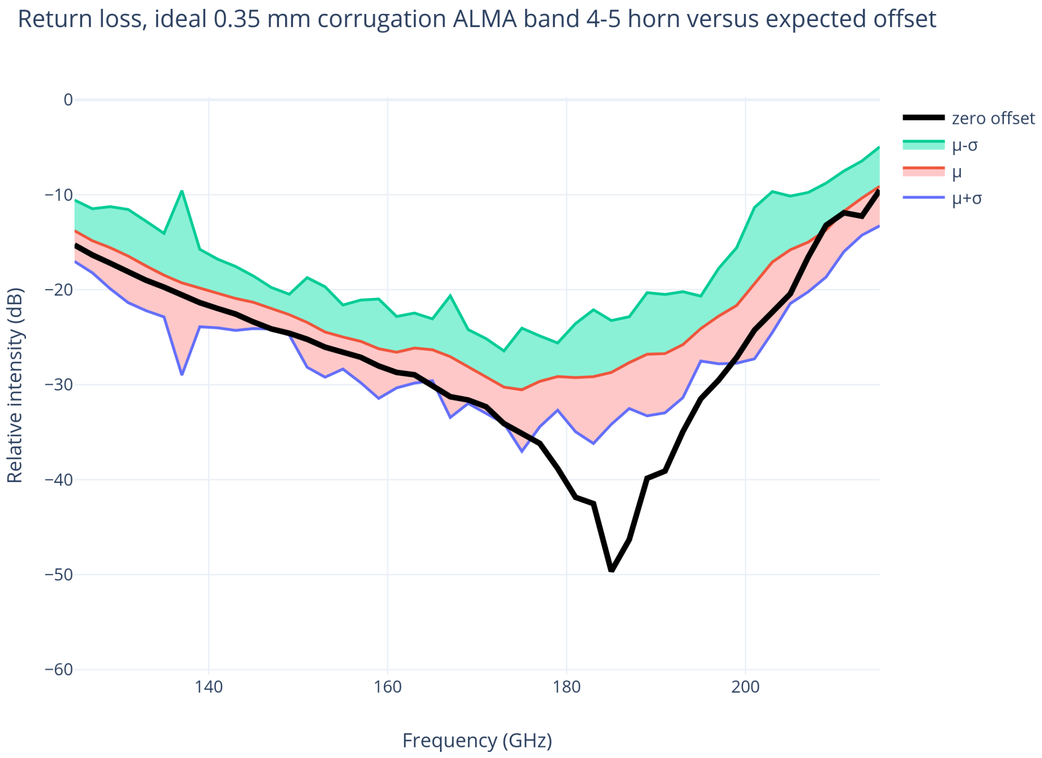

FIGURE 5.23: Mean and standard deviation of realised return loss as a function of frequency for 20 0.35-mm section horns, including errors of the final tolerancing levels. The nominal 0.35-mm section ALMA horn is included as the solid black trace.

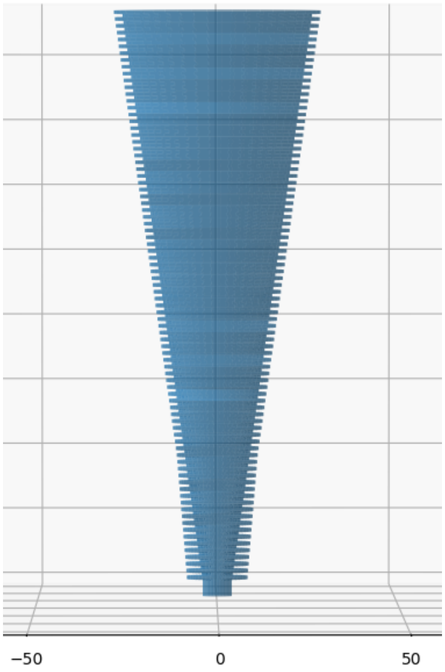

FIGURE 5.24: Ka band horn design plotted using 3D horn plotter, units in mm.

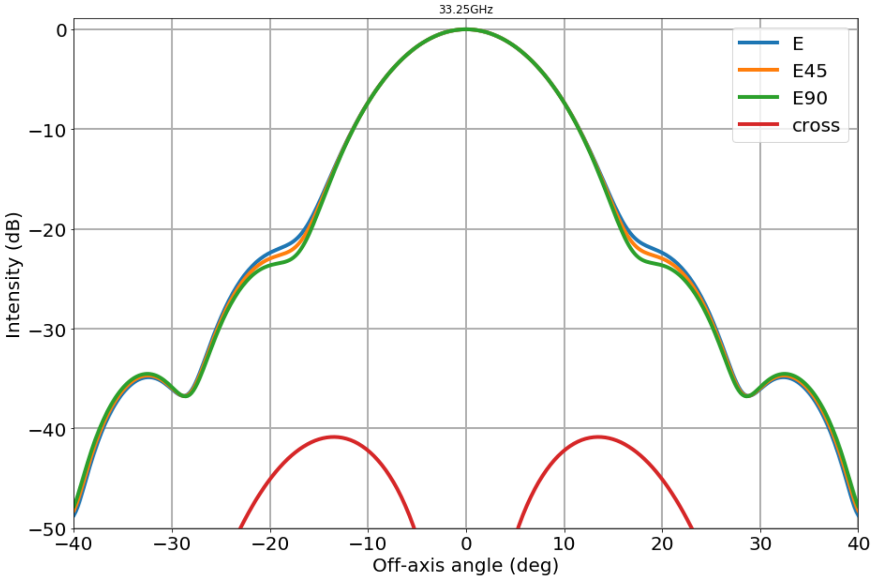

FIGURE 5.25: Central frequency beam plot of Ka band horn, showing very low cross polarisation and a low FWHM, with a relatively high shoulder, but low sidelobes.

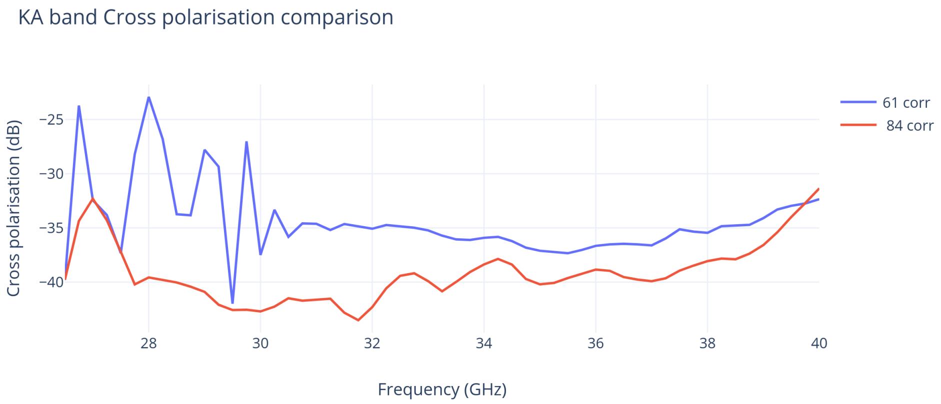

FIGURE 5.26: Comparison of cross polarisation between the 84 corrugation Ka band horn design and a lower corrugation alternative horn.

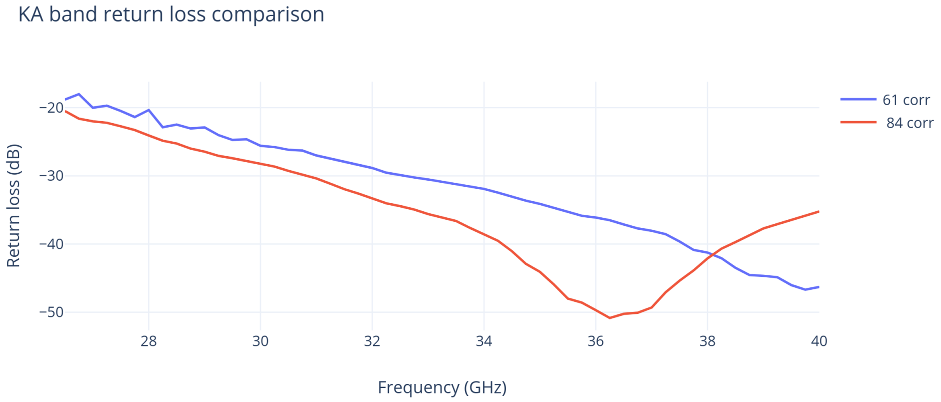

FIGURE 5.27: Comparison of return loss between the 84 corrugation Ka band horn design and a lower corrugation alternative horn.

Chapter 6

Numerical mode matching

6.1 Background and Introduction

The goal of the research presented in this chapter was to develop in-house numerical electromagnetic mode matching software for modelling non-ideal corrugated waveguides and horns. Numerical methods are often much more versatile than analytical methods, at the cost of greater computational intensity. This is of great importance for microwave modelling, as analytical models of the behaviour of electromagnetic radiation exist only for very simple and mathematically perfect components. The ensuing limitations confine current analytical routines to the study of perfectly aligned components, which is physically unreasonable for some realistic manufacturing methods, such as the simultaneous production of a horn array by platelet milling and alignment. The NumCross code developed here was extended from existing mode matching software (PyScatter) developed by Kalinauskaite (2018) and Burke (2021), which used analytical solutions for overlap integrals. When these were replaced with equivalent numerical integrals, a code could be developed to model corrugations which are offset from each other.

When manufacturing horns, there are two broad approaches for the machining procedure. Firstly, components can be machined individually; this can employ a variety of industrial techniques. Typical methods use electrodeposition to coat a mandrill (3D negative image) of the horn with conductive material, and then etch away the mandrill using a corrosive agent. The other general method of horn production is batch manufacture. Arrays of holes are cut into conductive sheets of carefully controlled width (typically equal to one half or one corrugation) using CNC milling or laser micromachining. The sheets are then stacked on top of one another to yield an array of identical horns in their final geometric configuration, embedded in the resultant block of conductive material. The array is typically held in place by mechanical force from the fastenings alone, as adhesive thickness and uniformity would be difficult to control. An example of one such array is shown as Fig. 6.1.

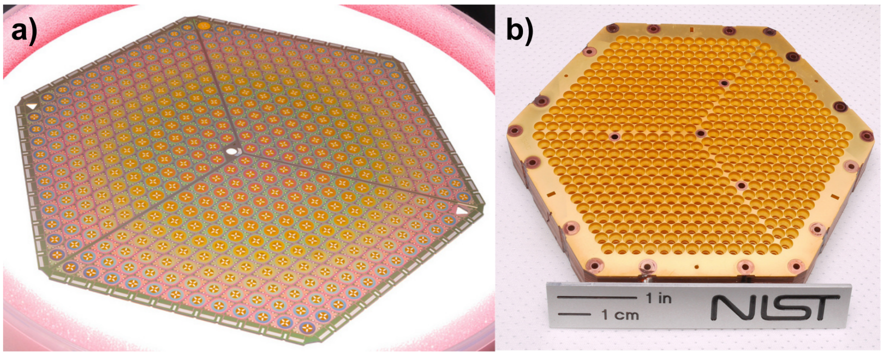

FIGURE 6.1: Micromachined Si platelet array of horns (NIST, 2008)

Batch processes are much more economical for large arrays of horns, but lack the inherent cylindrical symmetry of single horn techniques. Additionally, they require high precision overlaying of the individual sheets of conductor to ensure correct relative positioning of corrugation sections. This tends to incur large decentered lateral errors, as opposed to the radially symmetric errors which would be seen for individually fabricated components. By modelling the effect of small offsets in the waveguide steps, one can examine the impact of different sheet alignment tolerances on the optical performance of the horn. Computation of radially symmetric errors (e.g. incorrect radii, ridges or slots left by milling etc.) is simple analytically; it can be performed by random variation of the individual section radii composing the horn, as was performed for the ALMA project in Chapter 5. Conversely, introduction of lateral offsets is impossible analytically, as it breaks the cylindrical symmetry of the horns, making the integrals impractically difficult or impossible to solve. However this task is relatively simple numerically, comprising a relative shift of the horn sections on a pre-defined Cartesian integration grid, which is overlaid on the disk representing the internal cavity of a given section.

6.1.1 Power coupling in PyScatter

In Chapter 4, the method of mode matching for electromagnetics was introduced. This calculates power transfer by coupling modes using analytically solved overlap integrals of the form shown in Eqn 6.1, with the nth mode on the inner section coupling to the mth mode on the outer section

$$\int \bar{E}_{n,inner} \times \bar{H}^*_{m,outer} \cdot dA. \tag{6.1}$$

It may be shown (Kalinauskaite, 2018) that if the transverse electric field is continuous at a junction, then the power transfer across the junction may be represented in matrix form, using the [A] [B] [C] [D] mode coefficient vectors discussed earlier, as

$$[P][[A]+[B]] = [Q][[C]+[D]]. \tag{6.2}$$

The matrix elements of P and Q are defined by Eqns. 6.3 and 6.4, respectively, where use is made of the fact that the parallel electric field is zero at the conducting wall of the larger guide at the step.

$$P_{mn} = \int\limits_{a_{inner}} \bar{E}_{n_{inner}} \times \bar{H}^*_{m_{outer}} \cdot dA \tag{6.3}$$

$$Q_{mn} = \left(\int\limits_{a_{outer}} \bar{E}_{n_{outer}} \times \bar{H}^*_{m_{outer}} \cdot dA \right) \delta_{nm}. \tag{6.4}$$

a_{inner} and a_{outer} are the cross sectional areas of the inner and outer corrugation sections. Similarly, the continuity of the magnetic fields at the junction yields Eqn. 6.5, where $[R]$ is defined by Eqn. 6.6.

$$[R] = [[A]-[B]] = [P]^T[[D]-[C]] \tag{6.5}$$

$$R_{mn} = \left(\int\limits_{a_{inner}} \bar{E}_{n_{inner}} \times \bar{H}^*_{m_{inner}} \cdot dA \right) \delta_{nm}. \tag{6.6}$$

The terms making up the P, Q and R matrices are computed analytically in the PyScatter routine. The routine outlined in the following sections of this chapter computes these matrix values numerically in order to allow for an offset between the corrugation sections to be modelled. This section of each code is included as Appendix B for PyScatter and Appendix C for NumCross.

6.1.2 Modes

When passing radiation through a cylindrical waveguide, a source transmits power in a variety of transverse electric and magnetic modes. These modes are subject to the boundary condition imposed by the walls of the waveguide, namely that the electric field at the wall must be zero. Thus, in free space, an infinite number of modes are present, and the number which can propagate decreases with confinement of the wave. In essence, this represents a cylindrical analogue of a standing wave, prevalent throughout physics from fluid dynamics to the quantum world. Integral to the description of the transverse modes in cylindrical cavities are the Bessel functions, a series of periodic trancendental functions. These were refined in the 1820s by Friedrich Bessel, based on earlier work by many renowned classical mathematicians and physicists (Dutka, 1995). Of particular relevance are cylindrical Bessel functions of the first kind. These are cylindrically symmetrical decaying waveforms which constitute the solution set of Eqn. 6.7.

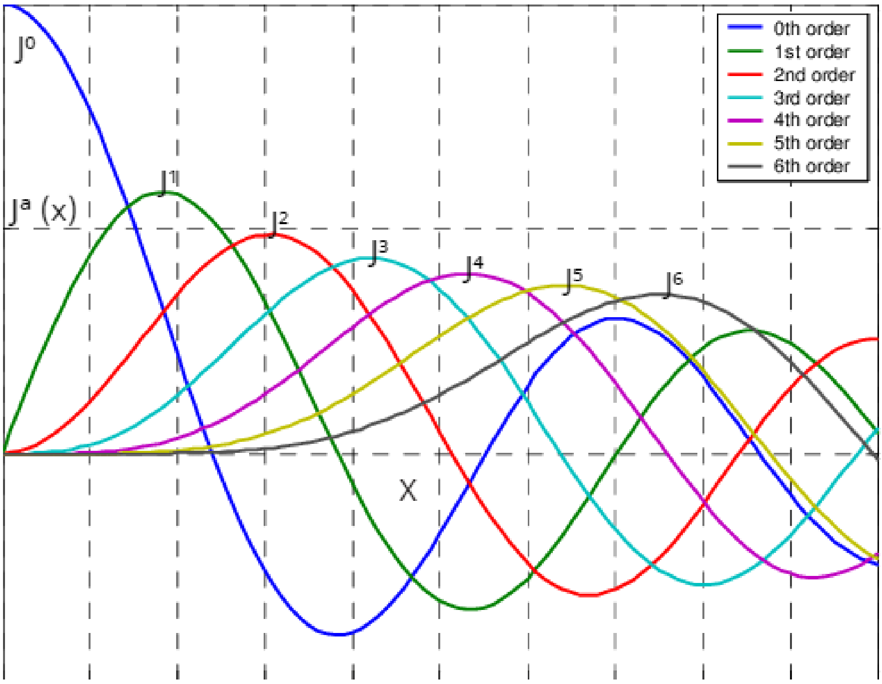

FIGURE 6.2: Profile of Bessel functions of the first kind, of varying order (Tan, C. et al.F 2002).

$$x^2\frac{d^2y}{dx^2} + x\frac{dy}{dx} + \left(x^2 - a^2\right) y = 0 \tag{6.7}$$

The a term in this equation refers to the order of the function. Higher orders describe progressively longer, lower amplitude waveforms. The dependence of these functions on the order is illustrated by Fig 6.2.

The equations to describe the transverse components of the fundamental transverse electric (TE) and transverse magnetic (TM) modes of a cylindrical cavity in Cartesian coordinates are as follows (Kalinauskaite, 2018).

For TE modes

$$e_x^{TE} = -\sqrt{\frac{(2-\delta_{n0})}{4\pi a^2\left(1-\left(\frac{n}{p'_{nm}}\right)^2\right)J_n^2(p'_{nm})}}\times$$
$$\left(J_{n-1}\left(p'_{nm}\frac{r}{a}\right)\begin{pmatrix}\cos((n-1)\phi)\\ -\sin((n-1)\phi)\end{pmatrix}+J_{n+1}\left(p'_{nm}\frac{r}{a}\right)\begin{pmatrix}\cos((n-1)\phi)\\ -\sin((n-1)\phi)\end{pmatrix}\right) \tag{6.8}$$

$$e_y^{TE} = -\sqrt{\frac{(2-\delta_{n0})}{4\pi a^2\left(1-\left(\frac{n}{p'_{nm}}\right)^2\right)J_n^2(p'_{nm})}}\times$$
$$\left(J_{n-1}\left(p'_{nm}\frac{r}{a}\right)\begin{pmatrix}\sin((n-1)\phi)\\ \cos((n-1)\phi)\end{pmatrix}-J_{n+1}\left(p'_{nm}\frac{r}{a}\right)\begin{pmatrix}\sin((n+1)\phi)\\ \cos((n+1)\phi)\end{pmatrix}\right) \tag{6.9}$$

$$h_x^{TE} = \sqrt{\frac{(2-\delta_{n0})}{4Z_{TEnm}^2\pi a^2\left(1-\left(\frac{n}{p'_{nm}}\right)^2\right)J_n^2(p'_{nm})}}\times$$
$$\left(J_{n-1}\left(p'_{nm}\frac{r}{a}\right)\begin{pmatrix}\sin((n-1))\phi\\ \cos((n-1)\phi)\end{pmatrix}-J_{n+1}\left(p'_{nm}\frac{r}{a}\right)\begin{pmatrix}\sin((n+1)\phi)\\ \cos((n+1)\phi)\end{pmatrix}\right) \tag{6.10}$$

$$h_y^{TE} = \sqrt{\frac{(2-\delta_{n0})}{4Z_{TEnm}^2\pi a^2\left(1-\left(\frac{n}{p'_{nm}}\right)^2\right)J_n^2(p'_{nm})}}\times$$
$$\left(J_{n-1}\left(p'_{nm}\frac{r}{a}\right)\begin{pmatrix}\cos((n-1)\phi)\\ -\sin((n-1)\phi)\end{pmatrix}+J_{n+1}\left(p'_{nm}\frac{r}{a}\right)\begin{pmatrix}\cos((n+1)\phi)\\ -\sin((n+1)\phi)\end{pmatrix}\right) \tag{6.11}$$

For TM modes

$$e_x^{TM} = \sqrt{\frac{(2-\delta_{n0})}{4\pi a^2 J_{n+1}^2(p_{nm})}} \times \left(J_{n-1}\left(p_{nm}\frac{r}{a}\right) \begin{pmatrix} \cos((n-1)\phi) \\ -\sin((n-1)\phi) \end{pmatrix} - J_{n+1}\left(p_{nm}\frac{r}{a}\right) \begin{pmatrix} \cos((n+1)\phi) \\ -\sin((n+1)\phi) \end{pmatrix} \right) \tag{6.12}$$

$$e_y^{TM} = -\sqrt{\frac{(2-\delta_{n0})}{4\pi a^2 J_{n+1}^2(p_{nm})}} \times \left(J_{n-1}\left(p_{nm}\frac{r}{a}\right) \begin{pmatrix} \sin((n-1)\phi) \\ \cos((n-1)\phi) \end{pmatrix} + J_{n+1}\left(p_{nm}\frac{r}{a}\right) \begin{pmatrix} \sin((n+1)\phi) \\ \cos((n+1)\phi) \end{pmatrix} \right) \tag{6.13}$$

$$h_x^{TM} = \sqrt{\frac{(2-\delta_{n0})}{4Z_{TM_{n-1}}^2 \pi a^2 J_{n+1}^2\left(p_{nm}\right)}} \times \left(J_{n-1}\left(p_{nm}\frac{r}{a}\right) \begin{pmatrix} \sin((n-1)\phi) \\ \cos((n-1)\phi) \end{pmatrix} + J_{n+1}\left(p_{nm}\frac{r}{a}\right) \begin{pmatrix} \sin((n+1)\phi) \\ \cos((n+1)\phi) \end{pmatrix} \right) \tag{6.14}$$

$$h_y^{TM} = \sqrt{\frac{(2-\delta_{n0})}{4Z_{TM_{n-1}}^2 \pi a^2 J_{n+1}^2\left(p_{nm}\right)}} \times \left(J_{n-1}\left(p_{nm}\frac{r}{a}\right) \begin{pmatrix} \cos((n-1)\phi) \\ -\sin((n-1)\phi) \end{pmatrix} - J_{n+1}\left(p_{nm}\frac{r}{a}\right) \begin{pmatrix} \cos((n+1)\phi) \\ -\sin((n+1)\phi) \end{pmatrix} \right) \tag{6.15}$$

The terms used in Eqns. 6.8 - 6.15 are defined as follows. r represents an arbitrary distance along the radius a of a cylindrical waveguide. J_n is a Bessel function of the first kind, of order n, and J'_n its first derivative. p_{nm} denotes the mth zero of that n_{th} order Bessel function, while p'_{nm} represents the mth zero of the first derivative of that function. The J'_ns are used to calculate the TE fields, while the J_ns calculate the TM.

The oscillatory character of Bessel functions is such that m and n can each assume any value $\in \mathbb{N}$, additionally, n may be zero. δ_{n0} is a delta function taking a value of unity when n=0, and having zero value elsewhere. Finally, the matrix notated trigonometric functions calculate the pair of orthogonal electromagnetic fields for each (m,n) mode combination.

6.2 Development of the numerical PyScatter code (NumCross)

6.2.1 Generating and plotting transverse modes.

The values for p_{nm} and p'_{nm} are found using the scipy package for Python, more specifically the routine scipy.special.jn_zeroes and scipy.special.jnp_zeroes, respectively. jnzeroes(n,m) computes m roots of the nth order Bessel function of the first kind, while jnpzeroes(n,m) computes m roots of the first derivative of the same function. By selecting just the m-1^{th} element of the output array in each case, the desired root could be returned.

An impedance factor (Z^{TE},Z^{TM}) was computed for both the electric and magnetic fields, using the p_{nm} and p'_{nm} results. This factor determines the effect of the size of the waveguide on the propagation of the wave. The equations for the electric and magnetic impedances are given by Equation 6.16 and 6.17.

$$Z_{TE} = Z_0 \left(\sqrt{1.0 - \frac{p'_{nm}(n,m)}{(\omega a \sqrt{\mu_0 \epsilon_0})}^2} \right)^{-1} \tag{6.16}$$

$$Z_{TM} = Z_0 \sqrt{1.0 - \frac{p_{nm}(n,m)}{(\omega a \sqrt{\mu_0 \epsilon_0})^2}} \tag{6.17}$$

Z_0 represents the impedance of free space, 377 Ω. However, for simplicity of analysis, this can be normalised to 1, as the beam power is computed as a relative rather than an absolute value. This is sufficient when the beam parameters compare boresight intensity with other measured values, return loss, cross-polarisation etc. If the waveguide is large compared to the wavelength, Z approaches unity, and has no effect, whereas if the waveguide is on the order of the wavelength, Z is of critical importance in determining the power transmitted in the cavity. Depending on the value of the relevant Bessel or Bessel derivative root, Z may take real or imaginary values. Imaginary values represent evanescent power dissipated in the system, meaning that the associated mode is non-propagating at the given waveguide radius. The point at which Z becomes imaginary may be predicted from Eqn. 4.4, as discussed in Chapter 4.

The equations for the fields were then calculated across the physical area of a waveguide. Initially, r and ϕ coordinates were used on a radial grid. However, this was later converted to Cartesian coordinates for ease of handling offsets. The ax.scatter3D function was used to create plots of each mode, with high power showing as yellow-white, and low power as black-red. TE modes are observed to fall off to zero at the waveguide edge, whereas TM modes reach a maximum value at the waveguide edge.

To integrate the total power across the mode, the cross product was taken of the E and H fields at each point on the Cartesian integration grid. This was summed across the grid, including only those points which fell within the circular cross section of the waveguide. The total was then multiplied by the specific dx and dy used. This gave the average Poynting value over the cross-section. To express the variables in the field equations in Cartesian coordinates, $\sqrt{x^2 + y^2}$ was substituted for r, and the two-argument arctangent of y/x for ϕ.

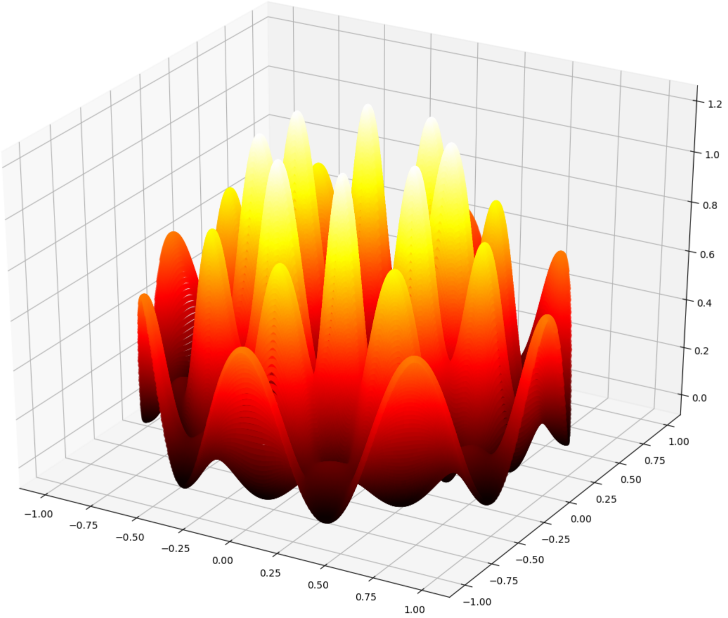

FIGURE 6.3: TM mode plot for radial order 2 and azimuthal order 4.

Fig. 6.3 and Fig. 6.4 show the profile of typical TM and TE modes as plotted using Python code. To preserve the generality of the result, the simulation was set such that $\lambda \ll r$. A higher order m corresponds to more Bessel zeroes, and thus more complete oscillations across the waveguide. Higher order n increases the order of the Bessel function, this introduces further oscillations

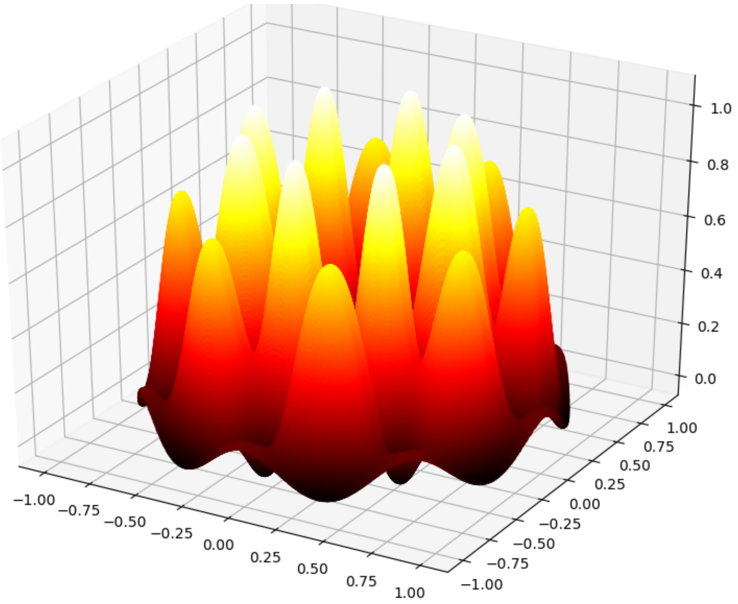

FIGURE 6.4: TE mode plot for radial order 4 and azimuthal order 2.

along the ϕ direction, the angular character. It is also observed that, as n increases, the central pattern broadens, and the outer radial oscillations compress toward the boundary of the waveguide. In general, for order (n,m), a TE mode will exhibit m radial crests divided into $2n$ angular peaks, whereas a TM mode will possess an extra half crest at the outer edge, to satisfy its boundary conditions.

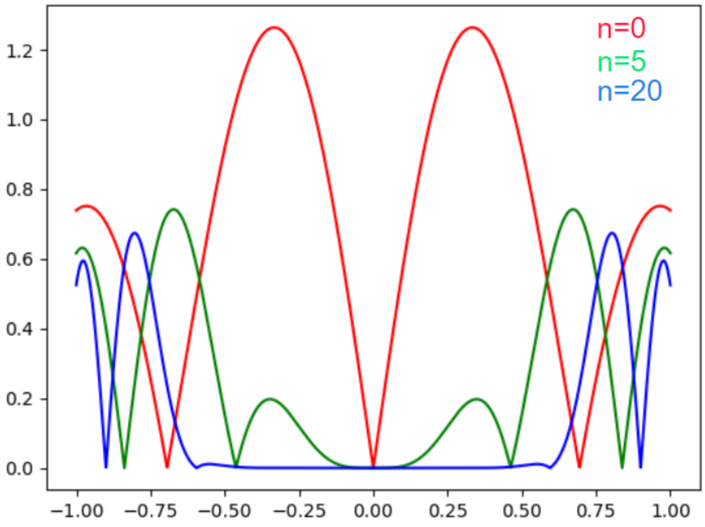

FIGURE 6.5: Superimposed TM mode cuts showing effects of changing n with constant m.

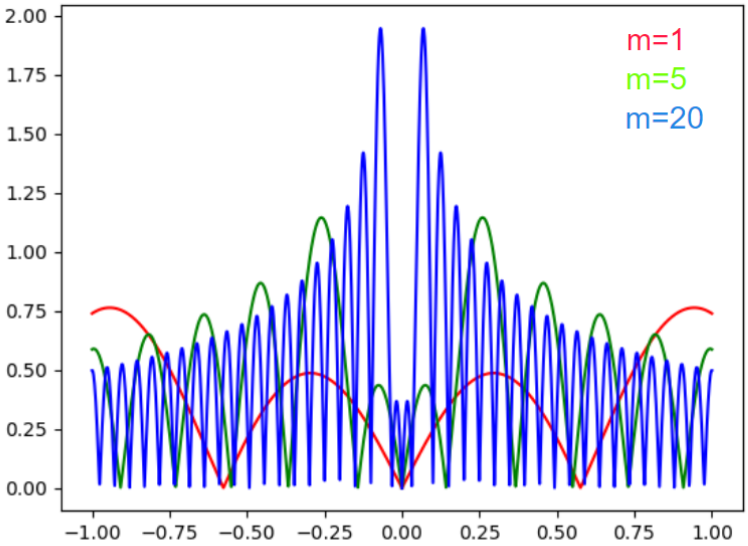

FIGURE 6.6: Superimposed TM mode cuts showing effects of changing m with constant n.

To show the distinct effects of the order n and root number m on the pattern, a set of cuts was computed and superimposed. m was kept fixed at 2 across the set, and n varied. The process was then repeated for fixed n=2 and variable m. These plots are shown as Fig. 6.5 and Fig. 6.6, respectively. All cuts were taken from the TE mode at $\phi = 0$, to ensure continuity and illustrate the general radial dependence of the power across the waveguide.

The increase in angular mode number reduces power in the centre. For the increasing radial modes however, higher m modes yield progressively sharper peaks. In the extreme case of a light pipe, $D \gg \lambda$, the walls would effectively impose no restriction on the available modes within the cavity.

A final plot was prepared to examine the change of the wave profile across the waveguide as m increased further. For high m, the profile envelope described by the peaks becomes very apparent. This profile is a good approximation for the radial distribution of power across a relatively large cavity. This profile is shown in Fig. 6.7. For simplicity, n is kept at 0. It is clear that as m increases, the power is concentrated further into the narrow peaks near the propagation axis. This observation will be revisited upon studying horn performance, as the ratio of diameter to wavelength is crucial in determining beam gain or directionality. As in the case of GRASP, cuts provide a more precise comparison tool, whereas 2D grid plots allow for easier visualization and understanding of the plot. However, it is also illustrated that some features are difficult to represent with a 2D slice.

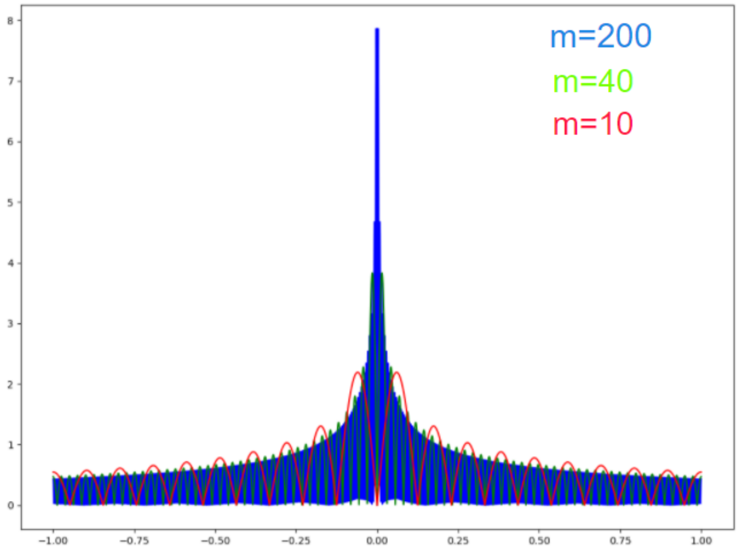

FIGURE 6.7: Change of wave peak profile with changing m for high values of m.

The Poynting sum across the waveguide for each mode is normalized to unity by the choice of the impedance as unity at the outset, thus all power in the modes should accordingly sum to unity. By printing the calculated Poynting sum, it was possible to check that the modes were correctly computed across the plots. Additionally, the deviation of these values from unity gave an approximation of the level of numerical error incurred at a given computational resolution, and thus the sensitivity of the simulation accuracy to an increase or decrease in resolution.

6.2.2 Generating a P matrix by numerical mode integration

Inside a smooth-walled waveguide of constant radius, modes propagate without transferring power between one another (no scattering). This breaks down when the radius changes within the guide. When a radial step occurs within a waveguide, each mode within the cavity scatters power to other modes, the amount of which is determined by the fractional size and offset of the step, and the wavelength of the radiation. If the waveguide recieving radiation across the step is very narrow relative to the incident wavelength, the wave may not propagate across the step. This is known as a full mode cutoff, and power will be reflected and scattered to purely evanescent modes at the boundary. Mathematically, this is represented as a complex valued Poynting vector in the guide experiencing the cutoff.

The exact intermodal scattering coefficients may be determined analytically using a cross coupling integration. This is the fundamental technique behind the PyScatter mode matching process used to design horns previously. The general mathematical expression for the overlap integral, e.g. the integral to calculate P_{mn} in Eq. 6.3, is replaced by a sum across the overlapping area.

$$P_{mn} = \sum_{i,j} \bar{E}_{n_{inner}}(i,j) \times \bar{H}^{*}_{m_{outer}}(i,j)dxdy. \tag{6.18}$$

P_{mn} refers to an element of the P matrix denoting the transfer of power from mode n to mode m, $\bar{E}(i,j)$ and $\bar{H}(i,j)$ are the electric and magnetic fields evaluated at a point (i,j) on the Cartesian grid and dx and dy are the grid spacings. As before, *inner* refers to the origin mode, and *outer* the destination mode.

Once calculated, the power scattering between all modes is stored as a square array of values. Each set of mode numbers has a corresponding TE and TM mode, which in turn each have co- and cross-polar modes. As such, the square array for N sets of mode numbers will have $(4N)^2$ entries. To organise these, all excited modes are entered once as labels on each axis of an array, and the amount of scattering from mode combination A to mode combination B is given as the unique value at the intersection of the row corresponding to the first mode, and the column corresponding to the second, as shown in Table 6.1. Scattering between modes must be non commutative in nature to allow for power transfer between modes. Were it commutative, the total power transferred between mode pairs would always sum to zero, as the scattering from mode A into B would equal that from mode B into A. The special case of a zero-length step (a smooth waveguide) yields a $(4N)^2$ identity matrix. The self coupling of modes (TE and TM co-polar and cross-polar) in this case, will be visible as unity entries along the main diagonal of the matrix, as shown for a TE11 mode by Gentili, Pelosi and Piccoli (2019). This is expected from the previous assertion that power is not scattered without a step being present. It is important also to note that in the case of a mode not propagating in a given cavity, the value of unity for that self coupling entry will be replaced by the positive or negative imaginary unit, ±i, depending on whether the mode is TE or TM. These imaginary entries denote evanescent mode couplings, resulting from the aforementioned impedance factor becoming complex. This, of course, requires that all equations and matrices in the code be complex compatible; this is denoted by a $cm.$ before the operator in Python.

Table 6.1 shows a P-matrix as output by the code written; it contains the scattering coefficients for the $n = 1$ order. The number preceding ‘te’ or ‘tm’ in the mode label denotes azimuthal order, and the subsequent qualifiers dictate if the mode is electric or magnetic, and whether it is polarised in the two orthogonal orientations. To reduce the matrix size, only m = 1, 2 are shown. The step and offset are both set to zero, so this is a pure propagation matrix. Additionally, the sections are set to have a very large diameter relative to the wavelength, $D > 100\lambda$. The values along the diagonal are very close to unity, while all other values are negligible. This is what would be expected intuitively from this case, as there is no sudden change in radius to scatter radiation from one mode to another, the power is just coupled from each mode to itself. Also of note are the values of the "zeros". These demonstrate the difference between analytical and numerical zeros. The entries on the order of $10^{-4} - 10^{-5}$ are numerical zeros, they depend on the integration accuracy, and tend to arise in the decimal place below the inverse of the resolution (1000 points along x and y in this case). The null values in the table had values of $10^{-18} - 10^{-19}$, which was rounded down for clarity. These are analytical, or "float" zeros. They arise from algebraic cancellation of terms in the scattering equations, and their tiny but non-zero value is a result of Python’s handling of floating point arithmetic. These analytical zeroes are a consequence of the nature of mode symmetry, and do not depend on the system analysed. As such, code sections which always generate them by way of symmetry can be excluded once the routine is debugged fully, to save on computation time.

TABLE 6.1: Example P-matrix for zero step, showing the n=1 mode, with m = 1, 2. As an example, TE2co refers to the first order co polar transverse electric field in that guide.

	TE1co	TE1cross	TE1co	TM1cross	TE2co	TE2cross	TM2co	TM2cross
TE1co	0.99996+0j	0	0.00007+0j	0	0.00001+0j	0	0.00008+0j	0
TE1cross	0	0.99996+0j	0	0.00007+0j	0	0.00001+0j	0	0.00008+0j
TM1co	0.0005+0j	0	0.99991+0j	0	-0.00001+0j	0	-0.00011j	0
TM1cross	0	0.0005+0j	0	0.99991+0j	0	-0.00001+0j	0	-0.00011j
TE2co	0.00002+0j	0	0.00003+0j	0	0.99999+0j	0	-0.00003+0j	0
TE2cross	0	0.00002+0j	0	0.00003+0j	0	0.99999+0j	0	-0.00003+0j
TM2co	-0.00004+0j	0	0.00007+0j	0	-0.00001+0j	0	-0.99991j	0
TM2cross	0	-0.00004+0j	0	0.00007+0j	0	-0.00001+0j	0	-0.99991j

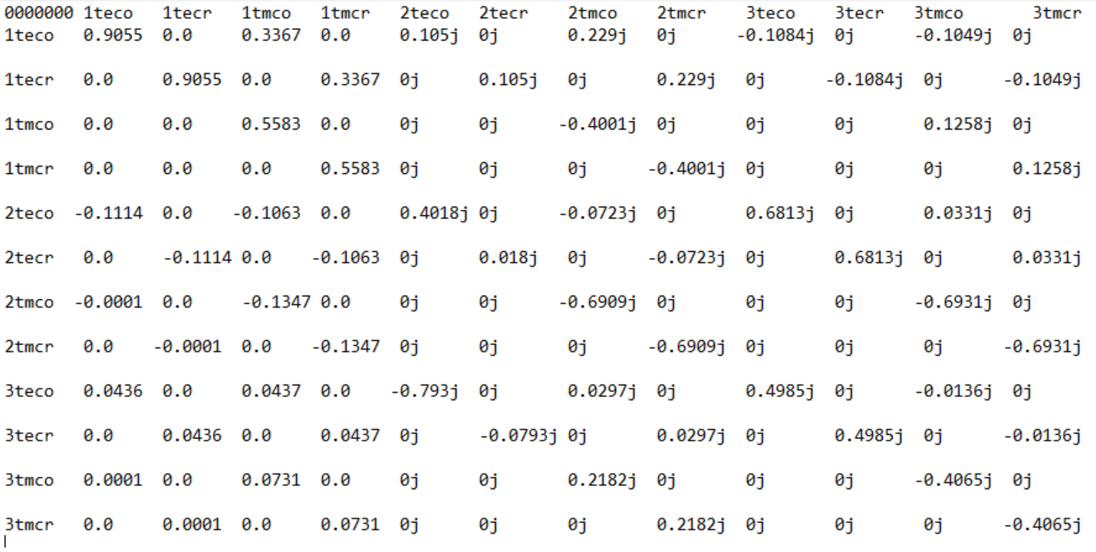

```
0000000 1teco   1tecr   1tmco   1tmcr   2teco   2tecr    2tmco    2tmcr    3teco    3tecr    3tmco      3tmcr
1teco   0.9055  0.0     0.3367  0.0     0.105j  0j       0.229j   0j      -0.1084j  0j      -0.1049j  0j

1tecr   0.0     0.9055  0.0     0.3367  0j      0.105j   0j       0.229j   0j      -0.1084j  0j      -0.1049j

1tmco   0.0     0.0     0.5583  0.0     0j      0j      -0.4001j  0j       0j       0j       0.1258j  0j

1tmcr   0.0     0.0     0.0     0.5583  0j      0j       0j      -0.4001j  0j       0j       0j       0.1258j

2teco  -0.1114  0.0    -0.1063  0.0     0.4018j 0j      -0.0723j  0j       0.6813j  0j       0.0331j  0j

2tecr   0.0    -0.1114 0.0    -0.1063  0j      0.018j   0j      -0.0723j  0j       0.6813j  0j       0.0331j

2tmco  -0.0001  0.0    -0.1347 0.0     0j      0j      -0.6909j  0j       0j       0j      -0.6931j  0j

2tmcr   0.0    -0.0001  0.0    -0.1347  0j      0j       0j      -0.6909j  0j       0j       0j      -0.6931j

3teco   0.0436  0.0     0.0437  0.0    -0.793j  0j       0.0297j  0j       0.4985j  0j      -0.0136j  0j

3tecr   0.0     0.0436  0.0     0.0437  0j     -0.0793j 0j       0.0297j  0j       0.4985j  0j      -0.0136j

3tmco   0.0001  0.0     0.0731  0.0     0j      0j       0.2182j  0j       0j       0j      -0.4065j  0j

3tmcr   0.0     0.0001  0.0     0.0731  0j      0j       0j       0.2182j  0j       0j       0j      -0.4065j
```

FIGURE 6.8: P-matrix for a single radial mode and including three angular modes, exhibiting the effect of a radial step.

6.2.3 Modification to include a step

A step in the waveguide requires a change to the P-matrix code to allow for propagation between waveguide sections of different radii. To accomplish this, one radius was assigned for the electric field on the incident side of the step, and another distinct radius for the magnetic field on the transmitted side. The larger of these radii was used to dictate the size of the Cartesian integration grid, with mesh size determined by the desired numerical resolution. The smaller area was then superimposed onto the larger, aligning the centres to maintain cylindrical symmetry. This is the numerical equivalent of an overlap integral, computing the fields for the overlapping area of two waveguide sections. Changing radii implies different impedance factors for electric and magnetic fields, as Z depends implicitly on the cavity radius. This is intuitive, as a step could be designed such that a given mode reaches cut off as it passes the step to a narrower section of waveguide. Ideally some scattering would be observed from co-polar to co-polar modes and likewise from cross-polar to cross-polar. While cylindrical symmetry is maintained, power will not transfer across polarisations. Additionally, due to the symmetry between x and y axes, the quantity of power in the co-polarised and cross-polarised components modes should remain equal.

Fig. 6.8 shows the P-matrix for a radial step, from 1.0 mm to 1.25 mm, at a

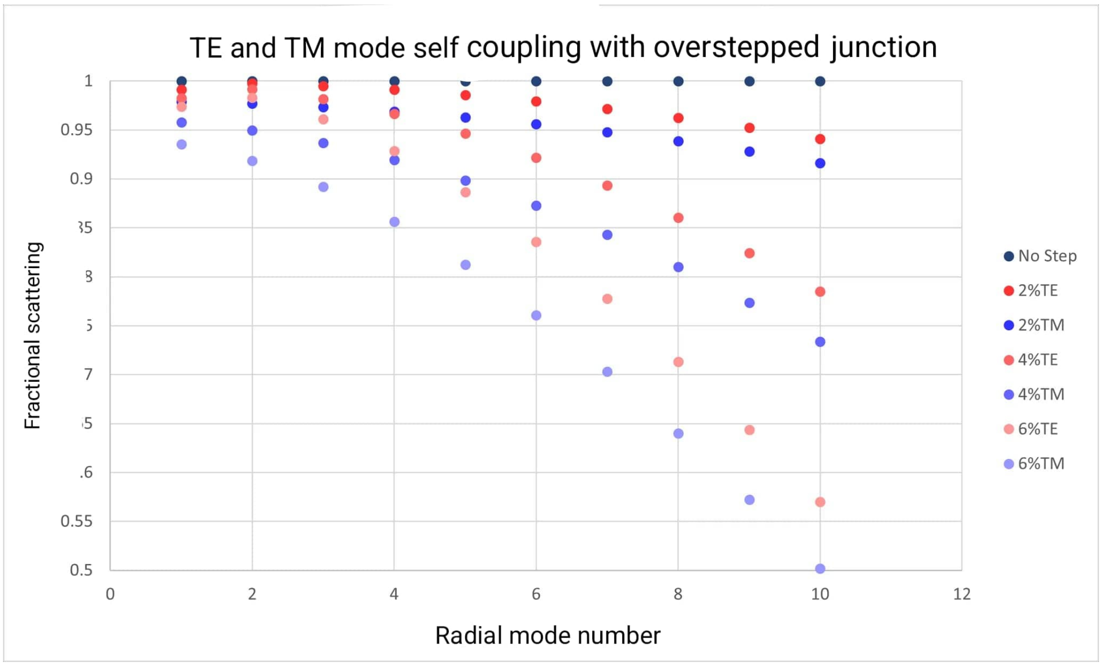

FIGURE 6.9: Effect of 2%, 4% and 6% steps on the self-coupling of n=1 TE and TM modes in a circular waveguide. Propagation across the step is calculated from the smaller to the larger guide.

frequency of 200 GHz. This frequency was chosen to allow the radii to be reasonably close to the fundamental mode cutoff radius at 0.44 mm. This allows us to inspect the handling of both real and imaginary terms. Two thirds of the terms are imaginary in this case, implying that those couplings did not propagate past the step, instead remaining as reactive, evanescent fields. Only couplings of the first angular mode have real values. It is also of note that in both cases, the TM to TE coupling has zero value for all orders, as TM modes do not couple to TE modes when the cylindrical symmetry of the guide is preserved. Mutually orthogonal polarisation combinations are also universally zero, as predicted. Finally, the fraction of power in the main diagonal decreases with increasing mode number. It is also expected from a conservation of energy standpoint, as to conserve the finite electromagnetic energy from the source, any scattering to other modes must result in a decrease of the power propagated in the intramodal terms (the main diagonal of the matrix).

To observe the effect of step size on scattering in the horn, the principal diagonals of P-matrices for various step sizes were plotted as a waterfall plot. The results are shown in Fig 6.9. The waveguide was set to be very large compared to the incident wavelength, to eliminate the effects of the impedance factor on results (the magnitude of which depends on the ratio of waveguide diameter to λ). All samples were run for 10 m values at n=1. As shown in the figure, the self coupling drops off slightly more rapidly for TM than TE, and the larger steps lose power much more rapidly at higher modes. This clearly illustrates the primary function of horn design; minimising scattering to unwanted higher order modes, while smoothing the transition to free space.

6.2.4 Determining the S matrices

The next step in designing the code concerned using the P-matrix to generate an S matrix (scattering matrix). A scattering matrix describes the effect of an action on an electromagnetic wave, in this case either propagating through space or navigating a change in boundary conditions: a step. There are four S submatrices in a two port S matrix for a single interaction, each representing a single S parameter, as described by Eqn. 4.2. The S11 matrix denotes the return loss, power which enters at port 1, and is reflected back through port 1. The S22 matrix denotes output reflection, while the S12 and S21 describe the propagation in both directions across the step interface. The antenna theorem ensures the equivalency of the S11/22 and S12/21 upon reversal of the source direction in the horn. This is explained at length in Dobrowolski, (2016), from which Fig 6.10 was obtained, showing a general scattering matrix. The systems described by scattering matrices in this thesis are solely two-element, with S11 and S12 to the left of the matrix, and S21, S22 to the right (Eqn. 4.2).

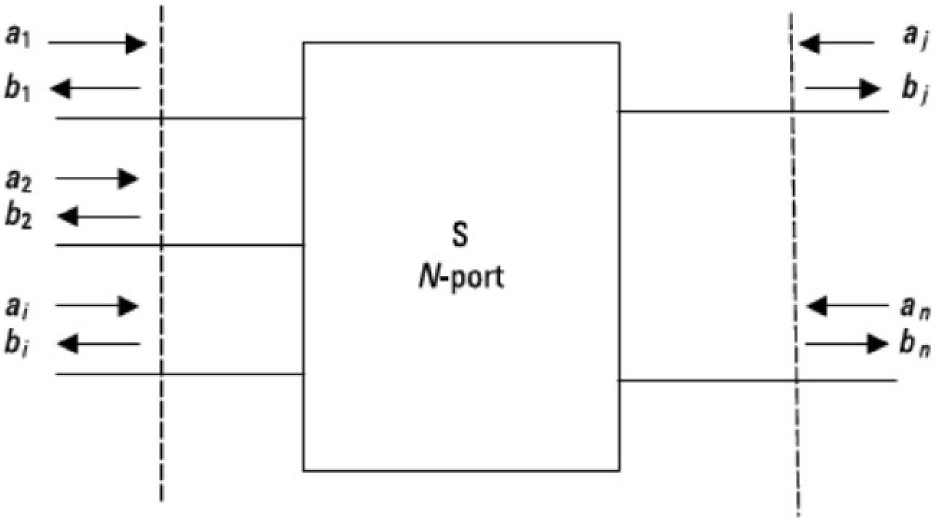

FIGURE 6.10: Scattering matrix schematic, showing general scattering parameters for an N-port system. Dobrowolski, (2016)

To produce the scattering matrix for a step from the P-matrix, the Q and R matrices must also be calculated. These represent the internal self coupling on the two sides of the step. The Q and R matrices are diagonal in form, as they only contain self coupling terms. These have a value of unity where the mode propagates, and become purely imaginary if the mode becomes evanescent. Evanescence signals that these modes will not be propagated to the next step. In the case of a non-zero step size, the Q and R matrices will often change from real to imaginary at different points along the diagonal, as more modes may propagate in the larger guide, which would be below cutoff in the smaller. TE and TM modes may also cut on at different positions. This can be seen directly by comparing Fig. 6.11 and Fig. 6.12. One of the matrices has just one mode propagating, the TE11. However, the other shows TE11, TE22 and TE33 propagating. No TM modes have yet cut on, showing that cut-on frequencies are indeed distinct for TE and TM modes of the same order.

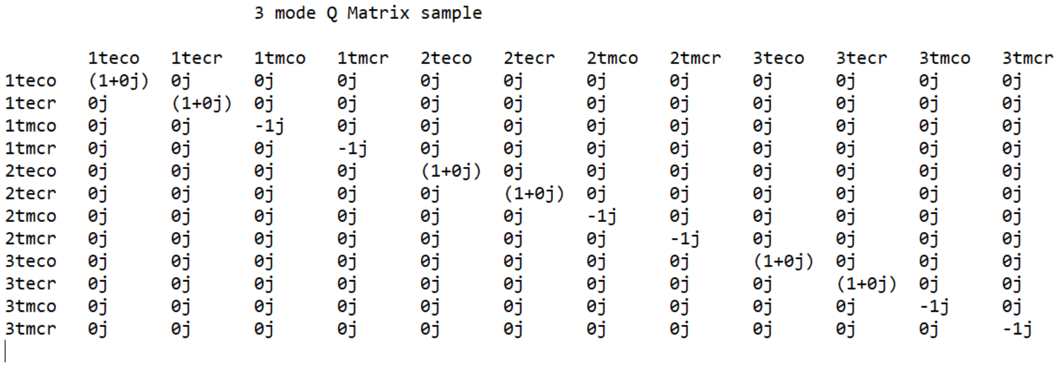

```
                        3 mode Q Matrix sample

        1teco   1tecr   1tmco   1tmcr   2teco   2tecr   2tmco   2tmcr   3teco   3tecr   3tmco   3tmcr
1teco   (1+0j)  0j      0j      0j      0j      0j      0j      0j      0j      0j      0j      0j
1tecr   0j      (1+0j)  0j      0j      0j      0j      0j      0j      0j      0j      0j      0j
1tmco   0j      0j      -1j     0j      0j      0j      0j      0j      0j      0j      0j      0j
1tmcr   0j      0j      0j      -1j     0j      0j      0j      0j      0j      0j      0j      0j
2teco   0j      0j      0j      0j      (1+0j)  0j      0j      0j      0j      0j      0j      0j
2tecr   0j      0j      0j      0j      0j      (1+0j)  0j      0j      0j      0j      0j      0j
2tmco   0j      0j      0j      0j      0j      0j      -1j     0j      0j      0j      0j      0j
2tmcr   0j      0j      0j      0j      0j      0j      0j      -1j     0j      0j      0j      0j
3teco   0j      0j      0j      0j      0j      0j      0j      0j      (1+0j)  0j      0j      0j
3tecr   0j      0j      0j      0j      0j      0j      0j      0j      0j      (1+0j)  0j      0j
3tmco   0j      0j      0j      0j      0j      0j      0j      0j      0j      0j      -1j     0j
3tmcr   0j      0j      0j      0j      0j      0j      0j      0j      0j      0j      0j      -1j
|
```

FIGURE 6.11: Q matrix sample, showing cutoff position.

The P, Q and R matrices may now be converted to the S matrix by use of Eqns. 6.19 - 6.22, (Olver, (1994). These apply a series of matrix algebraic operations to compute each of the four elements of the S matrix from different combinations of the P, Q and R matrices. Q and R exchange places in the equations for S11, S22 and S12, S21, respectively. This is due to the inherent reciprocity of the system, the S12 matrix for a receiving horn will correspond to the S21 matrix for a transmitting horn, and vice versa.

$$[S_{11}] = \Big[[R^*] + [P]^T[Q]^{-1}[P]\Big]^{-1}\Big[[R] - [P]^T[Q]^{-1}[P]\Big] \tag{6.19}$$

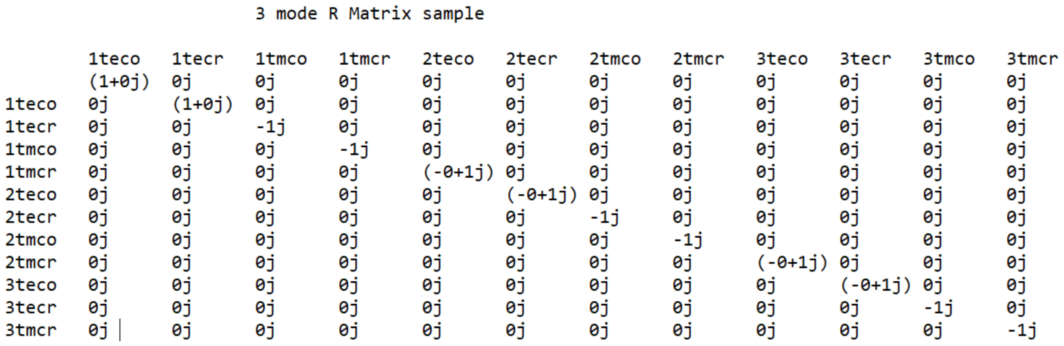

```
                    3 mode R Matrix sample

        1teco   1tecr   1tmco   1tmcr   2teco   2tecr   2tmco   2tmcr   3teco   3tecr   3tmco   3tmcr
        (1+0j)  0j      0j      0j      0j      0j      0j      0j      0j      0j      0j      0j
1teco   0j      (1+0j)  0j      0j      0j      0j      0j      0j      0j      0j      0j      0j
1tecr   0j      0j      -1j     0j      0j      0j      0j      0j      0j      0j      0j      0j
1tmco   0j      0j      0j      -1j     0j      0j      0j      0j      0j      0j      0j      0j
1tmcr   0j      0j      0j      0j      (-0+1j) 0j      0j      0j      0j      0j      0j      0j
2teco   0j      0j      0j      0j      0j      (-0+1j) 0j      0j      0j      0j      0j      0j
2tecr   0j      0j      0j      0j      0j      0j      -1j     0j      0j      0j      0j      0j
2tmco   0j      0j      0j      0j      0j      0j      0j      -1j     0j      0j      0j      0j
2tmcr   0j      0j      0j      0j      0j      0j      0j      0j      (-0+1j) 0j      0j      0j
3teco   0j      0j      0j      0j      0j      0j      0j      0j      0j      (-0+1j) 0j      0j
3tecr   0j      0j      0j      0j      0j      0j      0j      0j      0j      0j      -1j     0j
3tmcr   0j |    0j      0j      0j      0j      0j      0j      0j      0j      0j      0j      -1j
```

FIGURE 6.12: R matrix sample, showing cutoff position.

$$[S_{12}] = 2\left[[R^*] + [P]^r[Q]^{-1}[P]\right]^{-1}[P]^\top \tag{6.20}$$

$$[S_{21}] = 2\left[[Q] + [P][R^*]^{-1}[P]^T\right]^{-1}[P] \tag{6.21}$$

$$[S_{22}] = -\left[[Q] + [P][R^*]^{-1}[P]^T\right]^{-1}\left[[Q] - [P][R^*]^{-1}[P]^T\right] \tag{6.22}$$

The S matrices calculated thus far describe a discontinuous step of zero longitudinal extent. To construct a realistic optical system, a propagation term must be included to space the steps apart into corrugations, when multiple steps are introduced. This is encoded in the V matrix, a diagonal matrix of phase terms, describing how the phase of the wavefront changes as it passes along a smooth section of waveguide between steps. As there are by definition no disruptive features in this section aside from the phase factor, there is no change in amplitude when a propagation matrix is applied.

The V matrix is computed using the quantity β, which is the guide wavenumber as it appears in the phase evolution form, and serves to determine if a mode is propagating along a given section of waveguide. Calculating β requires the Bessel function or Bessel derivative related to the given mode, and the operating frequency.

$$\beta_{TE} = \sqrt{1 - \frac{(p'_{nm}(n,m)}{(\omega a\sqrt{\mu_0\epsilon_0}^2)}} \tag{6.23}$$

$$\beta_{TM} = \sqrt{1 - \frac{(p_{nm}(n,m)}{(\omega\sqrt{\mu_0 \epsilon_0})^2}}. \tag{6.24}$$

These values of β are then combined into a complex exponential phase relation to yield the final elements of the V matrix, as shown in Equation 6.25. dL specifies the distance over which the propagation will occur and upon which the phase change depends.

$$V_{ij} = e^{ik_0\beta_{ij} \cdot dL} \tag{6.25}$$

A sample propagation matrix for three sets of modes is shown in Fig. 6.13. Upon examining the P matrix of the same code iteration, it was found that the TE11 and TM11 alone were propagating. A complex phase term is required to describe the propagation of the EM waves. The phase terms in the V matrix are complex for TE11 and TM11, and real thereafter, so both matrices agree, indicating that only the first TE and TM mode propagate, with the higher order modes being evanescent.

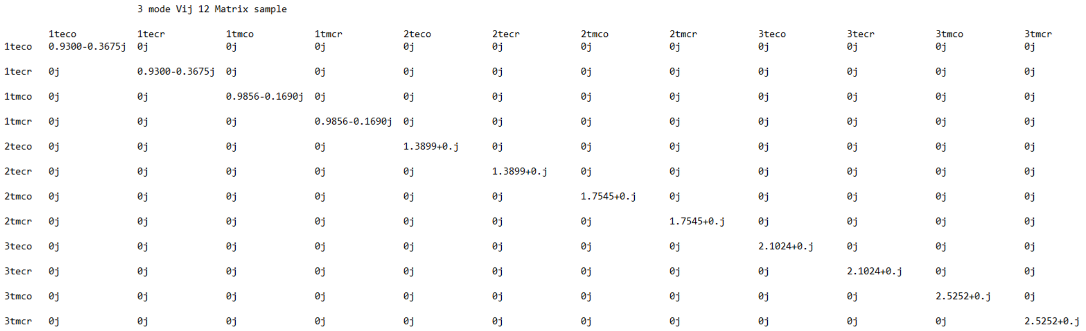

```
                3 mode Vij 12 Matrix sample

      1teco          1tecr          1tmco          1tmcr          2teco          2tecr          2tmco          2tmcr          3teco          3tecr          3tmco          3tmcr
1teco 0.9300-0.3675j 0j             0j             0j             0j             0j             0j             0j             0j             0j             0j             0j

1tecr 0j             0.9300-0.3675j 0j             0j             0j             0j             0j             0j             0j             0j             0j             0j

1tmco 0j             0j             0.9856-0.1690j 0j             0j             0j             0j             0j             0j             0j             0j             0j

1tmcr 0j             0j             0j             0.9856-0.1690j 0j             0j             0j             0j             0j             0j             0j             0j

2teco 0j             0j             0j             0j             1.3899+0.j     0j             0j             0j             0j             0j             0j             0j

2tecr 0j             0j             0j             0j             0j             1.3899+0.j     0j             0j             0j             0j             0j             0j

2tmco 0j             0j             0j             0j             0j             0j             1.7545+0.j     0j             0j             0j             0j             0j

2tmcr 0j             0j             0j             0j             0j             0j             0j             1.7545+0.j     0j             0j             0j             0j

3teco 0j             0j             0j             0j             0j             0j             0j             0j             2.1024+0.j     0j             0j             0j

3tecr 0j             0j             0j             0j             0j             0j             0j             0j             0j             2.1024+0.j     0j             0j

3tmco 0j             0j             0j             0j             0j             0j             0j             0j             0j             0j             2.5252+0.j     0j

3tmcr 0j             0j             0j             0j             0j             0j             0j             0j             0j             0j             0j             2.5252+0.j
```

FIGURE 6.13: V matrix sample, showing the effect of a propagation of arbitrary length along a single smooth cylindrical waveguide section of diameter approximately λ. Propagation of TE11 and TM11 modes, is seen, with evanescence of higher order modes.

To propagate the simulation forward along multiple sections, the matrices representing individual elements are cascaded, as with general matrix optics, such as those discussed in Chapter 2. It is desirable to begin a waveguide model with a long propagation, as that serves to filter out any evanescent power. If such power were to reach the corrugations, it could scatter to propagating modes in the corrugated section and increase the cross-polarisation. However, the design of the routine is such that the V matrices are produced from the β values calculated for the first P matrix, occurring after the initial propagation; as such they are generated for the first step. A new set of V_{ij}s, labelled *Vijinit*, are used to generate the first long propagation. The radius a used for these matrix calculations corresponds to the radius of the waveguide section of a horn, which supplies the necessary long propagation.

6.2.5 Introduction of offsets

As discussed previously, corrugations may be offset to simulate the tolerance on tightness and rigidity of the dowel pins which hold the stacks of platelets in place for platelet horn arrays. Due to the off-axis nature of such shifts, radial error techniques (as used in the tolerancing analysis of the micromachined and electroformed ALMA horns) will not suffice. Here an offset is introduced to each section, with the values drawn from a uniform or Gaussian random distribution. A Gaussian distribution is centred on zero, and its standard deviation is determined by the level of the manufacturing tolerance to be simulated. A nonzero offset can then move the section positively or negatively with respect to boresight in either the x or y direction. Similarly, a uniform distribution is allowed to vary randomly within the tolerance level, with equal probability of selecting any point along the interval. A Gaussian distribution can provide a more realistic picture of random offsets than a uniform distribution, as it gives more insight into the effects of worst case scenarios. However, it can also give occasional unphysical results, as there is no true limit to its potential deviation from the mean.

The offsets are read in from a file containing an ordered list of Δx values, drawn from a distribution with a given standard deviation (SD), one for each section in the horn, followed by a similar list for y. In the case of a typical dowel toleranced horn, the SD values will be constant throughout, however the ability to tolerance sections individually imparts considerable additional flexibility at virtually no cost in computation time; as such it is retained in case of future requirements.

6.2.6 Numerical computation of ‘offset’ integrals

Obtaining the S matrix for the horn requires evaluation of the overlap integrals at every step. This must be done numerically if offsets are present, as discussed previously. A schematic showing the integration process across an offset step is shown as Fig. 6.14. The smaller circle represents a corrugation, which is offset with respect to the slot, as this is a separate platelet in the stack. The integration grid is placed across a square of side length equal to the diameter of the larger section. As such, the code accurately computes offsets for any case in which the step is greater than the offset. This is always the case in corrugated horn design, as corrugations are usually no smaller than $\lambda/4$, and offsets approaching that magnitude would render a horn useless for most applications. For a smooth walled horn it could be more of a concern, but the benefits of platelet based design are reduced when manufacturing smooth walled horns, as these are much more straightforward to mill. The resolution variable chosen upon running the code initially determines the number of points computed across the square in which the large section is inscribed. A fraction of approximately $\pi/4$ of these fall within the section and are included in the computation.

Fig. 6.15 shows a standard S21 matrix, in this case for n=1,n=2 and m=1,m=2. The smallest grid boxes represent individual coefficients, of which there are 16 in each mode pairing (all combinations of TE and TM for both orthogonal cases.). In an uncorrugated waveguide, only the blue boxes on the diagonal have nonzero values. These are self coupling modes. In a perfect horn with corrugations, the red boxes are also populated with non-zero values, these are couplings within the same n order. Finally, in an imperfect horn with lateral offsets, there are potentially nonzero values everywhere. For small numbers of included orders, the modes coupled within the same order represent a large fraction of the total number of mode combinations possible. However, as the number of orders included grows, the inter-order mode combinations dominate. This makes the matrix for the imperfect horn much more structured and complex when large numbers of orders are considered.

The function of the waveguide section in ensuring a single moded input can be seen by looking at the TE11 and TE11-orthogonal columns of the S21 matrix for the initial section. Ideally, this will have non-zero values only in the TE11 rows, implying that power is scattering from TE11 to TE11 only, and is not present in other modes. If nonzero values are present in other rows, this implies that the waveguide section is either too wide, allowing propagation of

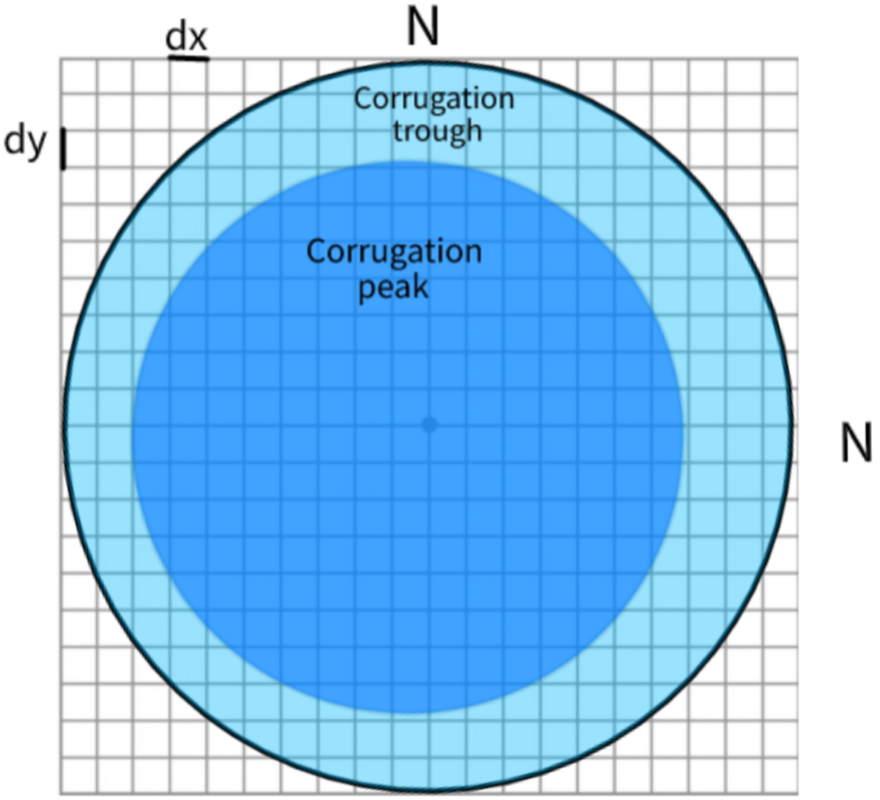

FIGURE 6.14: Diagram of the grid used for the offset step integration procedure.

higher modes, or too short, implying insufficient distance for evanescent decay. The output for the first section is shown in Fig. 6.16. The first terms in the n=1 box refer to the TE11 amplitude. Upon taking the magnitude of the complex amplitude terms, it is found that both the TE11 and its orthogonal agree with the unitary normalisation set at the input to 5 decimal places, even at reasonably low resolution (140 integrations per axis). The physical appearance of the input section can be seen in Fig. 6.18, further in the chapter.

The output of a perfect horn with all input power in the TE11 mode may then be contrasted with the output of a horn with offsets included. The perfect horn would retain most of its power in the TE11 mode, with some scattering to other n=1 modes, these could be TE or TM, and/or of different azimuthal orders. However, no power would be present in different n orders (n=0,2,3...) as these start with zero power at the input, and cannot receive scattered power from the n=1 order as no radial intermodal scattering is permitted in a radially symmetric horn. This theory was verified using perfect and offset versions of the QUBIC horn. As seen in the first section of Fig 6.17, the perfect horn has a

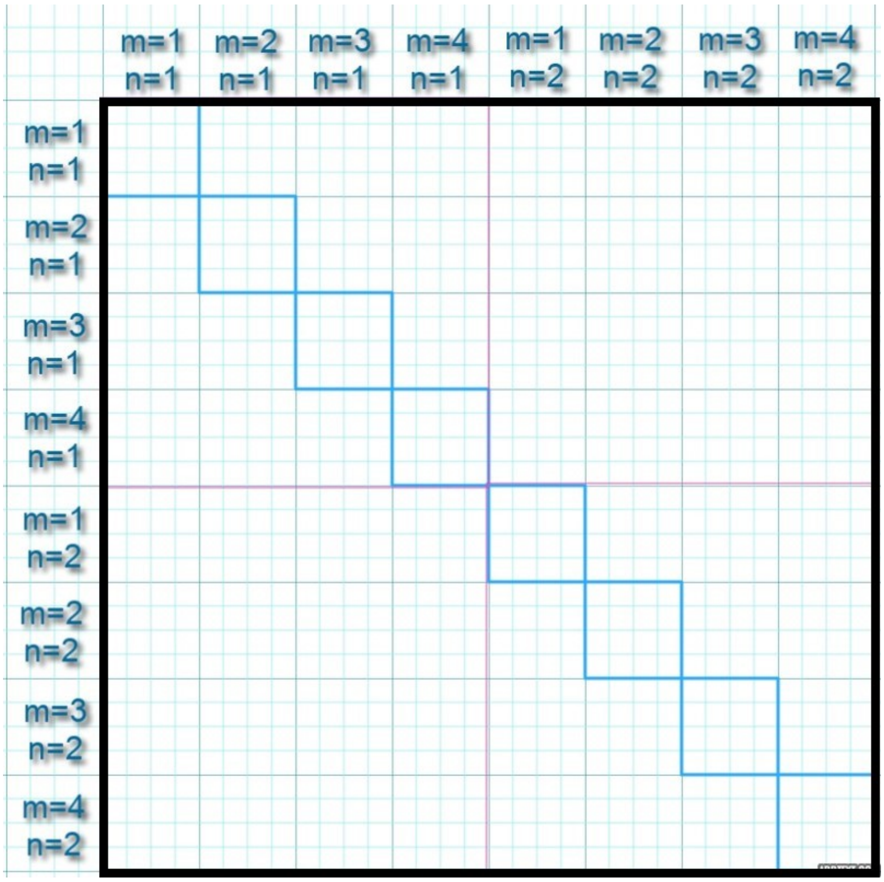

FIGURE 6.15: Regions of an S21 matrix.

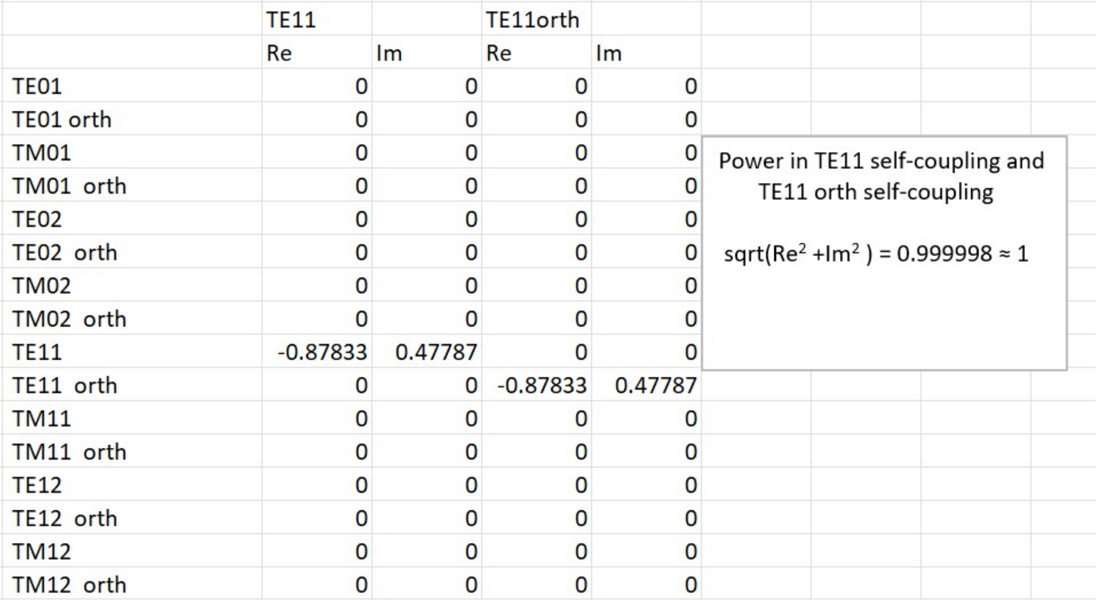

	TE11		TE11orth	
	Re	Im	Re	Im
TE01	0	0	0	0
TE01 orth	0	0	0	0
TM01	0	0	0	0
TM01 orth	0	0	0	0
TE02	0	0	0	0
TE02 orth	0	0	0	0
TM02	0	0	0	0
TM02 orth	0	0	0	0
TE11	-0.87833	0.47787	0	0
TE11 orth	0	0	-0.87833	0.47787
TM11	0	0	0	0
TM11 orth	0	0	0	0
TE12	0	0	0	0
TE12 orth	0	0	0	0
TM12	0	0	0	0
TM12 orth	0	0	0	0

Power in TE11 self-coupling and TE11 orth self-coupling

sqrt(Re^2 +Im^2) = 0.999998 ≈ 1

FIGURE 6.16: TE11 coupling coefficients for the initial S21 at the waveguide

maximum amplitude on the order of 10^{-3} in the zeroth n order, corresponding to power on the order of $10^{-6} - 10^{-7}$. This is an artefact of the numerical routine. To demonstrate that no power is found in other extraunitary orders, the power may be summed across the n=1 order, and should sum to unity for both the TE11 and TE11-orthogonal modes, giving a total of 2. The observed total upon summation is slightly over 2, however errors on the 10^{-3} level are negligible given that the resolution of integration across each mode was 140×140. This shows, as expected, that power is scattered within the n=1 order only. Furthermore, it shows that scattering to $m < 2$ modes is negligible. One last observsation of note is that every second entry in the n=1 array is zero, these represent co-polar to cross-polar couplings, and are zero in any cylindrically symmetric system.

In the subsequent sections of Fig. 6.17, the effects of lateral offsets on the total power are considered for two levels of offset, both with a Gaussian distribution. At 0.02 mm SD, symmetry is observed to break down across the modes. All other modes now receive power, except couplings between orthogonal modes of the n=0 order. These stay exactly 0 throughout, as these mode couplings do not physically exist for $n = 0$, but are included to maintain simplicity in dealing with matrices. Coupling between orthogonal modes is now allowed for higher orders, albeit at a low level. Summation of the n=0 values yields a total of approximately 0.03. This is 1.5% of the total power, about -18 dB. Total power in the n=1 orders sums to approximately 1.9, or 95%. That indicates that an additional 3.5% has been lost to back propagation (return loss) or to higher order couplings, leaving $n = 1$ power at 95%. This could have subtle effects on the main beam of a farfield pattern and would substantially affect the cross-polarisation.

The final section shows a scenario which is worse than what is likely realistic, with a 0.1 mm standard deviation on errors in both dimensions. The n=0 modes contain almost 10% of the total power and the total power contained in the n=1 order decreases to 85%. This alone would cause severe distortion of the main farfield beam. Furthermore, orthogonal couplings have amplitudes approaching the 10^{-1} level, meaning their power is on the order of 10^{-2}, -20 dB. These propagations are completely absent in a perfect horn, and as such are highly undesirable.

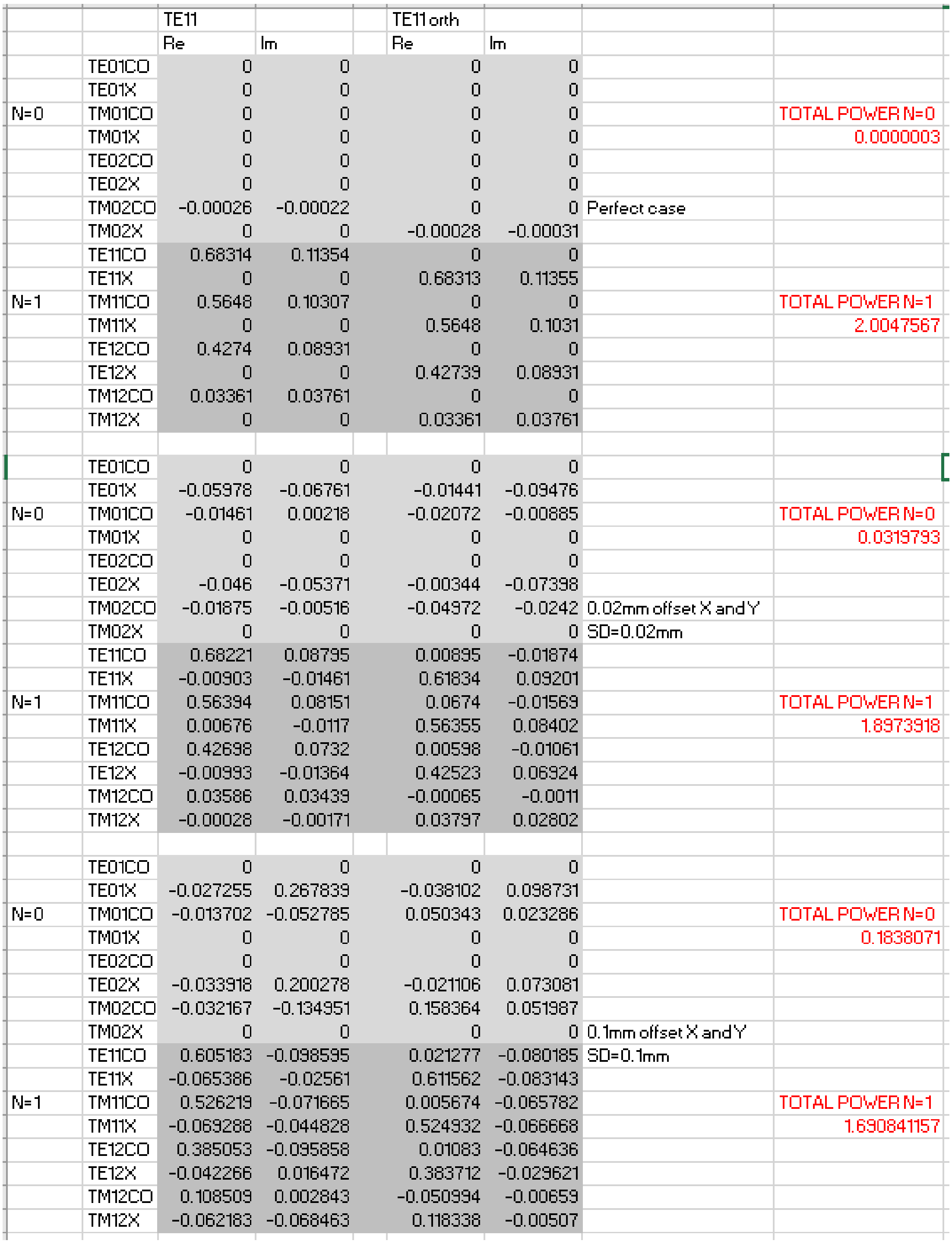

		TE11		TE11 orth			
		Re	Im	Re	Im		
	TE01CO	0	0	0	0		
	TE01X	0	0	0	0		
N=0	TM01CO	0	0	0	0		TOTAL POWER N=0
	TM01X	0	0	0	0		0.0000003
	TE02CO	0	0	0	0		
	TE02X	0	0	0	0		
	TM02CO	-0.00026	-0.00022	0	0	Perfect case	
	TM02X	0	0	-0.00028	-0.00031		
	TE11CO	0.68314	0.11354	0	0		
	TE11X	0	0	0.68313	0.11355		
N=1	TM11CO	0.5648	0.10307	0	0		TOTAL POWER N=1
	TM11X	0	0	0.5648	0.1031		2.0047567
	TE12CO	0.4274	0.08931	0	0		
	TE12X	0	0	0.42739	0.08931		
	TM12CO	0.03361	0.03761	0	0		
	TM12X	0	0	0.03361	0.03761		
	TE01CO	0	0	0	0		
	TE01X	-0.05978	-0.06761	-0.01441	-0.09476		
N=0	TM01CO	-0.01461	0.00218	-0.02072	-0.00885		TOTAL POWER N=0
	TM01X	0	0	0	0		0.0319793
	TE02CO	0	0	0	0		
	TE02X	-0.046	-0.05371	-0.00344	-0.07398		
	TM02CO	-0.01875	-0.00516	-0.04972	-0.0242	0.02mm offset X and Y	
	TM02X	0	0	0	0	SD=0.02mm	
	TE11CO	0.68221	0.08795	0.00895	-0.01874		
	TE11X	-0.00903	-0.01461	0.61834	0.09201		
N=1	TM11CO	0.56394	0.08151	0.0674	-0.01569		TOTAL POWER N=1
	TM11X	0.00676	-0.0117	0.56355	0.08402		1.8973918
	TE12CO	0.42698	0.0732	0.00598	-0.01061		
	TE12X	-0.00993	-0.01364	0.42523	0.06924		
	TM12CO	0.03586	0.03439	-0.00065	-0.0011		
	TM12X	-0.00028	-0.00171	0.03797	0.02802		
	TE01CO	0	0	0	0		
	TE01X	-0.027255	0.267839	-0.038102	0.098731		
N=0	TM01CO	-0.013702	-0.052785	0.050343	0.023286		TOTAL POWER N=0
	TM01X	0	0	0	0		0.1838071
	TE02CO	0	0	0	0		
	TE02X	-0.033918	0.200278	-0.021106	0.073081		
	TM02CO	-0.032167	-0.134951	0.158364	0.051987		
	TM02X	0	0	0	0	0.1mm offset X and Y	
	TE11CO	0.605183	-0.098595	0.021277	-0.080185	SD=0.1mm	
	TE11X	-0.065386	-0.02561	0.611562	-0.083143		
N=1	TM11CO	0.526219	-0.071665	0.005674	-0.065782		TOTAL POWER N=1
	TM11X	-0.069288	-0.044828	0.524932	-0.066668		1.690841157
	TE12CO	0.385053	-0.095858	0.01083	-0.064636		
	TE12X	-0.042266	0.016472	0.383712	-0.029621		
	TM12CO	0.108509	0.002843	-0.050994	-0.00659		
	TM12X	-0.062183	-0.068463	0.118338	-0.00507		

FIGURE 6.17: TE11 coupling coefficients for the final S21 at the mouth of the horn, a comparison between a perfect design and different offset levels.

6.2.7 Farfield pattern generation

To simplify and speed up the generation of farfield plots, only the single moded case was analysed. This entailed the assumption that all input power from the waveguide section was in the TE11 mode. The TE11 column and TE11-orthogonal column are extracted from the final S21 matrix at the mouth of the horn, and used in the farfield generation routines. Single moded analysis is valid for most systems, however some wideband horns, such as QUBIC, become multimoded at the upper edge of their bandwidth, allowing more modes in at the input. As such, more input columns would need to be analysed to account for this in an analysis of QUBIC at 220 GHz. The column matrices store all data about the system, as such a separate but similar program was designed to run a plotting sequence directly from these relatively small matrices instead of from geometry files. This means that further plots can be generated at a later date from saved arrays without requiring a repeat of the mode matching integration.

The system far-field propagation formulas from the original analytical code were modified to account for the increased matrix size, as the PyScatter code developed by Burke, (2021) could model only radially symmetric systems, and thus did not compute scattering between n orders or between co- and cross-polar modes. The field coefficients are computed for TE and TM modes, and their orthogonal counterparts, for both x and y components. These coefficients are then multiplied by the expressions for the fields, and summed to give total fields at a grid of points (x, y). The x and y field components are converted to co-polar and cross-polar total power using equations 6.26 and 6.27, where here x and y represent the x and y field components. These also depend on θ, the boresight angle, and it is this angle which is varied to derive the angular beam patterns used to determine horn performance. The summation of x and y polarisation power components gives the main beam total power, while including only y components yields the cross-polar power. This reaches maximum at azimuthal angles $\phi = \frac{n\pi}{4}$, thus the cross-polar cut is taken at 45 degrees. The main beam electric field is evaluated at an azimuth of 0 ° only; the 45 and 90 degree traces present in PyScatter were removed for clarity and ease of plotting. The changes applied to convert from the analytical to the numerical process may be observed by the excerpts from PyScatter and NumCross in Appendix B and Appendix C, respectively.

$$P_{co} = (1 + \cos(\theta))^2 * (|P_x|^2 + |P_y|^2) \tag{6.26}$$

$$P_{cross} = (1 + \cos(\theta))^2 * (|y|^2) \tag{6.27}$$

6.3 Application to QUBIC

6.3.1 3D plotting software

A Python routine was constructed to represent the QUBIC horn as a 3D rendered model, as opposed to a 2D cutaway slice. The code was also capable of showing the profile of linear offsets as they would appear on a real horn. This requires the use of a different centre point for each stacked section in the simulation. The entire horn with offsets included is shown as Fig. 6.18 below. Although the offsets were set at a relatively large ±50 μm, they are not immediately apparent in the plot.

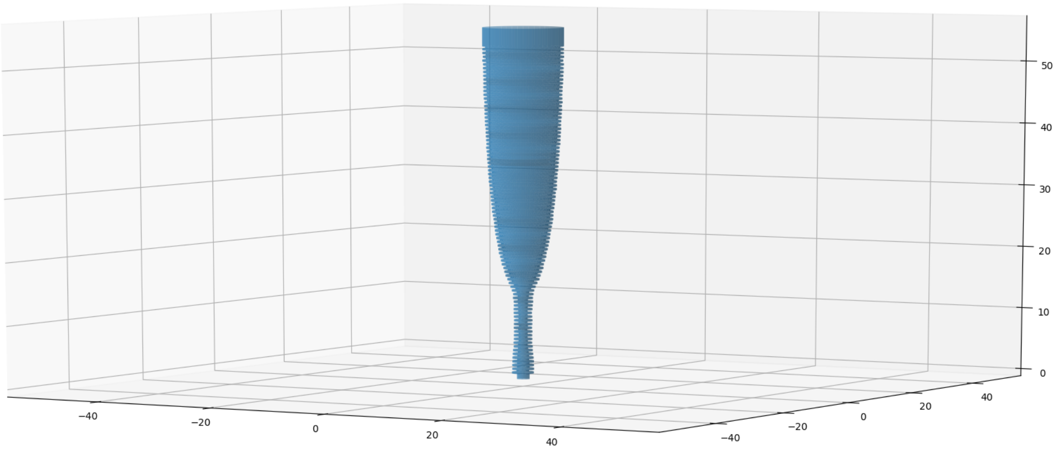

FIGURE 6.18: 3D scatter plotted rendition of the QUBIC horn, with ±50 μm offsets included.

To show the offsets between sections, it was necessary to magnify the throat section, as that is where offsets will represent the largest fraction of the total radius, and thus have the greatest impact on mode scattering. Fig. 6.19 shows the throat section of the horn, with the x and y axes magnified by a factor of 5 compared to the z axis. The offsets are clearly visible here, especially in the narrowest section.

6.3.2 Computational constraints

The core numerical routine in NumCross is the evaluation of the cross product representing the Poynting vector at each point on the xy integration grid. The

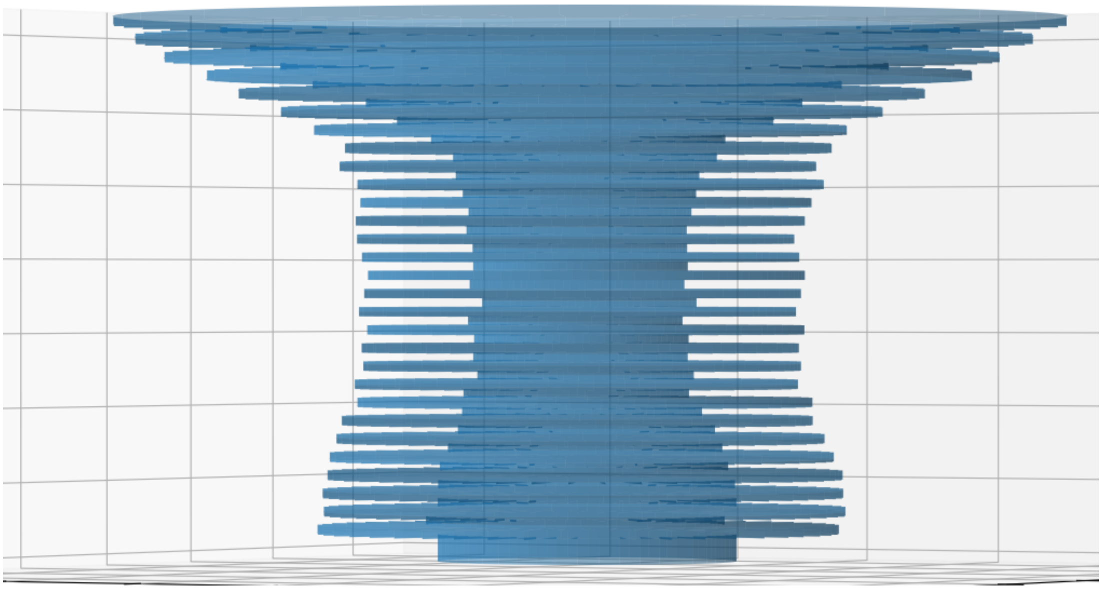

FIGURE 6.19: 3D scatter plotted rendition of the throat section of the QUBIC horn, with ±50 μm offsets included. All axes are in millimetres.

function takes seven input variables: x, y, $nvar1$, $nvar2$, $mvar1$, $mvar2$ and N. x and y represent the position on the grid of the evaluation. *nvar1* and *nvar2* are the mode indices that the power is scattered from, while *mvar1* and *mvar2* denote the indices of the mode to which power is scattered. Finally, N is the section number along the horn at which the step takes place. This is included in the code appendices, Appendix B and Appendix C. *mvar1* and *mvar2* have no analogues in the analytical software, as it requires cylindrical symmetry at steps, and thus has no radial mode scattering. As all variables are incorporated in nested *for* loops, the number of iterations of the point evaluation functions required combine multiplicatively. Eqn. 6.28 shows the expression for the total number of cross product computations required to analyse a horn. The *nmodes* term comprises the number of modes to be analysed, which is 4 times the product of the number of radial and azimuthal orders included in the simulation. The factor of 4 accounts for the pairs of orthogonal TE and TM modes. R denotes the xy resolution used. Finally $N - 1$ is the number of steps in the horn, which is one less than the number of sections N.

$$\Sigma i = (nmodes)^2 \times R^2 \times (N - 1) \tag{6.28}$$

For PyScatter, as mentioned elsewhere, the benchmark mode number used is 30 modes in TE and 30 in TM for each n order. This yields an S matrix of size 60 × 60 for the combined TE and TM. To obtain the same modal inclusivity numerically, with the potential for offsets, larger matrices are required. Orthogonal mode coupling is allowed, increasing the matrix size to 120 × 120 for each n. Furthermore, coupling between n orders is now permitted, increasing the size further to $120N \times 120N$, N being the number of n orders included in the simulation. Using Eqn. 6.28, we can compute Σi, the total number of iterations required to model a horn. Using the 176 section QUBIC horn as an example, the computational requirements of performing this integration may be investigated. At a reasonably high xy resolution N of 250×250, and including 10 n orders, this amounts to $1200^2 \times 250^2 \times 175 \approx 10^{13}$ iterations of the point evaluation functions. As propagation matrices are diagonal, their computation time is irrelevant for large mode numbers. A standard desktop PC can compute $\sim 10^5$ iterations per second, taking years to complete 10^{13}. Evidently, to analyse an entire horn to analytical precision in a reasonable timeframe, a supercomputer or cluster core module would be required. However, in the case of small offsets and a fairly well-behaved horn, many modes can be excluded at little cost. When combined with a modest decrease in resolution, this brings the simulation time into the realm of days, making proof of concept for an entire horn reachable for a standard desktop machine.

To check what resolution level was required for computing the offset horn parameters, the perfect horn was simulated at five resolutions, and compared with the analytical horn profile computed by PyScatter. The result is shown as Fig. 6.20. The 10 × 10 point simulation is completely unphysical, with the beam depressed on axis, and reaching maxima several degrees off axis. The cross-polar level lies just 5 dB below the co-polar. The 20×20 simulation matches the co-polar beam almost perfectly, deviating only at the -30 dB level. This is a remarkable change for only a fourfold increase in array size. However, the cross-polar is uneven and much lower than analytically calculated. The 30×30 simulation raises the cross-polar power to within 5 dB of the predicted peaks. The 40×40 resolution tightens this discrepancy to 4 dB, and 50×50 to ∼ 2 dB. A variation of ±2 dB at the -30 dB level is quite negligible, whereas a change of ±4 dB is much more significant. In light of this, 50×50 resolution was chosen for use in all subsequent NumCross simulations of the QUBIC horn. This simulation shows that the NumCross routine converges to the analytically computed beam pattern with increasing resolution, as is expected for a numerical approximation.

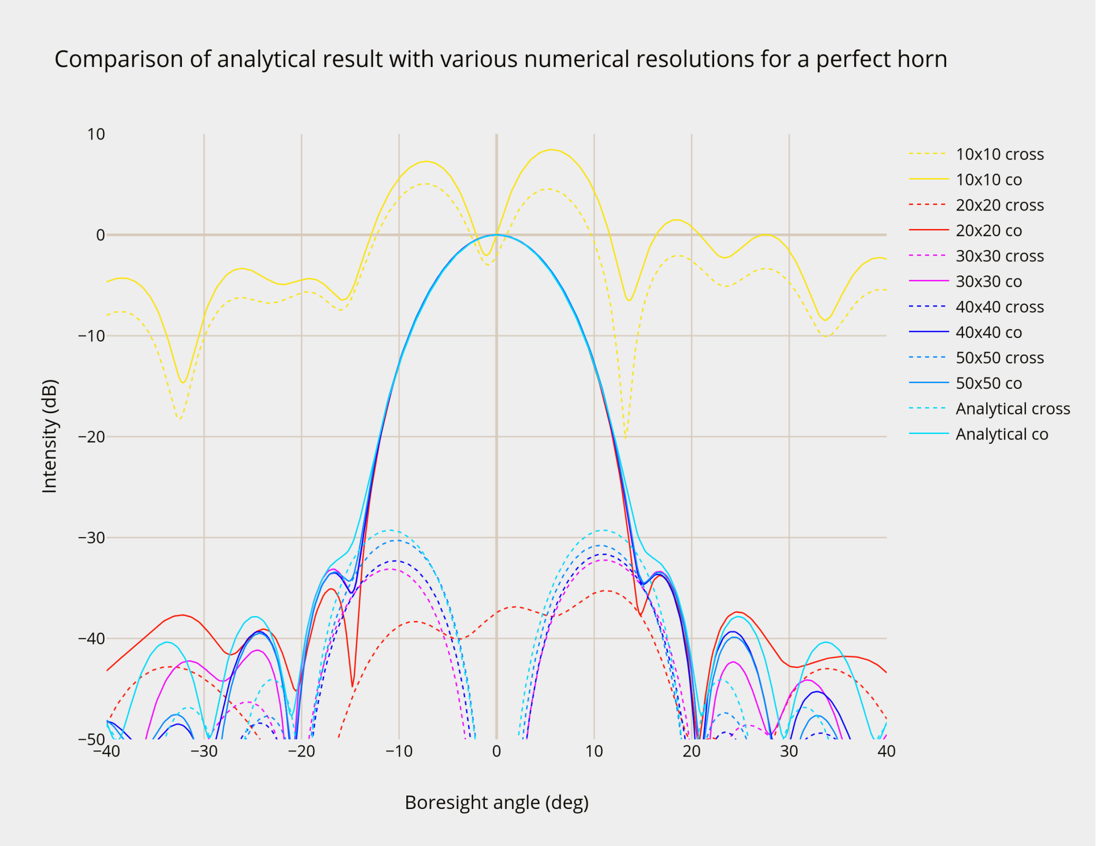

FIGURE 6.20: Variation of farfield beam patterns with numerical resolution level for the perfect QUBIC horn.

Simulations were run at the 50×50 resolution level to test the modelling of a 176 section QUBIC horn when offsets were included. A plot was then made of the S21 coefficient transmission through the horn for 10 iterations of an offset horn, to check which radial and azimuthal orders contained a meaningful amount of power (and thus have to be calculated). A uniform distribution was chosen over the Gaussian alternative, to remove the possibility of unphysical extreme events (2-3σ). The limits for the uniform random distribution were set at ± 50 μm, a reasonably coarse but possible tolerance. The maximum intersectional offset was thus $2 \times \sqrt{50^2 + 50^2} \approx 141$ μm. For comparison, the corrugation depth at the mouth of the horn was approx 600 μm. This was performed for five radial modes and eight angular modes. The 10 simulations were performed in parallel, each taking one core of a 12 core high performance PC. This circumvented the extra coding which would be required to parallelise individual simulations across multiple cores. The simulations required 36 hours to complete on a single core each. The additional 2 cores were left idle, to avoid strain on the cooling system.

6.3.3 Results

A plot of coupling coefficients for the trial simulation is shown in Fig. 6.21. This plot contains a large amount of information regarding the requirements of NumCross. The 1600 points are colour coded to determine which of the 10 Monte Carlo iterations they pertain to. In turn, there are 160 available positions on the x-axis corresponding to all possible scattering modes allowed within the bounds of the simulation. The assignment of modes to positions is explained in the axis label comment. The points are plotted logarithmically to highlight the exponential decline in power for higher modes. To allow the logarithmic scale to plot all points without undefined results, the aforementioned analytically zero-valued mode couplings in the n=0 order have been set to an arbitrary value of -70 dB. The black crosses on the plot represent the values obtained for zero offset. In the limit of perfect resolution, these would be zero outside the n=1, they are included for completeness and to show that the high power scattered to other n orders is not simply an artefact of the numerical nature of the routine.

Most of the input power is still contained in the TE11 mode for the offset simulations ($\sim$ 55-70%, as the n=1 value falls in the -1.5/-2.5 dB region for all simulations) and more generally in n=1, implying that the horns are still functional at a basic level. The power in radial and azimuthal orders is seen to decrease approximately exponentially with increasing order from the n=1 and m=1 orders (appearing as linear on a log graph). The decrease is more rapid for radial than for azimuthal orders. The n=4 order and the m=7,8 orders all have peak power in the <-35 dB region. This implies that they are the limiting orders past which the relevance to the cross-polarisation level is minimal, as cross-polarisation beneath -30 dB is considered to be excellent. It follows that, for tolerances up to and including ± 50 μm, 5 radial and 8 azimuthal orders are sufficiently inclusive for the calculation. Additionally, the maximal power seen outside the n=1 for zero offset is well below -40 dB, reiterating the assertion that the resolution used is adequate for these simulations. The total power contained in each simulation varied, with the lowest being 0.851 and the highest 0.983. This implies non-negligible return loss in the system, which is expected for significant tolerancing errors. It also shows the variety in output from the randomness of the tolerancing, from a -9 dB loss factor for the worst horn to a -17 dB loss factor for the best horn. The sum for the zero offset simulation was 0.993, implying return loss below -20 dB for the perfect horn, as expected.

The dominance of co-polar over cross-polar power is visible in the n=1 azimuthal order, with the TE11 and TM11 co-polar modes both showing large power >-7 dB, and their cross-polar components lying at <-25 dB. However, this high performance is not seen in the m=1 column of any of the other n orders, the power is much more uniformly distributed between the co- and cross-polar components. This can be seen most clearly with the TE21 values, as they are tightly bunched, with most falling between -17 and -27 dB. This loss of polarisation at relatively high power levels (>-20 dB) would imply a deterioration in cross-polarisation for the offset error horns due to the scattering between n orders, a phenomenon which is further demonstrated by 6.22. It is observed that the disparity between TE11 and TM11 agrees roughly with the theoretical result described by Cahill (2015), that the optimal cross-polarisation is achieved with a TE11-TM11 mixing ratio of 85%-15%, or a linear factor of 5.67. The TM11 co-polar power lies at the -7 dB level, $\sim$ 5 dB below the TE11 co-polar power, or a factor of $\sqrt{10} \approx 3.2$. A similar level was also observed in the perfect horn, as expected, given the very low variation in the co-polar main beam. This shows that there is a greater TM11 component in the horns than would be ideal in the presence of only the HE11 mode (ideal case). In reality, the other angular modes of the n=1 order also contribute to the extinction of the cross-polar power in the ideal case, which could account for this discrepancy. Finally, the low level of power in the $m > 2$ azimuthal orders of the n=1 for the perfect horn is seen to be almost negligible, $\sim$-30 dB. This agrees with the the initial testing of limited modes shown in Fig. 6.17.

The mode amplitudes plotted in Fig. 6.21 were then input into the farfield generation and plotting algorithm adapted from PyScatter. An additional example was included for the perfect horn, using the analytical code to generate the farfield pattern. The results are shown in Fig. 6.22. The co-polar beams are seen to vary minimally above -20 dB. This is expected, as the copolar beam shape is mostly determined by the flare and mouth diameter of the horn, and will not be so easily affected by small perturbations. Nevertheless, the position of peak intensity does shift from boresight, lying within the range $\pm 1.8^\circ$ for the ten iterations performed. The cross-polar power is affected very significantly, with main lobe cross-polar peaks ranging from -16 dB to -25 dB, compared to -29 dB for the ideal horn. Additionally, the asymmetry in the cross-polarisation between the left and right (ϕ=45, 225) primary peaks is observed to be large (>5 dB in some cases). This shows that the effects of lateral displacements of stacked plates at the ± 50 μm level are extremely significant, especially in the throat of the horn, to the point of rendering most manufactured horns unfit for purpose (cross-polarisation >-25 dB in the case of QUBIC). A similar computation could be performed for the orthogonal cross-polar peaks (ϕ=135, 315), but this would be expected to return the same result. This suggests that a tolerance $\ll \pm 50\mu$m is required for good performance.

6.3.4 Final summary

This chapter has described work that was carried out to convert analytical expressions for overlap integrals in the in-house PyScatter code into numerical evaluations of the integrals. This was done so that lateral offsets between subsequent corrugations could be accommodated. The work to develop this code, called NumCross, was carried out in several stages. Firstly the power coupling integrals were represented in a form compatible with a numerical solution, with provision for lateral shifts. Upon addition of an offset, the number of cross-coupling integrals required to solve for the power scattered across a step increased significantly. The expected power levels in modes of different radial and azimuthal orders was discussed, the code was then tested against those expectations. Finally, the 176-section QUBIC horn was analysed in its entirety. This was conducted for the perfectly aligned case, and for a version including random alignment offsets at the ± 50 μm level. Machining tolerances for platelet arrays would introduce such alignment errors. The effect of the offsets was tested by comparison with the nominal horn. The results indicated that alignment of platelet sections for corrugated horns at millimetre wavelengths must be substantially better than $\pm$ 50 μm to ensure acceptable horn performance. This analysis could be performed for any waveband at which platelet stacked horns are used, and could yield much more accurate results if greater computational power were allocated to simulations

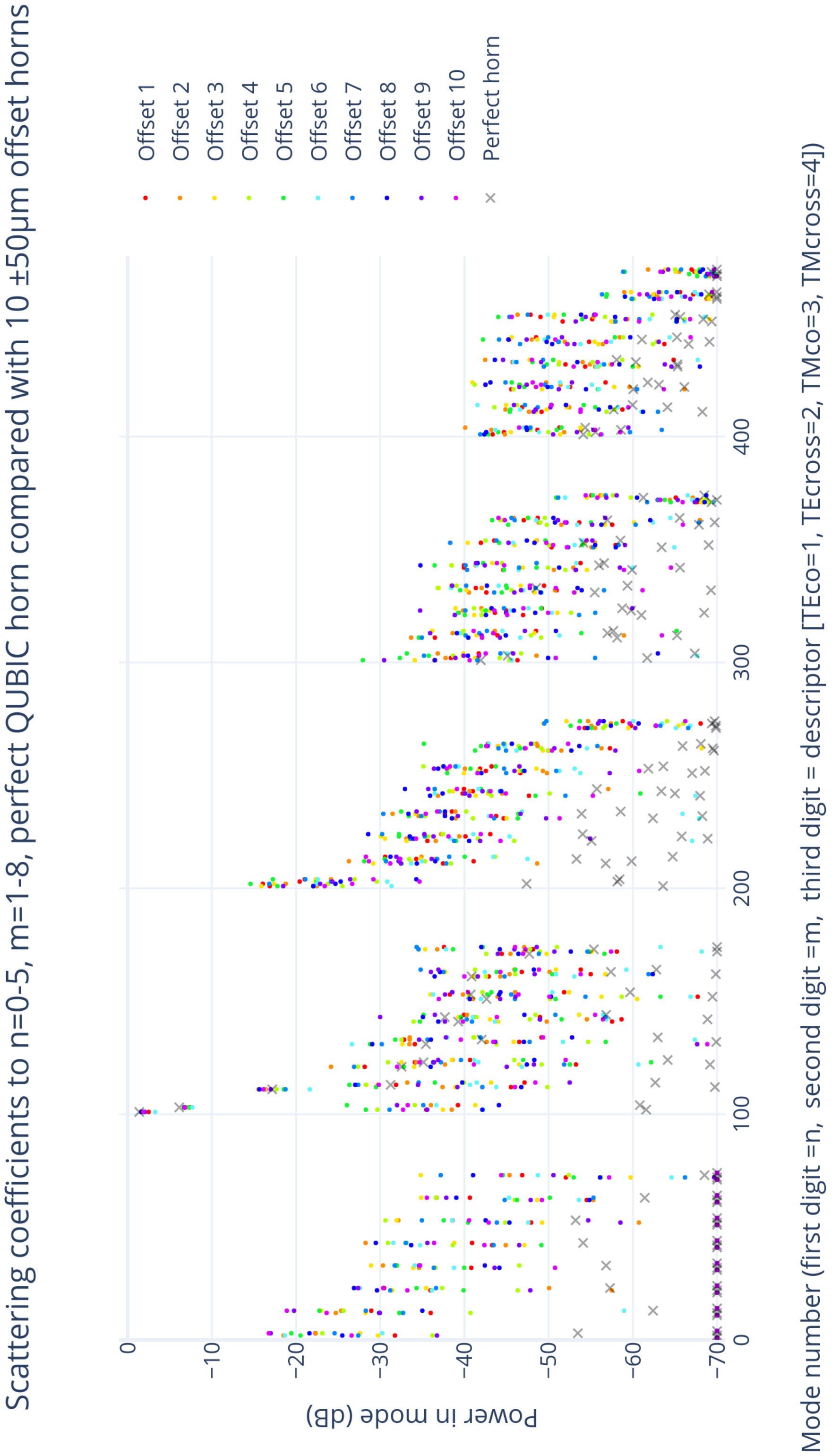

FIGURE 6.21: TE11 coupling coefficients for the full S21 at the mouth of the horn, a comparison between a perfect design and different offset levels. On the horizontal axis, for example, a value of 203 means TM20 co-polar.

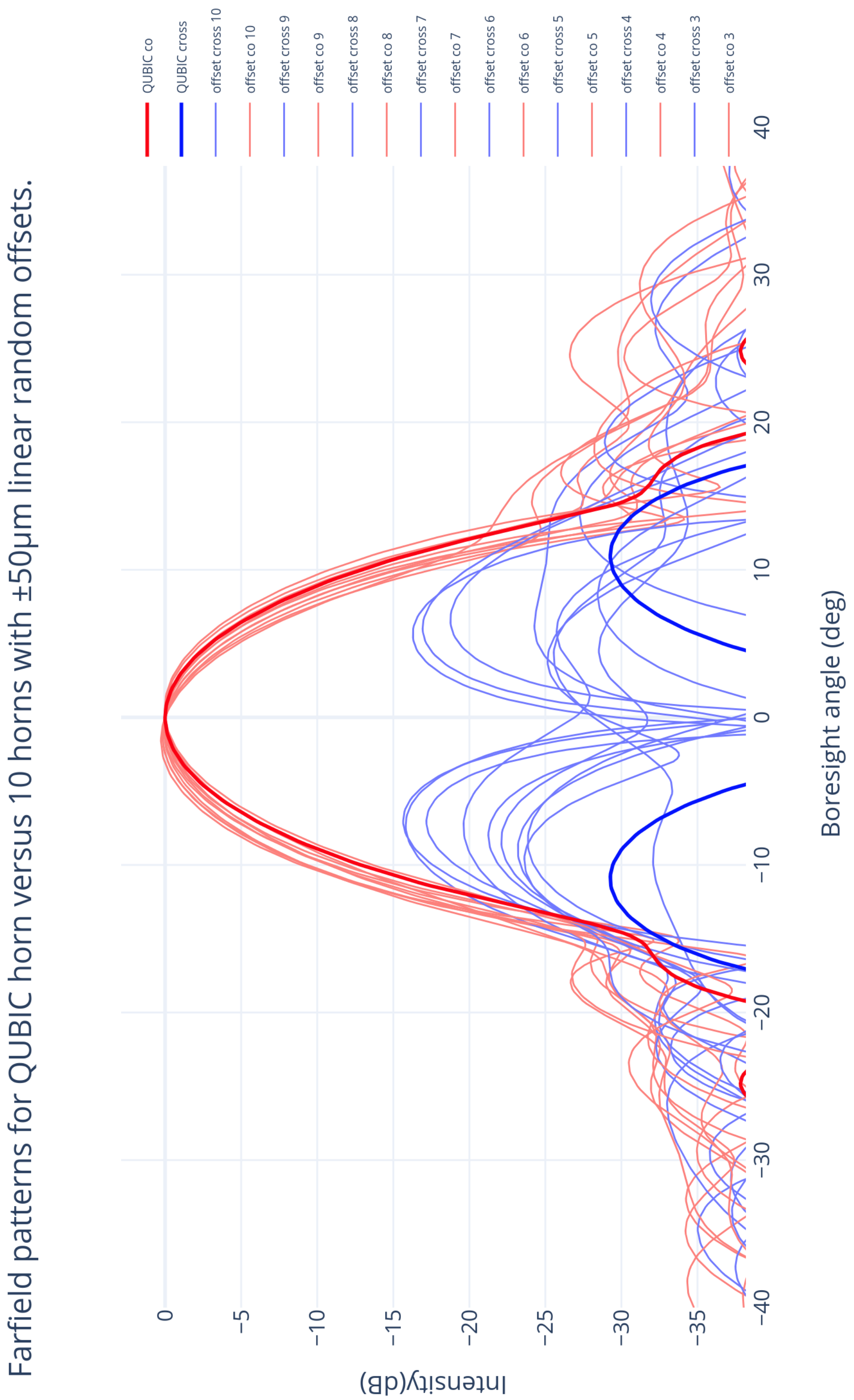

FIGURE 6.22: Comparison of the farfield pattern of the perfect QUBIC horn with patterns generated for the 10 Monte Carlo trials of the linearly offset QUBIC horn.

Chapter 7

Conclusions and Future Work

7.1 Conclusions

In this chapter I briefly summarise the work carried out in this thesis, and suggest potential future extensions of the work presented.

7.1.1 Pickmere

A Gaussian beam mode analysis was performed using Python on a simplified rendition of the Pickmere radio telescope's optical parameters. The model was tested independently using a physical optics analysis on the GRASP platform.

The beam properties evaluated using ABCD matrices and Gaussian beam mode analysis consistently agreed with the GRASP equivalent, both in the case of a free Gaussian beam and for a beam inside the telescope. The real apparatus was modelled by reflection between instantiated surfaces in GRASP, and by passage through multiple equivalent lenses in the Gaussian mode analysis.

The independent verification of beam parameters between two vastly different approaches confirms the efficacy of both methods and paves the way for further research into the use of phased arrays as proposed by our collaborators in Manchester University.

7.1.2 ALMA

A series of three wideband horns were developed for a proposed combined ALMA band 4 and 5, as well as initial prototypes for a Ka band horn which could be manufactured and tested in-house.

The beam parameter goals for the horns were challenged by manufacturing constraints and limits of the customisation of raw materials (AL plates). This allowed for more in-depth development of modelling techniques to balance these requirements.

Tolerance analysis was conducted by introducing random variations to the corrugation depths of the horn. This allowed an estimation of the expected deterioration of beam parameters for a given tolerance level, and also the spread in quality which could be expected across an array of horns. The results show that this type of analysis can be performed in a reasonable timeframe on PyScatter, and produces usable results.

7.1.3 QUBIC

The design for the QUBIC horn was used as a test for the PyScatter code. Simple alterations were made to the horn geometryto determine if the observing band could be widened to include frequencies between 90 and 150 GHz. The designs tested experienced full mode cutoff at 105 GHz, coupled with reduced performance at the upper end of the band. The QUBIC horn is manufactured using a platelet technique, any misalignment of these plates would likely result in a reduction in performance. Simulation based analysis of such offsets was not feasible using the analytical approach of PyScatter, so a new code was written using a numerical approach.

7.1.4 Numerical modelling

Proof of concept was achieved for NumCross, a numerical version of the existing analytical PyScatter routine in Python, which evaluates cross coupling integrals by summation of power over a grid of points covering the area of interest, with variable resolution. It has been demonstrated that such a routine can perform useful simulations to acceptable accuracy (<-40 dB) in a reasonable time on a standard PC (hours to several days, depending on the horn size and resolution required). The accuracy of numerical simulations of perfect horns was shown to converge incrementally toward the analytical solution as numerical resolution was increased.

NumCross was used to carry out the tolerance analysis of the QUBIC horn, by examining lateral offsets due to misalignment of platelets in plate assembly horn manufacturing. The main conclusion of this analysis was that such offsets can have a measurable effect on horn performance, specifically cross polarisation. The level of tolerancing effects on the QUBIC horn were determined to be of significance when considering horn designs.

A better knowledge of the theoretical cross polarisation and return loss from offset systems could avoid over or underengineering when the accuracy of aligning platelets for horn arrays is considered. If the level of deterioration caused by a particular fractional offset in the throat is known, then the alignment method can be tailored to the parameters needed before the horn is built. Otherwise, such effects could only be achieved by measuring the beam parameters directly from a physical horn. This is costly, both in terms of machining prototypes, and the requirement to take delicate measurements of cross-polarisation etc. It is also likely to incur higher uncertainty compared to simulation.

Numerical methods of horn analysis can constitute a valuable tool in the design of horns for array use, where individual manufacturing is impractical or prohibitively expensive. NumCross is a viable alternative to finite element techniques, which can be difficult to perform for large volume horns.

7.2 Future work

7.2.1 Overview

The research outlined in this thesis could serve as a foundation for further work in the field of THz element design and analysis, in particular for the three main projects undertaken. These are the modelling of the Pickmere radio telescope, covered in Chapter 2 the ALMA collaboration with Manchester University, as detailed in Chapter 5, and the numerical modelling undertaken in Maynooth, described in Chapter 6.

7.2.2 Pickmere

Greater computing power could be used for the GRASP analysis, allowing for inclusion of struts and other components in the full scale model, as opposed to just the main mirrors.

The Gaussian beam mode analysis code could be generalised to include an arbitrary number of simple components, with a user interface to select component parameters and positions.

7.2.3 ALMA

The design of the ALMA horns, both for bands 4-5 and for Ka band, could be extended to find the best conical horn possible, without limitations from materials and machining techniques currently available. Simulated models of the higher frequency horn indicated an ideal section width of 0.65 mm, which did not coincide with the plate thicknesses available from the supplier in the UK (0.6, 0.7 mm). Furthermore, the tolerancing on the sheets was quite poor, at $\pm 70\mu$m, although this is a guaranteed maximum, as opposed to a true uncertainty. Laser micromachining was also not as promising in terms of tolerancing as was initially hoped. Finally, the number of corrugations in horn prototypes had to be reduced considerably to meet budgeting, time and material constraints for machining. This restricted the beam parameters which could be achieved. Further research into solving these issues could yield a better prototype design.

The codes to generate geometry files and three-dimensional horn plots could be expanded to model more complex geometries of horns, for example, exponential and sine squared profiles. Combinations of these could improve cross polarisation and return loss over the linear conical designs considered for the ALMA horns.

7.2.4 Numerical modelling

The generation of the NumCross code opens up a wide variety of opportunities for straightforward and versatile analysis of horns and waveguides. Conquering the limitation of cylindrical symmetry could allow for the simulation of any system which can be broken down into circular sections along the propagation axis. The routine could also be tested at a higher accuracy and modal inclusivity, with the use of a supercomputer or cluster core processor. This would give a clearer picture of the performance and limitations of the numerical integration method used. Faster computation times could also allow analysis at many frequencies, as was conducted for ALMA using PyScatter. Finally, additional functionalities could be added, for example three-dimensional plotting of far-field patterns, and the inclusion of other sectional geometries, for example rectangular waveguides and horns.

Chapter 8

Bibliography

Ade, P. Aikin, R. Barkats, D. et al. Detection of B-Mode Polarization at Degree Angular Scales by BICEP2. Physical Review Letters Journal Volume: 112 Journal Issue: 24, June, 2014.

Ade, P. Akiba, Y. Anthony, A. et al. A measurement of the cosmic microwave background B-mode polarisation power spectrum at sub-degree scales with POLARBEAR. Astrophysical journal of the American Astronomical Society, October 2014.

Al-Azzawi, A. Physical Optics. 1st ed. Boca Raton: CRC-Taylor and Francis, pp.130-140, 2007.

Albiol, K. Navas, S. and Andres, M. Microwave experiments on electromagnetic evanescent waves and tunneling effect. American Journal of Physics - AMER J PHYS. 61. 165-169. 10.1119/1.17331, 1993.

ALMA, Antenna technology specifications. Available from https://www.almaobservatory.org /en/about-alma/ how-alma-works/technologies/antennas/ Resource created 2021, accessed 04/06/2022.

Altmann, J. Millimetre waves, lasers, acoustics for non-lethal weapons? Physics analyses and inferences. German Foundation for Peace Research, 2008.

Ascama, H. Hiramatsu, R. Oliveira, A. Dionisio, C. and Kofuji, S. Simulation and manufacturing of a miniaturized exponential UWB TEM horn antenna for UWB radar applications. Journal of Microwaves, Optoelectronics and Electromagnetic Applications, 12(2), pp.655-665, 2013.

Akiyama, K. Alberdi, A. Alef, W et al. First M87 Event Horizon Telescope Results. I. The Shadow of the Supermassive Black Hole. The Astrophysical Journal Letters, 875:L1 (17pp). April 2019

Balanis, C. Antenna Theory. Hoboken, N.J.: Wiley-Interscience, pp 137-143, 2016.

Benisha, M. Thandaiah, R. Bai, T. Evolution of Mobile Generation Technology. International Journal of Recent Technology and Engineering (IJRTE). ISSN: 2277-3878, Volume-7, Issue-5S4, February 2019.

Bennett, D. Design and analysis of a quasi-optical beam combiner for the QUBIC CMB interferometer. PhD Thesis, Maynooth University, July 2014.

Britannica, The Editors of Encyclopaedia. "Atacama Large Millimeter Array". Encyclopedia Britannica,
https://www.britannica.com/topic/Atacama-Large-Millimeter-Array.
Article created 5 Dec. 2018, accessed 3 November 2021.

Britton J. Nibarger J. Yoon K. Beall J. Becker D. Cho H. Hilton G. Hubmayr J. Niemack M. Irwin K. A Corrugated Silicon Platelet Feed Horn Array for CMB Polarimetry at 150 GHz. SPIE, Proceedings of Conference 7741, pages 249–272, July 2010.

Buchwald J.Z. Yeang, C.P. Kirchhoff's theory for optical diffraction, its predecessor and subsequent development: the resilience of an inconsistent theory, Archive for History of Exact Sciences, 2016.

Burke, D. Design and Analysis of the Optical Beam Combiner and Corrugated Feed Horns for the QUBIC Instrument. PhD Thesis, Maynooth University, 2021.

Bustos, R. Rubio, M. et al. "Parque Astronómico de Atacama: An Ideal Site for Millimeter, Submillimeter, and Mid-Infrared Astronomy". Publications of the Astronomical Society of the Pacific, Vol. 126, 2014.

Cahill, F. Design and Analysis of Corrugated Conical Horn Antennas with Terahertz Applications. PhD Thesis, Maynooth University, 2015.

Cavaliere, F. Mennella, A. et al. QUBIC VII: The feedhorn-switch system of the technological demonstrator. Instrumentation and Methods for Astrophysics. arXiv:2008.12721v2 [astro-ph.IM], Accepted for publication in the Journal of Cosmology and Astroparticle Physics, August 2020.

Clarricoats, P. J. B. and Olver, A. D. Corrugated Horns for Microwave Antennas. IEE Electromagnetic waves series, Peter Peregrinus Ltd, London, Vol 81, 1984

Crawley, D. Longbottom, C. Wallace, V. Cole, B. Arnone, D. Pepper, M. Three-dimensional terahertz pulse imaging of dental tissue. Journal of Biomedical Optics 8(2), 303–307, 2003

Committee for Radio Astronomy Frequencies (CRAF). Pickmere radio telescope. Available from
https://www.craf.eu/radio-observatories-in-europe/pickmere/
Accessed 12/02/22.

Collett, E. Field Guide to Polarization. SPIE Press, September 2005.

Crew, H. Huygens, C. Young, T. and Fresnel, A. 1900. The Wave Theory Of Light. New York: American Book Co.s, 70, 5, Sep. 2016.

Del Torto, F. Corrugated feed-horn arrays for future CMB polarization experiments, PhD Thesis, Department of Natural, Physical and Mathematical Sciences, University of Milan, 2012.

Del Torto, F. Bersanelli M. Cavaliere F. De Rosa A. D'Arcangelo O. Franceschet C. Gervasi M. Mennella A. Pagana E. Simonetto A. Tartari A. Villa F. Zannoni M. W-band prototype of platelet feed-horn array for CMB polarisation measurements. Cornell University, Journal of Instrumentation 6(06), July 2011

Diego-Palazuelos, P. Vielva, P. Herranz, D. Characterization of Extragalactic Point-Sources on E- and B-mode Maps of the CMB Polarization. Accepted for submission to JCAP, 2020.

Dobrowolski, J. Scattering Parameters in RF and Microwave Circuit Analysis and Design, Artech House, 2016.

Du Bosq, T. Lopez-Alonso, J. and Boreman, G. Millimeter wave imaging system for land mine detection, Optical Society of America, 2006.

Dutka, J. "On the Early History of Bessel Functions." Archive for History of Exact Sciences, vol. 49, no. 2, 1995.

ESO ALMA receiver band description. Available from
https://www.eso.org/public/ireland/teles-instr/alma/receiver-bands/
Resource created 2021, accessed 02/11/2021.

Fidler, C. Pettinari, G. Beneke, M. Crittenden, R. Koyama, K. Wands, D. The intrinsic B-mode polarisation of the Cosmic Microwave Background. Journal of Cosmology and Astroparticle Physics, Issue 7, 2014.

Franceschet C. del Torto F. Villa, F. Realini S. Bongiolatti R. Peverini, O. Pezzotta F. Viganó D. Addamo G. Bersanelli M. Cavaliere F. Cuttaia, F. Gervasi M. Mennella A. Morgante G. Taylor A. Virone G. Zannoni M. The LSPE-Strip feed horn array. July 2021. Preprint paper at the time of writing, available from https://www.researchgate.net/publication/353567752 _The_LSPE-Strip_feed_horn_array.
Accessed 30/8/2021.

Gaal, R. July 1816: Fresnel's Evidence for the Wave Theory of Light. American Physical Society News, 2016. 25(7).

Gallerano, G. 2004. Overview of Terahertz Radiation Sources. Proceedings of the 2004 FEL Conference, pp.216-221.

Gavdush, A. Chernomyrdin, V. Malakhov, K. Beshplav, S. Dolganova, I. Kosyrkova, A. Nikitin, P. Musina, G. Katyba, G. Reshetov, I. Cherkasova, O. Komandin, G. Karasik, V. Potapov, A. Tuchin, V. Zaytsev, K. Terahertz spectroscopy of gelatin-embedded human brain gliomas of different grades: a road toward intraoperative THz diagnosis. Journal of Biomedical Optics. Feb;24(2):1-5, 2019.

Gentili, G. Pelosi, G. Piccioli, F. On the symmetry of scattering matrix in waveguide circuits. Microwave and Optical Technology Letters, vol 61, Feb 2019, 10.1002/mop.31553

Goldsmith P.F. Quasioptical Systems: Gaussian Beam Quasioptical Propogation and Applications. IEEE Press, 1998.

Gradziel, M.Ł. et al. Modelling of the optical performance of millimeter-wave instruments in MODAL. Proc. SPIE 6472, Terahertz and Gigahertz Electronics and Photonics VI, 64720D, 1 February 2007.

Granet, C. and James, G. Design of corrugated horns: a primer. IEEE Antennas and Propagation Magazine, 47(2), pp.76-84, 2005.

Hamilton, J. Mousset, L. Zullo, A. et al. QUBIC I: Overview and Science Program. November 2020. arXiv:2011.02213v2 [astro-ph.IM]. Accepted for publication in the Journal of Cosmology and Astroparticle Physics, 2021.

Holgado, W. Sola, I. Jarque, E. & Jarabo, S. Roso, L. Q-switching in a neodymium laser. European Journal of Physics. 33. 265-278. 10.1088/0143-0807/33/2/265, 2012.

Iguchi, S. Morita, K. Sugimoto, M. Vilaro, B. Saito, M. Hasegawa, T. Kawabe, R. Tatematsu, K. Sakamoto, S. Kiuchi, H. Okumura, S. Kosugi, G. Inatani, J. Takakuwa, S. Iono, D. Kamazaki, T. Ogasawara, R. Ishiguro, M. The Atacama Compact Array (ACA). Publications of the Astronomical Society of Japan, Vol. 61, Issue 1, Pages 1–12, 25 February 2009.

Jones, D.S. The theory of electromagnetism. Pergamon Press London, 1964.

Kalinauskaite. E, Electromagnetic and Quasi-Optical Analysis of Cavity Coupled Bolometers for Far-Infrared and Terahertz Receivers. PhD Thesis, Maynooth University, 2018.

Karagoz, B. Kamburoglu, K. Altan, H. Terahertz pulsed imaging for the monitoring of dental caries: a comparison with X-ray imaging. 2017, SPIE Proceedings (Optical Society of America). Vol. 10417, id. 104170P, 2017.

Kemp, M. Taday, P. Cole, B. Cluff, J.A. Fitzgerald, A. Tribe, W. Security Applications of Terahertz Technology. Proceedings of SPIE - The International Society for Optical Engineering. Vol. 5070. 10.1117/12.500491, 2003

Kirchhoff, G. Hentschel, K. and Zhu, N. Gustav Robert Kirchhoff's Treatise "On The Theory Of Light Rays" (1882). Singapore: World Scientific Publishing Co. Pte Ltd, 2017.

Kun, M. Tu-nan, C. Tao, C. Li-guo, Z. Qiao, L. Zhao, L. Fei, L. Sen-cheng, Z. Ze-ren, L. Hua, F. Jian-heng, Z. Terahertz pulsed spectroscopy of paraffin-embedded brain glioma. Journal of Biomedical Optics; 19(7):077001, 2014.

Liddle, A. Loveday, J. The Oxford Companion to Cosmology. Oxford University Press, 2008

Li-Ming, S. Xin, L. CPW-fed multi-band omni-directional planar microstrip antenna using composite metamaterial resonators for wireless communications. Progress In Electromagnetics Research, PIER 83, 133–146, 2008.

Mandelli S. Manzan E. Mennella A. Cavaliere F. Viganò D. Franceschet C. de Bernardis P. Bersanelli M. Castellano M.G. Coppolecchia A. Cruciani A. Gervasi M. Lamagna L. Limonta A. Masi S. Paiella A. Passerini A. Pettinari G. Piacentini F. Tommasi E. Volpe A. Zannoni M. A chemically etched corrugated feedhorn array for D-band CMB observations. Experimental Astronomy 51, 249–272, February 2021.

Mandeep, J and Hilary. Effects of polarization loss factor, form factors and reader transmitting power on the range of paper and plastic UHF tags in a free and metallic environment International Journal of the Physical Sciences Vol. 6(12), pp. 2776-2781, 18 June, 2011.

Mansell, J. Praus, R. Xu, L. Seward, A. Coy, S Algorithm for Implementing an ABCD Ray Matrix Wave-Optics Propagator. SPIE Proc. Vol. 6675-16, 2007

May, R. Evans, M. Zhong, S. Warr, I. Gladden, L. Shen, Y. Zeitler, A. Terahertz in-line sensor for direct coating thickness measurement of individual tablets during film coating in real-time. Journal of Pharmaceutical Sciences Apr;100(4):1535-44, 2010.

May, A. Chapron, C. Coppi, G. D'Alessandro, G. Bernardis, P. Masi, S. Melhuish, S. Piat, M. Piccirillo, L. Schillaci, A.Thermeau, J. Ade, P. Amico, G. Auguste, D. Aumont, J. Banfi, S. Barbara, G. Battaglia, P. Battistelli, E. Zullo, A. July, 2018. Thermal architecture for the QUBIC cryogenic receiver. Millimeter, Submillimeter, and Far-Infrared Detectors and Instrumentation for Astronomy IX. Vol. 10708. International Society for Optics and Photonics, 2018.

Nagler, P. Sadleir, J. Wollack, E. Transition-edge sensor detectors for the Origins Space Telescope. Journal of Astronomical Telescopes, Instruments, and Systems. Vol. 7(1) 011005-1, January 2021.

National Institute of Standards and Technology. Photograph of the feedhorn array for the Advanced ACT receiver, Available from https://www.nist.gov/programs-projects/fabrication. Resource created 2008, accessed 14/02/2022

Olver, A. D. and Clarricoats, P. J. B. and Kishk A. A. Shafai, L. Microwave Horns and Feeds, IEEE Press, 1994

Ramakrishna, S. Anantha, R and Armour, A. "Propagating and Evanescent Waves in Absorbing Media." American Journal of Physics, vol. 71, no. 6 pp. 562–567, 10.1119/1.1557301, June 2003.

Romero, G. Large Latin American Millimeter Array. Instrumentation and Methods for Astrophysics. Science Reviews from the end of the world, Vol. 1, No. 4, pp. 34-46, September 2020.

Shchepetilnikov, A. Gusikhin, P. Muravev, V. Tsydynzhapov, G. Nefyodov, Y. Dremin, A. Kukushkin, I. New Ultra-Fast Sub-Terahertz Linear Scanner for

Postal Security Screening. Journal of Infrared, Millimeter, and Terahertz Waves volume. 41(6):1-10, 2020.

Smith, Y. Photographing a Black Hole. Available from
https://www.nasa.gov/image-feature/photographing-a-black-hole.
Resource created 2021, accessed 12/10/21.

Snitzer, E. Cylindrical Dielectric Waveguide Modes. Journal of the Optical Society of America, 51(5), p.491, 1961.

Sudhakar Rao, B. Shafai, L. et al. Handbook Of Reflector Antennas And Feed Systems. 1st ed. Artech house Antennas and Propagation Library, 2013.

Tan, C. Fletcher, P. Beach, M. Nix, AR. Landmann, M. Thomä, R. On the application of circular arrays in direction finding. Part I: Investigation into the estimation algorithms. Technical University Ilmenau, 1st Annual COST 273 Workshop, Espoo, Finland, 29-30 May 2002.

TICRA, GRASP Technical Description, 2009. Available under license from www.ticra.com.

Ufimtsev, P, and United States. Air Force. Systems Command. Foreign Technology Division. Method of Edge Waves in the Physical Theory of Diffraction. Springfield, Va. Ntis, 1980.

Ufimtsev, P. Fundamentals of the Physical Theory of Diffraction. Hoboken, NJ, Wiley, 2014.

Villa, F. Sandri, M. Mandolesi, N. Nesti, R. Bersanelli, M. SIMONETTO, A. Sozzi, C. D'Arcangelo, O. Muzzini, V. Menella, A. Guzzi, P. Radaelli, P. Fusi, R. Alippi, E. High Performance Corrugated Feed Horns for Space Applications at Millimetre Wavelengths. Experimental Astronomy. Experimental Astronomy volume 14, pp 1–15 Kluwer Academic Publishers, June 2002.

Walker, C.K. Terahertz astronomy. CRC press, ISBN 9781138894648, 2020.

Weinmann, F. Ray Tracing With PO/PTD for RCS Modeling of Large Complex Objects. IEEE Transactions on Antennas and Propagation, 54(6), pp.1797-1806, 2006.

Willumson, S. Process time optimization of robotic remote laser cutting by utilizing customized beam patterns and redundancy space task sequencing. ROBOCUT project, PhD Thesis, Aalborg University, 2016.

Wilmink, G. J. and Grundt, J. E. Invited review article: Current state of research on biological effects of terahertz radiation. Journal of infrared, millimeter and terahertz waves, 32(10), pp. 1074–1122, 2011.

Yagoubov, P. Mroczkowski, T. Testi, L. De Breuck C. Gonzalez, A. Kaneko, K. Uzawa, Y. Molina, R. Tapia, V. Reyes, N. Mena, P. Beltran, M. Nesti, R. Cuttaia, F. Ricciardi S. Sandri, M. Terenzi, L. Villa, F. Murk, A. Kotiranta, M. McGenn, W. Cuadrado-Calle, D. Fuller, G. A. George, D. Gallego, J. D. Lapkin, I. Fredrixon, M. Belitsky, V. Wideband 67-116 GHz cryogenic receiver development for ALMA Band 2. Astronomy and Astrophysics, Volume 634, id.A46, pp 22.

Yngvesson, S. Bardin, J. Real time breast cancer cell detection with Terahertz. University of Massachusetts Institute for Applied Life Sciences, 2021. Available from https://www.umass.edu /cphm/content/
real-time-breast-cancer-cell-detection-terahertz. Accessed 20/09/21.

Zaman, A. Matin, A and Gaffar, M. An Optimized Ku-Band Corrugated Feed Horn Antenna Design for a Cassegrain Reflector Using Multi-Objective Particle Swarm Optimization. WSEAS Transactions on Communications 10(12) pp 364-373, 2011.

Appendix A

Pickmere Schematics

These schematics formed the basis of the dimensions used in the GRASP model of Pickmere. They were obtained by personal correspondence from the Manchester team.

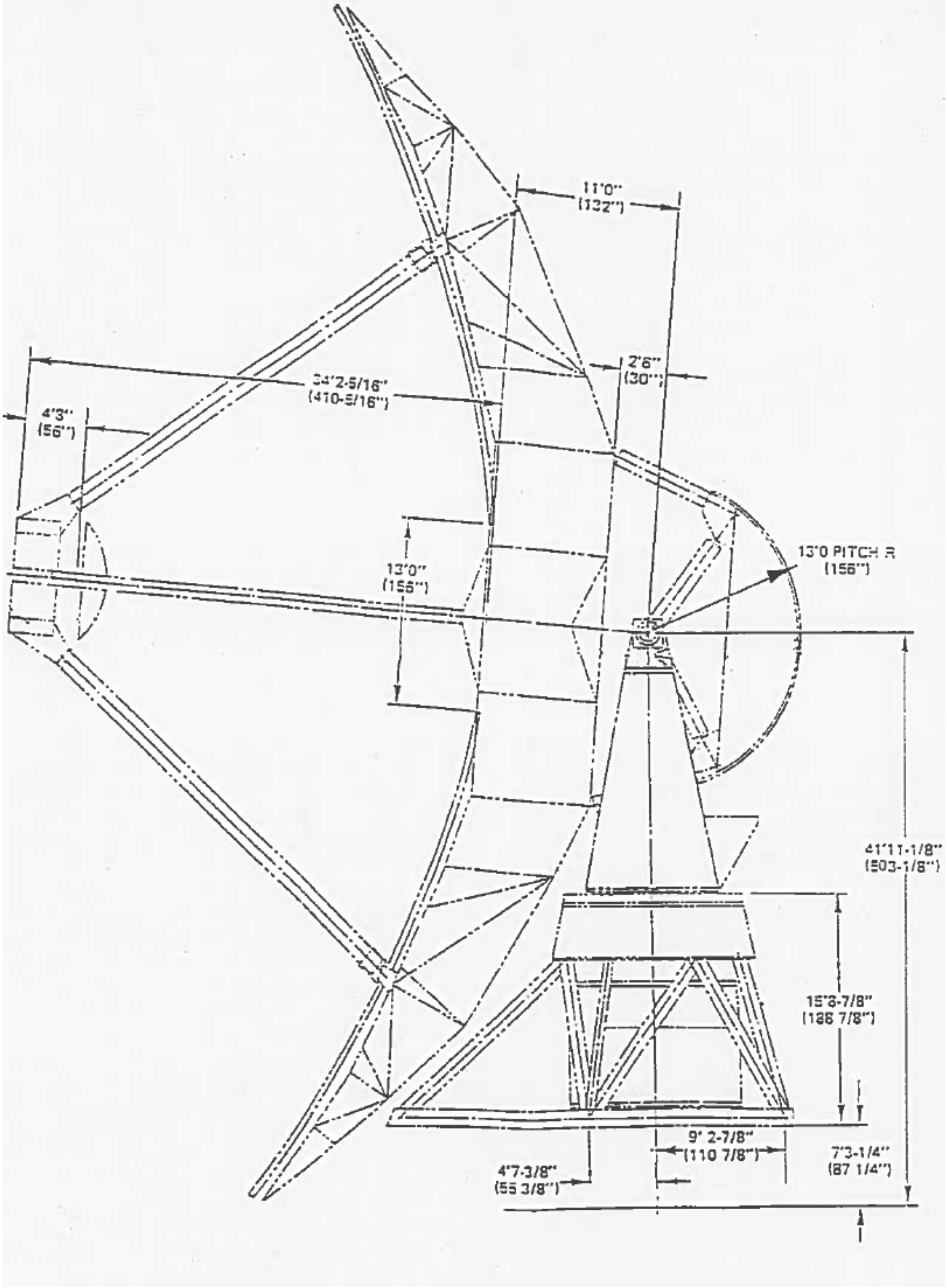

FIGURE A.1: Initial design of the Pickmere radio telescope, with mount

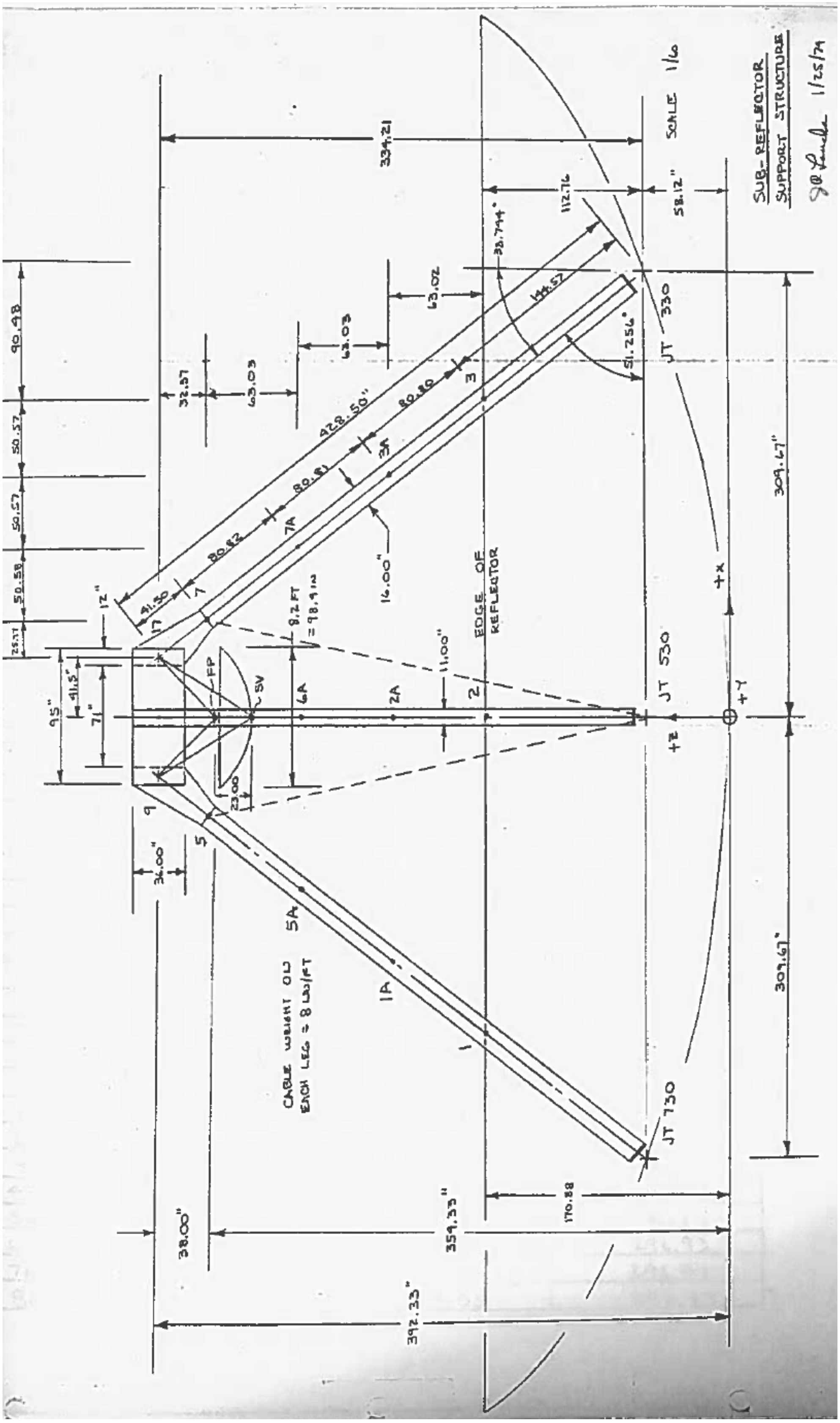

FIGURE A.2: Dimensions of the reflectors, struts and armature

Appendix B

PyScatter excerpt, calculating P, Q and R matrices

This appendix contains an example section of the PyScatter code described in Chapters 4, 5 and 6, specifically the part which performs the mode matching integrations and generates the P, Q nd R matrices.

This code was developed from the cross-coupling integration. This routine written by David Burke as part of his doctoral degree, (Burke, 2021), based on mode matching mathematics compiled by Eimante Kalinauskaite as part of her doctoral degree (Kalinauskaite, 2017).

B.1 Cell 1

```
from datetime import datetime
start_time = datetime.now()

def frange(start,stop, step):
    while start <= stop:
        yield start
        start +=step

logcrossset=[]

for freq in frange (FStart,FEnd,FStep):
    #Setting up constants
    c=299792458
    L=(c/(freq * pow(10,9)))*pow(10,3)

    # Wavenumber
    def k0(L):
        return (2 * pi)/L
    # Propagation function
    def beta(z):
        return conjugate(sqrt(1 - pow((z / k0(L)),2)))

    #Creating a table of Bessel derivative roots
```

```
pnlds =[]
for n in range(var1,var2 + 1):
    for l in range(1,var3 + 1):
        pnld = jnp_zeros(n,l)
    pnlds.append(pnld)

#Creating a table of Bessel roots
pnls = []
for n in range(var1,var2 + 1):
    for l in range(1,var3 + 1):
        pnl = jn_zeros(n,l)
    pnls.append(pnl)

index1=[]
index2=[]


LLinit = sections_lengths[0]
a0 = sections_radii[0]
#Defining the initial propagation matrices
def VijTEInit(n,x):
    return exp(complex(0,-1)*k0(L)*beta((pnlds[n][x-1])/a0)*LLinit)
def VijTMInit(n,x):
    return exp(complex(0,-1)*k0(L)*beta((pnls[n][x-1])/a0)*LLinit)
k00 = k0(L)
import numpy as np
VIJTEINIT = [[exp(complex(0,-1)*k00*beta((pnlds[n][x-1])/a0)*LLinit)
for x in range(1,var3+1)] for n in range (var1,var2+1)]
VIJTMINIT = [[exp(complex(0,-1)*k00*beta((pnls[n][x-1])/a0)*LLinit)
for x in range(1,var3+1)] for n in range (var1,var2+1)]
VijTEMatInit = np.array(list(VIJTEINIT))
VijTMMatInit = np.array(list(VIJTMINIT))
VijTETMINIT = [np.vstack((VijTEMatInit[n],VijTMMatInit[n]))
for n in range (var1, var2+1)]
VINIT = [np.diag(VijTETMINIT[n].flatten()) for n in range (var1,var2+1)]

b = a0
LL=LLinit
IdentityMatrix = np.identity(2*var3)
S21a = [(np.dot(VINIT[n],IdentityMatrix)) for n in range (var1, var2+1)]
S12a = S21a
S11a = (np.zeros(shape=(2*var3,2*var3)))
S22a = S11a



for index in range (0,len(sections_radii)-1):
    a = b
    b = sections_radii[index+1]
    delLL=sections_lengths[index+1]
    LL = delLL + LL
    if a > b:
        rbig = a
        rsmall = b
    if b > a:
        rbig = b
        rsmall = a
```

```
# Populating arrays of dimensions "n x i x j" with analytical solutions to cross-coupling integrals
PTETE = [[[(-1 * sqrt(1 / (pow(rsmall,2) * (1 - (pow(n / pnlds[n][i-1],2)))
        * pow(jv(n,pnlds[n][i-1]),2)))) * sqrt(1 / (pow(rbig,2) * (1 - (pow(n / pnlds[n][j-1],2)))
        *pow(jv(n,pnlds[n][j-1]),2))) * conjugate(beta(pnlds[n][j-1] / rbig)) * (2 *
        pnlds[n][i-1] * jv(n,pnlds[n][i-1]) * jvp(n,(pnlds[n][j-1] * rsmall) / rbig)) / (
        pow((pnlds[n][j-1] / rbig),2) - (pow((pnlds[n][i-1] / rsmall),2))) *
        ((1 / (sqrt(abs(beta(pnlds[n][j-1] / rbig)))))
        * (1 / (sqrt(abs(beta(pnlds[n][i-1] / rsmall)))))) for j in range(1,var3+1)]
        for i in range(1,var3+1)] for n in range(var1,var2+1)]

PTMTM = [[[(1 * sqrt(1 / (pow(rsmall,2) * pow(rbig,2) * (pow(jv((n+1),pnls[n][i-1]),2)
        ) * pow(jv((n+1),pnls[n][j-1]),2)))) * (2 * ((rsmall * pnls[n][j-1]) / rbig) * (
        jvp(n,pnls[n][i-1])) * jv(n,(pnls[n][j-1] * rsmall) / rbig)) / (
        pow((pnls[n][j-1]) / rbig,2) - pow((pnls[n][i-1]) / rsmall,2)) * 1 / (
        conjugate(beta(pnls[n][j-1] / rbig))) * ((sqrt(abs(beta(pnls[n][j-1] / rbig)))) * (
        sqrt(abs(beta(pnls[n][i-1] / rsmall))))) for j in range(1,var3+1)]
        for i in range(1,var3+1)] for n in range(var1,var2+1)]

PTETM = [[[ (1 * sqrt(1 / ((1 - (pow(n / pnlds[n][i-1],2))) * pow(jv(n,pnlds[n][i-1]),2))
        )) * sqrt(1 / (((pow(jv((n+1) , pnls[n][j-1]),2))))) * (2 * n) * jv(n,pnlds[n][i-1]
        ) * (jv(n,(pnls[n][j-1] * rsmall) / rbig) / (pnlds[n][i-1] * pnls[n][j-1])) * (
        1/(conjugate(beta((pnls[n][j-1]) / rbig)))) * (sqrt(abs(beta(pnls[n][j-1] / rbig)) / abs(
        beta(pnlds[n][i-1] / rsmall))))
        for j in range(1,var3+1)]for i in range(1,var3+1)] for n in range(var1,var2+1)]

PTMTE = [[[0 for j in range(1,var3+1)]for i in range(1,var3+1)] for n in range(var1,var2+1)]

QijTETE = [[conjugate(beta(pnlds[n][i-1] / rbig))*(1 / abs(beta(pnlds[n][i-1] / rbig)))
        for i in range(1,var3+1)] for n in range(var1,var2+1)]

QijTMTM = [[1 / (conjugate(beta(pnls[n][i-1] / rbig))) * abs(beta(pnls[n][i-1] / rbig))
        for i in range(1,var3+1)] for n in range(var1, var2+1)]

RijTETE = [[conjugate(beta(pnlds[n][i-1] / rsmall))*(1 / abs(beta(pnlds[n][i-1] / rsmall)))
        for i in range(1,var3+1)] for n in range(var1,var2+1)]

RijTMTM = [[1 / (conjugate(beta(pnls[n][i-1] / rsmall))) * abs(beta(pnls[n][i-1] / rsmall))
        for i in range(1,var3+1)] for n in range(var1, var2+1)]

#generating propagation matrices
def VijTE(n,x):
    return exp(complex(0,-1)*k0(L)*beta((pnlds[n][x-1])/b)*delLL)
def VijTM(n,x):
    return exp(complex(0,-1)*k0(L)*beta((pnls[n][x-1])/b)*delLL)
k00 = k0(L)
VIJTE = [[exp(complex(0,-1)*k00*beta((pnlds[n][x-1])/b)*delLL)
for x in range(1,var3+1)] for n in range (var1,var2+1)]
VIJTM = [[exp(complex(0,-1)*k00*beta((pnls[n][x-1])/b)*delLL)
for x in range(1,var3+1)] for n in range (var1,var2+1)]

PteteMat = np.array(list(PTETE))
PtetmMat = np.array(list(PTETM))
PtmteMat = np.array(list(PTMTE))
PtmtmMat = np.array(list(PTMTM))

QteteMat = np.array(list(QijTETE))
QtmtmMat = np.array(list(QijTMTM))
```

```
RteteMat = np.array(list(RijTETE))
RtmtmMat = np.array(list(RijTMTM))
Qtetetmtm = [np.vstack((QteteMat[n],QtmtmMat[n])) for n in range (var1, var2+1)]
Rtetetmtm = [np.vstack((RteteMat[n],RtmtmMat[n])) for n in range (var1, var2+1)]
#producing finished P, Q and R matrices
QQij = [np.diag(Qtetetmtm[n].flatten()) for n in range (var1, var2+1)]
RRij = [np.diag(Rtetetmtm[n].flatten()) for n in range (var1,var2+1)]
PPij = [np.vstack((np.hstack((np.transpose(PteteMat[n]),np.transpose(PtmteMat[n])))
,np.hstack((np.transpose(PtetmMat[n]),np.transpose(PtmtmMat[n])))))


PPij = [np.vstack((np.hstack((np.transpose(PteteMat[n]),np.transpose(PtmteMat[n])))\\
,np.hstack((np.transpose(PtetmMat[n]),np.transpose(PtmtmMat[n]))))) for n in range (var1, var2+1)]


VijTEMat = np.array(list(VIJTE))
VijTMMat = np.array(list(VIJTM))
VijTETM = [np.hstack((VijTEMat[n],VijTMMat[n])) for n in range (var1, var2+1)]
Vij = [np.diag(VijTETM[n].flatten()) for n in range (var1,var2+1)] #propagation phase matrix
```

Appendix C

NumCross excerpt, calculating P, Q and R matrices

This appendix contains an example section of the NumCross code described in Chapter 6, specifically the part which performs the mode matching integrations and generates the P, Q nd R matrices

C.1 Cell 1

```
import numpy as np
import matplotlib.pyplot as plt
import scipy.special
import math as mth
from mpl_toolkits.mplot3d import Axes3D
import cmath as cm
import time
import datetime
from datetime import datetime
import random as rnd

#shorthand for trig functions

pi=np.pi
sin=np.sin
cos=np.cos
sqrt=np.sqrt
tan=np.tan
tan2=mth.atan2

#timer
start=datetime.now()

#inputting and reading geometry files
lines = np.loadtxt("QUBICtest.txt", comments="#", delimiter=",", unpack=False)
section_number = lines[2];
sections_lengths = lines[3:(len(lines)-(len(lines)/2)+1)]
sections_radii = lines[(len(lines)-(len(lines)/2)+1):len(lines)];
print section_number, sections_lengths, sections_radii

lines2=np.loadtxt("QUBICtestoffset0.1.txt", comments="#", delimiter=",", unpack=False)



rawoffsetx=lines2[0:len(lines2)/2]
rawoffsety=lines2[len(lines2)/2:len(lines2)]

offsetx=[]
offsety=[]
deloffsetx=[]
deloffsety=[]
#Setting up offsets
```

```
for i in range (int(section_number)):
    offsetx.append(rnd.gauss(sections_radii[i], rawoffsetx[i]))
    offsety.append(rnd.gauss(sections_radii[i], rawoffsety[i]))
for i in range (int(section_number)):
    deloffsetx.append (offsetx[i]-sections_radii[i])
    deloffsety.append (offsety[i]-sections_radii[i])

print "offsetx", deloffsetx

print "offsety", deloffsety

print np.max(deloffsetx)
print np.max(deloffsety)
#unit conversion
for i in range (int(section_number)):
    offsetx[i]=offsetx[i]/1000
    offsety[i]=offsety[i]/1000
    deloffsetx[i]=deloffsetx[i]/1000
    deloffsety[i]=deloffsety[i]/1000
```

C.2 Cell 2

```
#number of  modes to be analysed
m=10
n=1
#side length of resultant matrices
x1=2*int(2*m*(n+1))



#Initial propagation matrices
Vij11initmatrix=np.zeros((x1, x1),dtype=complex)
Vij22initmatrix=np.zeros((x1, x1),dtype=complex)
Vij12initmatrix=np.zeros((x1, x1),dtype=complex)
Vij21initmatrix=np.zeros((x1, x1),dtype=complex)
Vijinitlist=[]
Vij11finalmatrix=np.zeros((x1, x1),dtype=complex)
Vij22finalmatrix=np.zeros((x1, x1),dtype=complex)
Vij12finalmatrix=np.zeros((x1, x1),dtype=complex)
Vij21finalmatrix=np.zeros((x1, x1),dtype=complex)
Vijfinallist=[]

#Constants
omega=2*pi*2*10**11
lamb=(2*pi*300000000)/omega
k0=2*pi/lamb
#Plotting resolution
res=100
r= 9  #rounding factor

#intrinsic impedance of free space
Z0=1.0
mu0=1.2567*10**-6
ep0=8.854*10**-12


asmalllist=[]
abiglist=[]
aproplist=[]


for sect in range (int(section_number-1)):
   #creating radii and length sections for integration
    dL=sections_lengths[sect]/1000
    dLinit=sections_lengths[0]/1000
    dLfinal=sections_lengths[-1]/1000
    ae=sections_radii[sect]  #radius of the cavity
    am=sections_radii[sect+1]


    ae=ae/1000
    am=am/1000
```

```
    #determining the sizes of the waveguide sections across the step.

if am>=ae:
    xe=np.linspace(-ae+deloffsetx[sect],ae+deloffsetx[sect],res+1) #offsetae
    ye=np.linspace(-ae+deloffsety[sect],ae+deloffsety[sect],res+1) #offsetae
    xm=np.linspace(-ae+deloffsetx[sect+1],ae+deloffsetx[sect+1],res+1) #+offsetam
    ym=np.linspace(-ae+deloffsety[sect+1],ae+deloffsety[sect],res+1) #offsetam#

    asmall=ae
    abig=am
    asmalllist.append(asmall)
    abiglist.append(abig)


if am<ae:
    xe=np.linspace(-am+deloffsetx[sect+1],am+deloffsetx[sect+1],res+1) #offsetam
    ye=np.linspace(-am+deloffsetx[sect+1],am+deloffsetx[sect+1],res+1) #offsetam
    xm=np.linspace(-am+deloffsetx[sect],am+deloffsetx[sect],res+1) #+offsetae
    ym=np.linspace(-am+deloffsety[sect],am+deloffsety[sect],res+1) #offsetae

    asmall=am
    abig=ae
    asmalllist.append(asmall)
    abiglist.append(abig)
stepe=(2*asmall)/res
stepm=(2*asmall)/res
aprop=sections_radii[sect]/1000

#initial and final sections
apropinit=sections_radii[0]/1000
apropfinal=sections_radii[-1]/1000
aproplist.append(aprop)

#function to calculate Bessel roots
def pnm(n,m):
    return scipy.special.jn_zeros(n,m)[m-1]
 #roots of first derivatives of Bessel fucntions
def pnmd(n,m):
    return scipy.special.jnp_zeros(n,m)[m-1]


#this function calculates the impedance values for the horn
def impedance(n,m,a):

    ztenm=Z0/(cm.sqrt(1.0-(pnmd(n,m)/(omega*a*sqrt(mu0*ep0)))**2))
    ztmnm=Z0*cm.sqrt(1.0-(pnm(n,m)/(omega*a*sqrt(mu0*ep0)))**2)

    return ztmnm, ztenm
    #Computing bets
def beta(n,m,a):
    betatmnm=1.0*np.conj(cm.sqrt(1.0-(pnm(n,m)/(k0*a))**2))
    betatenm=1.0*np.conj(cm.sqrt(1.0-(pnmd(n,m)/(k0*a))**2))

    return betatmnm, betatenm


#this function integrates the Poynting vector over offset pairs of waveguide sections.
def mode(nnumber, mnumber):
    starttime=datetime.now()
    dummy=0
    timer1=0.0
    timer2=0.0
    counter=0.0
    totalpower=0.0
    m1=np.linspace(1, mnumber, mnumber)
    n1=np.linspace(0, nnumber, nnumber+1)

    #Cresting empty lists and matrices to fill durng the routine.
    Qlist=[]
    Rlist=[]
    betalist=[]
    Vijlist=[]
    Qmatrix=np.zeros((x1, x1),dtype=complex)
    Rmatrix=np.zeros((x1, x1),dtype=complex)
    Vij11matrix=np.zeros((x1, x1),dtype=complex)
    Vij22matrix=np.zeros((x1, x1),dtype=complex)
    Vij12matrix=np.zeros((x1, x1),dtype=complex)
```

```
Vij21matrix=np.zeros((x1, x1),dtype=complex)
Identitymatrix=np.identity(x1)
#cycling through all included radial and angular modes.
for nvar1 in range(0,len(n1)):

    for mvar1 in range(len(m1)):

        for nvar2 in range(0,len(n1)):
            for mvar2 in range(len(m1)):
                pline=[]
                pline2=[]
                pline3=[]
                pline4=[]


                if ae<=am:
                        asmall=ae
                        abig=am
                if ae>am:

                        asmall=am
                        abig=ae


                pnmvalE=pnm(int(n1[nvar1]),int(m1[mvar1]))
                pnmdvalE=pnmd(int(n1[nvar1]),int(m1[mvar1]))
                pnmvalH=pnm(int(n1[nvar2]),int(m1[mvar2]))
                pnmdvalH=pnmd(int(n1[nvar2]),int(m1[mvar2]))
                #calculating impedances
                ztmnmE, ztenmE =impedance(int(n1[nvar1]),int(m1[mvar1]),asmall)
                ztmnmH, ztenmH =impedance(int(n1[nvar2]),int(m1[mvar2]),abig)




                betatmnmH, betatenmH=beta(int(n1[nvar2]),int(m1[mvar2]),abig)

                betatmprop, betateprop=beta(int(n1[nvar1]),int(m1[mvar1]),aprop)

                betatmpropinit, betatepropinit=beta(int(n1[nvar1]),int(m1[mvar1]),apropinit)

                betatmpropfinal, betatepropfinal=beta(int(n1[nvar1]),int(m1[mvar1]),apropfinal)


                if mvar2==0 and nvar2==0 and sect !=0:
                    Vije=np.exp(complex(0,-1)*k0*betateprop*dL)
                    Vijm=np.exp(complex(0,-1)*k0*betatmprop*dL)


                    Vijlist.append(Vije)
                    Vijlist.append(Vije)
                    Vijlist.append(Vijm)
                    Vijlist.append(Vijm)
                if sect==0 and mvar2==0 and nvar2==0:
                    #Generating the initial and final propagation matrices
                    Vijeinit=np.exp(complex(0,-1)*k0*betatepropinit*dLinit)
                    Vijminit=np.exp(complex(0,-1)*k0*betatmpropinit*dLinit)
                    Vijefinal=np.exp(complex(0,-1)*k0*betatepropfinal*dLfinal)
                    Vijmfinal=np.exp(complex(0,-1)*k0*betatmpropfinal*dLfinal)

                    Vijinitlist.append(Vijeinit)
                    Vijinitlist.append(Vijeinit)
                    Vijinitlist.append(Vijminit)
                    Vijinitlist.append(Vijminit)

                    Vijfinallist.append(Vijefinal)
                    Vijfinallist.append(Vijefinal)
                    Vijfinallist.append(Vijmfinal)
                    Vijfinallist.append(Vijmfinal)


                deltan0e=0
                deltan0m=0
                if int(n1[nvar1])==0:
                    deltan0e=1
                if int(n1[nvar2])==0:
                    deltan0m=1
                exhtot=[0,0,0,0,0,0,0,0,0,0,0,0,0,0,0,0]
```

```
for i in range(len(xe)):


    for j in range(len(ye)):



    #Performing the numerical integration
        n=int(n1[nvar1])
        #coordinate conversion




            #Coordinate convrsion
        r1=(sqrt((xe[i]/asmall)**2+(ye[j]/asmall)**2))
        phi1=(tan2(ye[j],xe[i]))




        #these functions are separated out to neaten the equations
        const=(2-deltan0e)/(4.0*pi*asmall**2)
        J1E=scipy.special.jv(n-1,(pnmvalE*r1))
        J2E=scipy.special.jv(n+1,(pnmvalE*r1))
        J3E=scipy.special.jv(n-1,pnmvalE)**2
        J4E=1-(n/pnmdvalE)**2
        J5E=scipy.special.jv(n+1,(pnmdvalE*r1))
        J6E=scipy.special.jv(n-1,(pnmdvalE*r1))
        J7E=scipy.special.jv(n,pnmdvalE)**2
        #Fully written out equation, as an example
        #exteco=cm.sqrt((2-deltan0)/(4.0*pi*a**2)/(1-(n/pnmdval)**2*scipy.special.jv(n,pnmdval)**2)) *
        #(scipy.special.jv(n+1,(pnmdval*(sqrt((i/a)**2+(j/a)**2))))*cos((n-1)*(tan2(i,j)))
        # +scipy.special.jv(n+1,(pnmdval*(sqrt((i/a)**2+(j/a)**2))))*cos((n+1)*(tan2(i,j))))*sqrt(abs(ztenmE))

        #Electric cross coupling equations
        exteco=cm.sqrt(const/(J4E*J7E)) * (J6E*cos((n-1)*phi1)+J5E*cos((n+1)*phi1))*sqrt(abs(ztenmE))
        extecross=cm.sqrt(const/(J4E*J7E)) * (J6E*-sin((n-1)*phi1)+J5E*-sin((n+1)*phi1))*sqrt(abs(ztenmE))
        eyteco=-cm.sqrt(const/(J4E*J7E)) * (J6E*sin((n-1)*phi1)-J5E*sin((n+1)*phi1))*sqrt(abs(ztenmE))
        eytecross=-cm.sqrt(const/(J4E*J7E)) * (J6E*cos((n-1)*phi1)-J5E*cos((n+1)*phi1))*sqrt(abs(ztenmE))
        extmco=cm.sqrt(const/(J3E)) * (J1E*cos((n-1)*phi1)-J2E*cos((n+1)*phi1))*sqrt(abs(ztmnmE))
        extmcross=cm.sqrt(const/(J3E)) * (J1E*-sin((n-1)*phi1)-J2E*-sin((n+1)*phi1))*sqrt(abs(ztmnmE))
        eytmco=-cm.sqrt(const/J3E) * (J1E*sin((n-1)*phi1)+J2E*sin((n+1)*phi1))*sqrt(abs(ztmnmE))
        eytmcross=-cm.sqrt(const/J3E) * (J1E*cos((n-1)*phi1)+J2E*cos((n+1)*phi1))*sqrt(abs(ztmnmE))

        n=int(n1[nvar2])
        r2=(sqrt((xm[i]/abig)**2+(ym[j]/abig)**2))
        phi2=(tan2(ym[j],xm[i]))

        #these functions are separated out to neaten the equations
        const=(2-deltan0m)/(4.0*pi*abig**2)
        J1H=scipy.special.jv(n-1,(pnmvalH*r2))
        J2H=scipy.special.jv(n+1,(pnmvalH*r2))
        J3H=scipy.special.jv(n-1,pnmvalH)**2
        J4H=1-(n/pnmdvalH)**2
        J5H=scipy.special.jv(n+1,(pnmdvalH*r2))
        J6H=scipy.special.jv(n-1,(pnmdvalH*r2))
        J7H=scipy.special.jv(n,pnmdvalH)**2

         #Magnetic cross coupling equations
        hxteco=(1/ztenmH)*cm.sqrt(const/(J4H*J7H)) * (J6H*sin((n-1)*phi2)-J5H*sin((n+1)*phi2))*sqrt(abs(ztenmH))
        hxtecross=(1/ztenmH)*cm.sqrt(const/(J4H*J7H)) * (J6H*cos((n-1)*phi2)-J5H*cos((n+1)*phi2))*sqrt(abs(ztenmH))
        hyteco=(1/ztenmH)*cm.sqrt(const/(J4H*J7H)) * (J6H*cos((n-1)*phi2)+J5H*cos((n+1)*phi2))*sqrt(abs(ztenmH))
        hytecross=(1/ztenmH)*cm.sqrt(const/(J4H*J7H)) * (J6H*-sin((n-1)*phi2)+J5H*-sin((n+1)*phi2))*sqrt(abs(ztenmH))
        hxtmco=(1/ztmnmH)*cm.sqrt(const/(J3H)) * (J1H*sin((n-1)*phi2)+J2H*sin((n+1)*phi2))*sqrt(abs(ztmnmH))
        hxtmcross=(1/ztmnmH)*cm.sqrt(const/(J3H)) * (J1H*cos((n-1)*phi2)+J2H*cos((n+1)*phi2))*sqrt(abs(ztmnmH))
        hytmco=(1/ztmnmH)*cm.sqrt(const/(J3H)) * (J1H*cos((n-1)*phi2)-J2H*cos((n+1)*phi2))*sqrt(abs(ztmnmH))
        hytmcross=(1/ztmnmH)*cm.sqrt(const/(J3H)) * (J1H*-sin((n-1)*phi2)-J2H*-sin((n+1)*phi2))*sqrt(abs(ztmnmH))

        #calculating Poynting from cross product of components
        exhtetecoco=((exteco*hyteco)-(eyteco*hxteco))
        exhtetecocross=((exteco*hytecross)-(eyteco*hxtecross))   #abs(z)/z
        exhtetecrossco=((extecross*hyteco)-(eytecross*hxteco))
        exhtetecrosscross=((extecross*hytecross)-(eytecross*hxtecross))
        exhtetmcoco=((exteco*hytmco)-(eyteco*hxtmco))
        exhtetmcocross=((exteco*hytmcross)-(eyteco*hxtmcross))
        exhtetmcrossco=((extecross*hytmco)-(eytecross*hxtmco))
        exhtetmcrosscross=((extecross*hytmcross)-(eytecross*hxtmcross))
```

```
                exhtmtecoco=((extmco*hyteco)-(eytmco*hxteco))
                exhtmtecocross=((extmco*hytecross)-(eytmco*hxtecross))
                exhtmtecrossco=((extmcross*hyteco)-(eytmcross*hxteco))
                exhtmtecrosscross=((extmcross*hytecross)-(eytmcross*hxtecross))
                exhtmtmcoco=((extmco*hytmco)-(eytmco*hxtmco))
                exhtmtmcocross=((extmco*hytmcross)-(eytmco*hxtmcross))
                exhtmtmcrossco=((extmcross*hytmco)-(eytmcross*hxtmco))
                exhtmtmcrosscross=((extmcross*hytmcross)-(eytmcross*hxtmcross))

                #creating coordinate points for plotting
                D=sqrt(xe[i]**2+ye[j]**2)

                #creating unit cell to store values pertaining to the interaction of a single pair of modes
                basiccell=np.zeros((4,4), dtype=complex)

                if D<asmall:

                    exhtot[0]+=exhtetecoco
                    exhtot[1]+=exhtetecocross
                    exhtot[2]+=exhtetmcoco
                    exhtot[3]+=exhtetmcocross
                    exhtot[4]+=exhtetecrossco
                    exhtot[5]+=exhtetecrosscross
                    exhtot[6]+=exhtetmcrossco
                    exhtot[7]+=exhtetmcrosscross
                    exhtot[8]+=exhtmtecoco
                    exhtot[9]+=exhtmtecocross
                    exhtot[10]+=exhtmtmcoco
                    exhtot[11]+=exhtmtmcocross
                    exhtot[12]+=exhtmtecrossco
                    exhtot[13]+=exhtmtecrosscross
                    exhtot[14]+=exhtmtmcrossco
                    exhtot[15]+=exhtmtmcrosscross



        pixnum=stepe**2
        exhnorm=[0,0,0,0,0,0,0,0,0,0,0,0,0,0,0,0]
        #dividing the total pixel value for the mode by the number of pixels computed.

        for q in range(len(exhtot)):
            im=0.0
            re=0.0
            exhnorm[q]=exhtot[q]*pixnum
            re=0.0+np.round(np.real(exhnorm[q]), r)
            if abs(np.round(np.imag(exhnorm[q]), r))>1/10**r:
                im=np.round(np.imag(exhnorm[q]), r)
                exhnorm[q]=re+(im*1j)
            else:
                exhnorm[q]=re
            totalpower+=exhnorm[q]

        Appending values to the unit cell
        for b1 in range (4):
            for b2 in range (4):
                basiccell[b1, b2]= exhnorm[4*b1+b2]


        #Appending the 4x4 unit cell to the larger matrix
        if nvar2==0 and mvar2==0:
            Pmatrix1=basiccell

        else:
            Pmatrix1= np.concatenate((Pmatrix1, basiccell), axis=1)


        if nvar1==nvar2 and mvar1==mvar2:

            Rlist.append(abs(ztenmE)/ztenmE)
            Rlist.append(abs(ztenmE)/ztenmE)
            Rlist.append(abs(ztmnmE)/ztmnmE)
            Rlist.append(abs(ztmnmE)/ztmnmE)
            Qlist.append(abs(ztenmH)/ztenmH)
            Qlist.append(abs(ztenmH)/ztenmH)
            Qlist.append(abs(ztmnmH)/ztmnmH)
            Qlist.append(abs(ztmnmH)/ztmnmH)

    if mvar1==0 and nvar1==0:
```

```
                Pmatrix=Pmatrix1

            else:
                Pmatrix=np.concatenate((Pmatrix, Pmatrix1), axis=0)
    #Filling Q, R and propagation matrices
    np.fill_diagonal(Qmatrix, Qlist)
    np.fill_diagonal(Rmatrix, Rlist)



    np.fill_diagonal(Vij21matrix, Vijlist)
    np.fill_diagonal(Vij12matrix, Vijlist)


    if sect==0:
        np.fill_diagonal(Vij21initmatrix, Vijinitlist)
        np.fill_diagonal(Vij12initmatrix, Vijinitlist)
    if sect==(section_number -1):
        np.fill_diagonal(Vij21finalmatrix, Vijfinallist)
        np.fill_diagonal(Vij12finalmatrix, Vijfinallist)


    return Pmatrix, Qmatrix, Rmatrix, totalpower, Vij11matrix, Vij12matrix, Vij21matrix,
    Vij22matrix, Vij12initmatrix, Vij21initmatrix, Vij12finalmatrix, Vij21finalmatrix, Identitymatrix



Pmatrix ,Qmatrix, Rmatrix, totalpower, Vij11matrix, Vij12matrix, Vij21matrix, Vij22matrix,
Vij12initmatrix, Vij21initmatrix, Vij12finalmatrix, Vij21finalmatrix, Identitymatrix = mode(n,m)


Pmatrix= np.transpose (Pmatrix)
#organising matrices

s = [[str(e) for e in row] for row in Pmatrix]
lens = [max(map(len, col)) for col in zip(*s)]
fmt = '\t'.join('{{:{}}}'.format(x) for x in lens)
table = [fmt.format(*row) for row in s]


s = [[str(e) for e in row] for row in Qmatrix]
lens = [max(map(len, col)) for col in zip(*s)]
fmt = '\t'.join('{{:{}}}'.format(x) for x in lens)
table1 = [fmt.format(*row) for row in s]



s = [[str(e) for e in row] for row in Rmatrix]
lens = [max(map(len, col)) for col in zip(*s)]
fmt = '\t'.join('{{:{}}}'.format(x) for x in lens)
table2 = [fmt.format(*row) for row in s]
```